

FINAL REPORT

Technical Assistance for the Deployment of an Advanced Hyperspectral Imaging Sensor during HYFLEX

in response to

ESA Contract No. 4000107143/12/NL/FF/lf

final version

version 1: 4 December 2013

version 2: 16 April 2014



Table of Content

Acronyms and Abbreviations	4
1 Summary of main findings	5
1.1 HyPlant: a high-performance imaging spectrometer to measure reflectance and sun-induced fluorescence.....	5
1.2 Mapping of sun-induced fluorescence according to the 3-FLD method.....	5
1.3 Mapping of sun-induced fluorescence using singular vector decomposition	5
1.4 Mapping of sun-induced fluorescence using spectral fitting methods.....	6
1.5 Consistency of fluorescence measurements	6
1.6 Outlook/recommendations for future activities	6
2 Overview of the campaign concept	7
2.1 Background	7
2.2 Campaign objectives	7
3 Description of the study area	9
3.1 Finnish test site.....	9
3.2 Jülich study sites, Germany	9
3.2.1 TR32 study site.....	9
3.2.2 Klein-Altendorf study site.....	12
3.3 CzechGlobe study site, Bílý Kříž, Czech Republic.....	14
3.3.1 Spruce forest experimental site.....	14
3.3.2 Meadow experimental site.....	16
4 Campaign activities, material, methods, and data	18
4.1 HyPlant: Technical description, sensor characteristics and performance.....	18
4.1.1 Sensor characteristics and performance in 2012	18
4.1.2 Sensor characteristics and performance in 2013 as of today	21
4.2 Airborne measurements 2012	24
4.2.1 Jülich campaign, Germany	24
4.2.2 Bílý Kříž campaign, Czech Republic	28
4.3 Complementary ground data	31
4.3.1 TOC fluorescence ground reference measurements	31
4.3.2 Unmanned Aerial Vehicle measurements	34
4.3.3 Characterisation of atmospheric properties to test the influence of atmospheric variations on the signal and for atmospheric correction.....	35
4.3.4 Characterisation of the structural and functional status of vegetation using leaf and canopy level methods.....	38
4.3.5 Measurements of canopy photosynthesis using eddy covariance techniques ...	39
4.3.6 Thermal measurements.....	39
4.4 Campaign database	40
4.4.1 Data archive	40

4.4.2	Campaign GIS	40
5	Results	43
5.1	Weather conditions during the campaign	43
5.1.1	Agriculture, Jülich campaign, Germany	43
5.1.2	Forest, Bílý Kříž campaign, Czech Republic	43
5.2	Atmospheric characterisation	44
5.2.1	Agriculture	44
5.2.2	Forest	51
5.3	Top of canopy fluorescence	64
5.3.1	Agriculture	64
5.3.2	Forest	66
5.4	Airborne mapping of fluorescence using the HyPlant sensor	75
5.4.1	3-FLD like method	76
5.4.2	Statistical approach for fluorescence retrieval based on singular vector decomposition (SVD)	82
5.4.3	Spectral Fitting Method 1 (SFM-1, University of Valencia)	88
5.4.4	Spectral Fitting Method 2 (SFM-2, UNIMIB)	98
5.5	DCMU experiment – Biochemical block of photosynthesis	105
5.5.1	Leaf level	106
5.5.2	Diurnal courses of reflectance values, vegetation indices, and sun-induced fluorescence	107
5.5.3	Airborne measurements	109
	References	112

Acronyms and Abbreviations

AOT	Aerosol Optical Thickness
Agl	Above ground level
Cdm	Leaf Dry Matter Content
CIP	Campaign Implementation Plan
Cw	Leaf Water content
DOY	Day of the Year
DEM	Digital Elevation Model
EC	Eddy Covariance
EE	Earth Explorer
EMORAL	Esa's MOBILE Raman Lidar
ESA	European Space Agency
ESAC	Earth Science Advisory Committee
ESTEC	ESA Technical Centre
FLEX	FLuorescence EXplorer
FLORIS	FLuORescence Imaging Spectrometer
FLUSS	Atmospheric corrections for fluorescence signal and surface pressure retrieval over land
FWHM	Full Width at Half Maximum
HYFLEX	HYperspectral FLuorescence EXperiment
HyPlant	Hyperspectral Plant imaging spectrometer
ITP	Instrument Test Plan
LAI	Leaf Area Index
MERIS	Medium Resolution Imaging Spectrometer
MRI	Multiplexer-based Radiometer Irradiometer
MSS	Manual Spectrometer System
PBL	Planetary Boundary Layer
RH	Relative Humidity
RT	Radiative Transfer
S-3	Sentinel-3
SNR	Signal to Noise Ratio
SoW	Statement of Work
SR	Spectral Resolution
SS	Spectral Shift
SSI	Spectral Sampling Interval
SIF	Sun-induced fluorescence
SSL	Spectral Stray Light
TOC	Top-Of-Canopy
TR32	Transregional Collaborative Research Centre 32
UAV	Unmanned Aerial Vehicle
SVD	Single Vector Deconvolution
SSL	Spectral Stray Light
SFM	Spectral Fitting Method

Reference Documents (RD)

- [RD-1] EOP-PI/2008-05-83, An Analysis of the Synergy Between FLEX and Sentinel-3
- [RD-2] FLEX Candidate Earth Explorer Mission: Mission Requirements Documents, MRD, EOP-SM/2221/MD-md
- [RD-3] Instrument Test Plan, Issue 1
- [RD-4] Instrument Test Report, Issue 2
- [RD-5] Technical note: HyPlant destriping algorithm

1 Summary of main findings

1.1 HyPlant: a high-performance imaging spectrometer to measure reflectance and sun-induced fluorescence

- HyPlant was extensively tested and recognised as a high-performance instrument that can operate stably and reliably under airborne conditions.
- The radiometric performance of the sensor is good, and the instrument can serve as an airborne demonstrator for the proposed FLEX mission.
- The sensor was fundamentally improved between 2012 and 2013, and all of the technical problems of the first year were solved.
- The point spread function was characterised, and a software deconvolution of the signal should further improve the signal.

1.2 Mapping of sun-induced fluorescence according to the 3-FLD method

- The 3-FLD method can be successfully used to retrieve fluorescence in the O₂-A band.
- Reference surfaces, however, are required to compensate for uncertainties caused by insufficient atmospheric modelling and remaining sensor artefacts (i.e., spectral shift, band broadening, vignetting).
- These non-fluorescence pixels are used to constrain the retrieval by empirically optimising atmospheric parameters involved in the retrieval scheme, i.e., transmittance in observer direction and path radiance.
- For best results the following criteria should be met by the flight scene:
 - Sufficient non-fluorescence pixels must be present, spanning the full field of view across-track.
 - The correction should be performed for each flight line separately.
- The code for this modified 3-FLD approach is available. The last version was fundamentally debugged, validated, and now delivers good maps of fluorescence.

1.3 Mapping of sun-induced fluorescence using singular vector decomposition

- The singular vector decomposition (SVD) method can be used to retrieve fluorescence in the O₂-A and O₂-B band and does not require any further input parameters and also works in densely vegetated areas, such as the Czech forest site.
- This method performed very well during this activity and delivered stable and good results in most cases.
- There are, however, a few limitations to this method:
 - The outcome is dependent on the training of the vectors and the results cannot be interpreted for the influence of single influencing factors.
 - In some flight lines (about 10%), the method delivers obviously false results.

1.4 Mapping of sun-induced fluorescence using spectral fitting methods


- Two spectral fitting methods (SFM) were developed and applied to top-of-canopy point measurements. Both approaches deliver data on fluorescence at 687 nm and 760 nm.
- The first spectral fitting method (SFM-1) works on apparent reflectance data and uses the absorption features around the O_2 bands. The algorithm was successfully applied to modelled data and TOC spectrometer measurements and first HyPlant maps of fluorescence at 687 nm and 760 nm were analysed. The SFM methods are influenced by pixel noise and stray light. The relative values are convincing. The absolute values of fluorescence fluxes are by a factor of 2–6 higher than the ground measurements and thus refinement is proposed.
- The second spectral fitting method (SFM-2) works on radiance data and uses different spectral windows with a focus around the O_2 absorption bands. The algorithm was routinely used for TOC spectrometer measurements and first maps of fluorescence at 760 nm that were produced from HyPlant data. Deconvolution of the HyPlant data greatly improved the results, and first quantitative maps of fluorescence are presented in this report. Absolute values are similar to ground measurements.
- This is the first demonstration that fluorescence can be retrieved from experimental flight data taking the proposed retrieval scheme of FLEX into account.

1.5 Consistency of fluorescence measurements

- Canopy fluorescence could be consistently retrieved from top-of-canopy measurements and airborne mapping. Several maps from different flight lines were calculated using the three approaches mentioned above. The results are consistent.
- There is a very good correlation between reference fluorescence measured on ground and airborne-based fluorescence obtained from different flight heights. This suggests that atmospheric absorption and scattering effects can be successfully compensated.
- Maps of fluorescence in the O_2 -A band are presented and compared to other vegetation products. It is demonstrated that fluorescence shows an additional signal that is not simply related to classical vegetation products, especially in dense canopies.
- It could be shown that fluorescence in the O_2 -A band is different from fluorescence in the O_2 -B band. This provides experimental evidence that both fluorescence peaks are related to different canopy properties (structure, function, and relations).
- Healthy canopies seem to reach fluorescence values of $2 \text{ mW/m}^2/\text{sr/nm}$ at 760 nm (O_2 -A band). No substantially higher fluorescence values were found over a wide variety of vegetation types, suggesting that this might be the maximum value for healthy vegetation.
- Needle forest has a lower fluorescence emission than crops and grasslands, with maximum fluorescence emissions being in the range of $1.5 \text{ mW/m}^2/\text{sr/nm}$ (O_2 -A band).
- The fluorescence signal is an indicator for the functional status of vegetation. This could be shown convincingly by the application of a chemical photosynthesis blocking agent (DCMU). The physiological block of photosynthesis resulted in a 3-fold increase of the sun-induced fluorescence. Aircraft mapping could monitor this increase.

1.6 Outlook/recommendations for future activities

- HyPlant should be further used for FLEX related activities and may also provide an airborne sensor that could be useful for other earth observation activities.
- The four retrieval methods all have proven their potential for different applications and thus should all be equally included in further activities preparing the FLEX mission.

	Doc.: HYFLEX – Final Report		
	Date: 16-04-2014	Issue: 8	Revision: 0
	Ref.: ESA Contract No. 4000107143/12/NL/FF/If		Page: 7 / 113

2 Overview of the campaign concept

2.1 Background

Although vegetation monitoring has been one of the key objectives of many different satellite missions in the past, Fluorescence Explorer (FLEX) will be the first mission explicitly designed to monitor the photosynthetic activity of the terrestrial vegetation layer by using a completely novel technique measuring the chlorophyll fluorescence signal that originates from the core of the photosynthetic machinery. This will provide new possibilities to assess the dynamics of actual photosynthesis through sun-induced fluorescence, which offers a great advancement over current capabilities that can only detect potential photosynthesis as derived in passive reflectance measurements by conventional land surface monitoring satellites. While current observational techniques provide information about the amount of light absorbed by vegetation, FLEX will provide direct insight on how much of such absorbed energy is actually used for photosynthesis, which is a fundamentally new type of information never available before from space observations. The new EE-8 FLEX mission concept comprises a smaller satellite carrying a Fluorescence Imaging Spectrometer (FLORIS), which is flying in tandem with Sentinel-3 (S-3) [RD-1], [RD-2].

This HYFLEX campaign aimed to deliver maps of sun-induced fluorescence recorded from airborne measurements using the approaches of the space-borne FLEX mission. Airborne data will be validated by ground-based measurements. Those data provide a crucial element related to fluorescence retrievals from space in the context of the FLEX mission, as implemented in tandem with S-3.


The HYFLEX project tested and verified the performance of the Hyperspectral Plant Imaging Spectrometer (HyPlant). HyPlant is a narrow-band imaging sensor for passive monitoring of sun-induced fluorescence in the O₂ absorption bands, which was developed in cooperation of the Forschungszentrum Jülich (Jülich Research Centre, Germany) and SPECIM Imaging Ltd. (Finland). The verification of the data was performed for different land-use types during dedicated campaigns. Test sites were the radiometric calibration site of the University of Helsinki, Finland, a heterogeneous and well-characterised agricultural area in Western Germany, which is intensively monitored by the Transregional Collaborative Research Centre 32 (TR32), and a forest site in the Czech Republic (Experimental Ecological Site Bílý Kříž of CzechGlobe).

2.2 Campaign objectives

The objectives of the HYFLEX activity were:

1. operate and verify the new HyPlant sensor through airborne measurement activities over agricultural and forest areas
2. calculate maps of sun-induced fluorescence using the proposed approaches of the space-borne FLEX mission and to validate these maps using ground-based measurements of top-of-canopy sun-induced fluorescence
3. compare airborne fluorescence estimates over agricultural and forest areas to ground measurements and model simulations.

These objectives were achieved through the collection, processing, and preliminary analysis of airborne and correlative datasets. Through this activity, it was possible to verify the signal in the context of future missions, document the link between fluorescence signal and vegetation geophysical properties, and support the elaboration of mission-specific algorithms. The work carried out in this study is a beneficial direct to the Earth Explorer candidate mission and particularly to demonstrating the advantages of the selected implementation concept for measuring land surface vegetation fluorescence. The objectives also required interaction with other relevant activities and studies, carried out by ESA, namely the FLEX photosynthesis study and the FLEX PARCS study.

	Doc.: HYFLEX – Final Report		
	Date: 16-04-2014	Issue: 8	Revision: 0
	Ref.: ESA Contract No. 4000107143/12/NL/FF/If		Page: 8 / 113

Five main tasks were defined to accomplish the objectives given above. In the following, a summary of each task under consideration of the objectives and references within this document is given.

Task 1: HyPlant readiness

In close co-operation with the instruments manufacturer (Specim, Ltd., Finland), HyPlant readiness was proven during the test campaign in Finland (chapter 3.1, RD-3). The outcome of this campaign was the evaluation of the technical performance of the instrument (RD-4). Because HyPlant is a prototype instrument, the technical evaluation was continuously on-going during this activity; thus, technical improvements to the sensor were continuously monitored and updated. A summary of the sensor characteristics and technical performance of HyPlant based on the 2012 data is given in the Instrument Test Report [RD-4], and a summary of the technical performance of the instrument as of October 2013 is given in chapter 4.1

Task 2: HyPlant agricultural campaign

The HyPlant agricultural campaign took place in the Jülich area (chapter 3.2), with measurements days on 22, 23, and 27 August 2012. Several flight lines were recorded at different times during the day using a north-south-oriented flight pattern (chapter 4.2.1). In addition, complementary ground data for validation of level-2 data were recorded (chapter 4.3). Different algorithms to derive sun-induced fluorescence from HyPlant data were used to calculate maps of sun-induced fluorescence (chapter 5.4).

Task 3: HyPlant forest campaign

The HyPlant forest campaign took place in eastern Czech Republic, Bílý Kříž area (chapter 3.3), with measurements days on 5, 7, and 9 September 2012. Several flight lines were recorded at different times over the day in a north-south-oriented flight pattern (chapter 4.2.2). In addition, complementary ground data for validation of level-2 data were recorded (chapter 4.3). Different algorithms to derive sun-induced fluorescence from HyPlant data were used to calculate maps of sun-induced fluorescence (chapter 5.4).

Task 4: Data acquisition

All data acquired during HYFLEX campaign, the intermittent processing results, and the final results/products are archived on a FTP server, which will be maintained by the Forschungszentrum Jülich, Germany. All project partners and the agency have access to this server.

Task 5: Data processing and preliminary analysis

This final report includes a full description of the conducted campaigns, acquired data (chapters 3 and 4), processing steps, and a review of the analysed results (chapter 5).

Main campaign data are organised in a GIS system (chapter 4.4.2), which will remain available to all project partners and will be delivered to the agency as well.

With the implementation of the test, agricultural, and forest campaign (task 1, 2, 3) objective 1 of the HYFLEX Project is fulfilled. From selected flight lines, maps of sun-induced fluorescence were calculated using the standard 3-FLD retrieval method (chapter 5.4.1) as well as more advanced retrieval algorithms, such as a statistical approach (chapter 5.4.2) and spectral fitting methods (chapter 5.4.3 and 5.4.4) [objective 2]. Calculated maps were validated by top-of-canopy (TOC) fluorescence measurements (chapter 5.3), and fluorescence data were compared to forward modelling approaches of biophysical parameters of canopy properties [objective 3].

3 Description of the study area

3.1 Finnish test site

The Helsinki area has two potentially interesting test sites (Figure 1). However, when visiting the sites for the first time, we decided to concentrate only on one site due to logistical reasons. The first, operated by the University of Helsinki, is an agricultural test site with large homogeneous plots of different species that are easy accessible. The second, the Sjököla test field operated by the Finnish Geodetic Institute, is a photogrammetric test field for radiometric and spatial resolution calibration and testing. This second site was chosen for performing the test flights.



Figure 1: Map of the Helsinki area with the Sjököla and agricultural test sites.

3.2 Jülich study sites, Germany

3.2.1 TR32 study site

The Transregional Collaborative Research Centre 32: Patterns in Soil-Vegetation-Atmosphere Systems: Monitoring, Modelling and Data Assimilation (TR32) is an interdisciplinary, collaborative project of the University of Bonn (host university), the University of Cologne, RWTH Aachen, and Forschungszentrum Jülich. The central hypothesis of the TR32 is based on the paradigm that characterisation of spatio-temporal structures and patterns will lead to a deeper qualitative and quantitative understanding of the soil-vegetation-atmosphere system. In this context, the TR32 specifically focuses on the analysis of H_2O and CO_2 fluxes across a large range of space and time scales (see www.tr32.de for more information). The Rur catchment (2354 km²) is the research area of the TR32 project. It can be described as an anthropogenically influenced area consisting of a variety of different vegetation types, including agricultural fields, grasslands, meadows, and small forest patches. Annual precipitation ranges from about 650 mm/year up to 1350 mm/year mainly varying with orography and is influenced by lee effects.

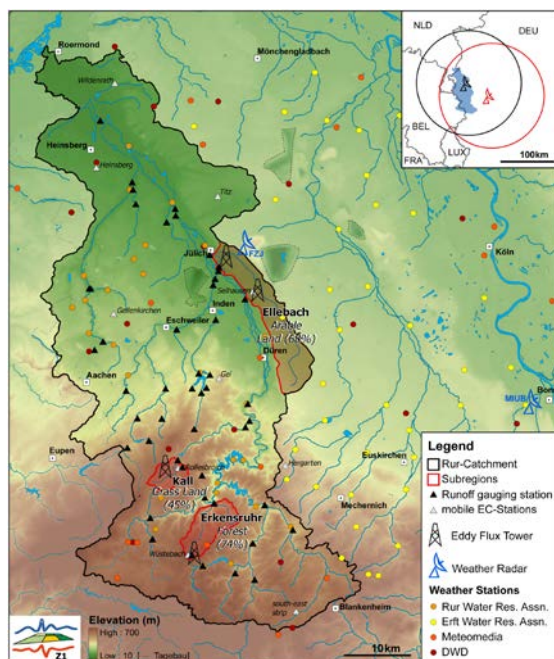


Figure 2: The Rur catchment and TR32 measurement sites.

Based on environmental monitoring, modelling, and data assimilation during the last six years of the TR32 project, basic data sets on land use, soil types, and relief are provided (Table 1). In total, four eddy flux stations, providing ecosystem gas exchange data (H_2O and CO_2) and micrometeorological measurements, have been installed in the agricultural area near Selhausen (Figure 3; Table 2). This area is well characterised and provides good infrastructure and power supply. Marked sugar beet fields are continuous measurements fields of the TR32 (leaf and chamber gas exchange, LAI). During aircraft campaigns, additional ground validation measurements were performed for measuring vegetation biochemical and biophysical properties, plant function and structure for selected sites and the different land-use types.

Table 1: Available data of the TR32 study side, Jülich.

Parameter	Source	Resolution
GEODATA		
Soil type	digital soil map ('Informationssystem Bodenkarte 5')	1:5000
Land use	ASTER satellite images, bands 1-3	15 m
Relief	Digital Topographic Map Digital Elevation Model (DEM) 10 (with anthropogenic landforms)	1:25 000 10 m (higher resolution is available on request)
ATMOSPHERIC DATA		
Aerosol optical thickness	Sun photometer (CE318NEBS9, calibrated within AERONET)	
MICROMCOLOGICAL DATA		
Gas exchange (H_2O , CO_2)	Eddy covariance (EC) measurements	m-300m; min-h 4 EC stations
Wind speed and direction, humidity, air temperature, radiation components, precipitation, soil	EC ancillary measurements, climate stations (field)	m/cm-m min-h

temperature/moisture		
----------------------	--	--

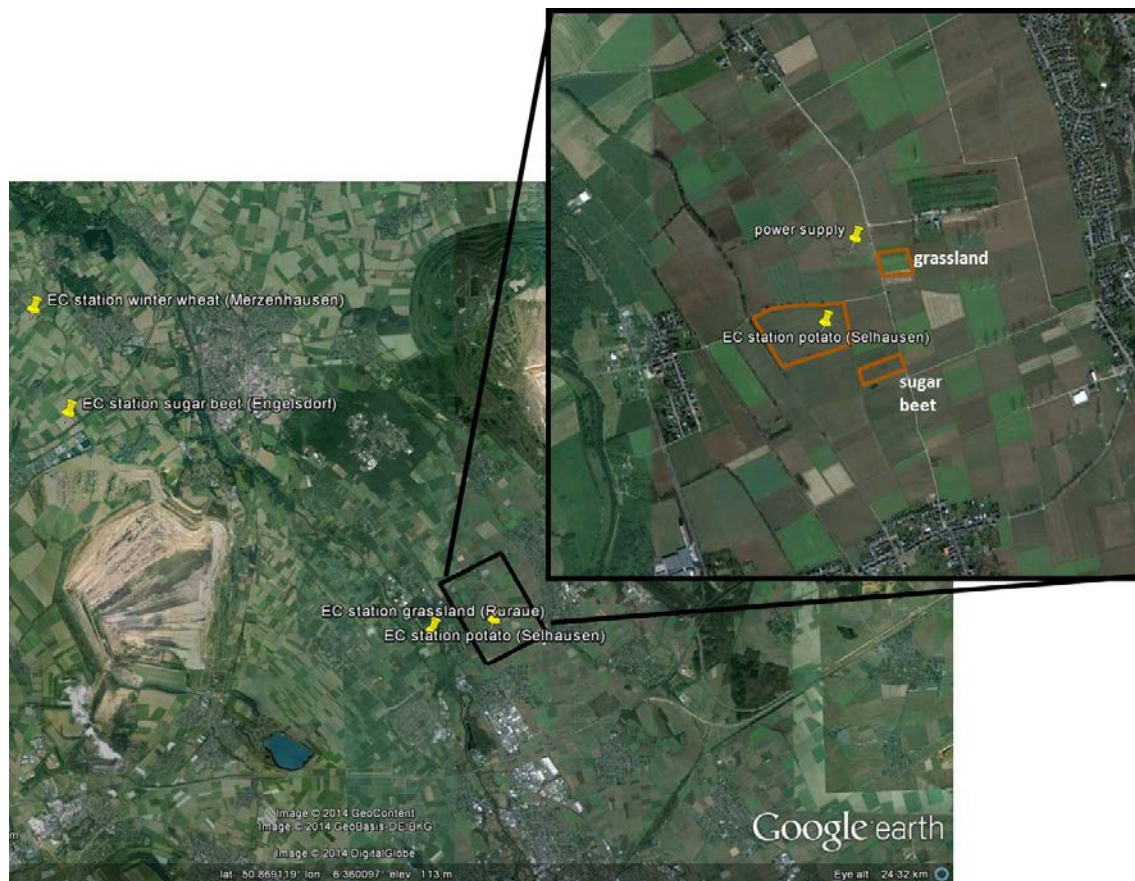


Figure 3: Selhausen measurement sites in the TR32 study area covering several types of agricultural fields.

Table 2: Field coordinates and location of EC stations of the TR32 measurement sites.

	Crop	Field centre / location EC station
Selhausen	bare soil (power supply)	50.869374° N, 6.450020° E
	sugar beet	50.864179° N, 6.452070° E
	grassland	50.868657° N, 6.452904° E
	potato	50.8658339° N; 6.4473888° E
Merzenhausen	winter wheat	50.9297879° N, 6.2969924° E
Engelsdorf	sugar beet	50.9115426° N, 6.3088546° E
Ruraue	grassland	50.8636289° N, 6.4274571° E

3.2.2 Klein-Altendorf study site

The Außenlabore Agrar, Geodäsie, Ernährung (Field Labs for Agriculture, Geodesy, Nutrition) at Campus Klein-Altendorf near Bonn comprises 181 ha for field trials and approximately 4,800 m² for Greenhouse trials. During the last years, the following research infrastructure was established:

- greenhouse for plant phenotyping: plants can be grown in soil up to a height of 4.5 m; one chamber is equipped with a 'moving fields' infrastructure with sixty-eight rotating tables; three chambers with a usable area of 48 x 6.4 m; regular field equipment can be used; roofing material is a glass-foil combination with high UV-transparency
- rainout-shelter: movable greenhouse for drought-stress research and experiments on climatic change. Plants can be grown under controlled water and nutrient supply without changing temperature and humidity in comparison to field conditions; highly UV-A and UV-B transmissible roofing materials; foundations reach 1.5 m in depth to avoid lateral water flow; 3-year crop rotation; size: 50 x 11 m, 4.5 m height; equipped with a programmable watering system using rain water and a sensor for measuring plant height.
- greenhouse with high light supply (1000 W m⁻²) and roofing material differing in UV-A and/or UV-B transparency; water and nutrients are controlled by different measuring systems (e.g., soil moisture); plants can be cultivated in pots (40 tables with preinstalled drop irrigation), special laundry system and/or in soil; usable height: 4.5 m, chamber size: 37 x 6.4 m
- greenhouse for medicinal plants equipped with a sensors system in two chambers differing in UV-transparency
- greenhouse with foil-foil combination differing in UV-transparency; usable height: 4.5 m; five chambers measuring 24 x 6.4 m
- Machine hall and machine shop for developing new, testing and repairing machines; usable area: 2,100 m²; usable height: 7.5 m
- Solar drying: a 'greenhouse' using a solar chimney was developed to dry biomass
- Research heating plant: a 500 kW heating plant was built for a sustainable and CO₂-neutral heating of the campus facilities using biomass plants (e.g., *Miscanthus*, short-rotation coppice); in the heating plant different biomass plants can be tested and evaluated.

On Campus Klein-Altendorf, research can be conducted with all kinds of plants and crops, ranging from small plants like *Arabidopsis* or herbs to large crops like maize, from annual crops like vegetables to perennial plants like *Miscanthus* or fruit trees. Plants can be grown in the experiments under practical conditions. All field and greenhouse equipment is standardised.

During aircraft campaigns, validation and ground reference measurements took place at three fields belonging to Campus Klein-Altendorf (Figure 4, Table 3). One field is an intensively monitored study site that consists of different varieties of sugar beet grown under two different nitrogen treatments (Figure 5). This sugar beet experiment is equipped with a 7 m tall tower. An active laser-induced fluorescence instrument (LIFT) was already installed and adjusted to the field (Figure 5). The tower provides the possibility to install additional instrumentation, such as the thermal camera from Lippmann Institute and Trier University (chapter 4.3.6).



Figure 4: Agricultural study site Klein-Altendorf.

Table 3: Fields coordinates of Klein-Altendorf experimental site.

Field/Crop	Location
sugar beet experiment	50.623738 N, 6.986002 E
sugar beet	50.616016 N, 6.992406 E
grassland	50.612236 N, 6.993832 E

2	4		1	3		2	4		1	3
2	4		1	3		2	4		1	3
113	114	R	115	116	R	213	214	R	215	216
4	5		12	13		20	21		28	29
3	1		4	2		3	1		4	2
109	110	R	111	112	R	209	210	R	211	212
3	6		11	14		19	22		27	30
4	3		2	1		4	3		2	1
105	106	R	107	108	R	205	206	R	207	208
2	7		10	15		18	23		26	31
1	2		3	4		1	2		3	4
101	102	R	103	104	R	201	202	R	203	204
1	8		9	16		17	24		25	32

Old numbering: 101 – 216; Numbering of Fields: 1 – 32;
 1: Pauletta 2: Berenika 3: Maurica 4: Cesira



Figure 5: Sugar beet experiment in Klein-Altendorf: four varieties, two nitrogen treatments, four repetitions.

3.3 CzechGlobe study site, Bílý Kříž, Czech Republic

Experimental research site of Bílý Kříž was established in the Beskydy Mountains in 1986. Recently, the experimental site is being used for the monitoring of energy and substances fluxes using eddy covariance technique and the evaluation of carbon pools in mountain forest and meadow ecosystems. The Bílý Kříž site is part of the CzechGlobe infrastructure (<http://www.czechglobe.cz/en/>). The research site is located in the Moravian-Silesian Beskydy Mountains in the eastern part of the Czech Republic, bordering the Slovak Republic: 49.50194°N, 18.53667° E, mean altitude of 880 m above sea level. (Figure 6). The climate of the area is characterised by an annual mean temperature of 5.5°C, annual mean relative air humidity of 80%, and a total rainfall of 1000–1400 mm.

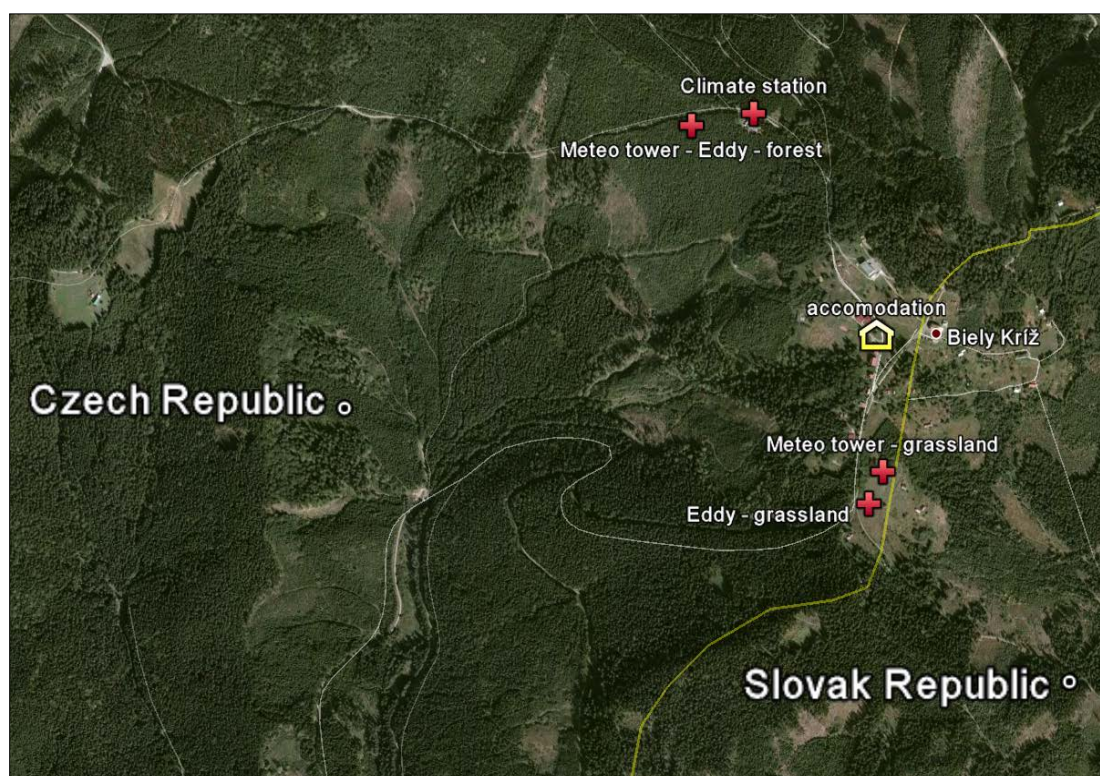


Figure 6: CzechGlobe study site (Bílý Kříž).

3.3.1 Spruce forest experimental site

The spruce forest experimental site (Figure 7) of the Bílý Kříž is covered by a 35-year-old regular plantation of *Norway spruce* (*Picea abies* (L.) Karst) growing on a moderate slope (13°) with S-SE orientation. The geological bedrock is formed by Mesozoic Godula sandstone (flysch type), with ferric podzols.

The Norway spruce site serves as an experimental site for ecosystem monitoring, and many types of continuous/discrete measurements have been carried out there for more than fifteen years (e.g., GHG and energy fluxes, water balance, carbon stock in vegetation and soil, biomass inventory, tree transpiration flow, nitrogen inputs, etc.). The site is equipped with power supply, a meteorological station covering basic micrometeorological measurements (Table 4), and an EC tower (49.50222° N; 18.53683° E, Figure 7) where additional equipment can be installed.



Figure 7: CzechGlobe study site (Bílý Kříž) with Norway spruce experimental plot: two glass domes (*left*) and EC tower (*right*).

Table 4: Available data of the Bílý Kříž spruce forest site.

Parameter	Source	Resolution
GEODATA		
Land cover	AISA Eagle data 65 bands (2011)	40 cm
Relief	Digital Topographic Map	1:25 000
	DEM and DSM based on lidar data (2010)	5 points per m ²
MICROMETEROLOGICAL DATA		
Gas exchange (H ₂ O, CO ₂)	Eddy covariance (EC) measurements	30 min average
	Vertical gradient of CO ₂	
Wind speed and direction, humidity, air temperature,	EC ancillary measurements, vertical gradients at the meteorological tower	10 min average
Radiation, precipitation, soil temperature and moisture	EC ancillary measurements	10 min average
CO ₂ efflux measurements	Respiration of soil, stems	Every 90 min
PARAMETERS OF VEGETATION		
Leaf area index, diameter breast height, height of vegetation, sap flow	Measured on regular basis	

3.3.2 Meadow experimental site

The meadow experimental site (Figure 8) is situated at an 8° slope with SE exposition. *Festuca rubra*, *Veronica officinalis*, and *Hieracium laevigatum* are the meadow's main species. The geological bedrock is formed by claystone covered by Cambic pseudogley. Within the CzechGlobe infrastructure, basic geodata and instruments necessary for validating airborne fluorescence and spectral reflectance data can be provided (Table 5).



Figure 8: Meadow experimental plot with eddy tower.

Table 5: Available data of the Bílý Kříž, meadow site.

Parameter	Source	Resolution
GEODATA		
Land cover	AISA Eagle data 65 bands (2011)	40 cm
Relief	Digital Topographic Map	1:25 000
	DEM and DSM based on lidar data (2010)	5 points per m ²
MICROMETEROLOGICAL DATA		
Gas exchange (H ₂ O, CO ₂)	Eddy covariance (EC) measurements	30 min average
wind speed and direction, humidity, air temperature, radiation, precipitation, soil temperature and moisture	EC ancillary measurements	10 min average
PARAMETERS OF VEGETATION		
Leaf area index	Measured on regular basis	Approx. every month

At the time of the campaign, mountain grassland already showed a high degree of senescence. Therefore, two lawn carpets (12 x 12 m each) were laid on plastic sheets close to the grassland sites. One hour before the first overpass, one lawn carpet was treated with DCMU, a chemical that increases the fluorescence signal. The lawn carpets were removed in agreement with waste disposal regulations after the campaign. A small hydraulic movable platform (up to 12 m above surface) was available for the measurements of carpet reflectance (Figure 9). For a further description of the DCMU experiment, see chapter 5.5.



Figure 9: Lawn carpets with ground measurements using a portable spectrometer system (Ocean Optics) and ASD measurements from a small hydraulic platform.

4 Campaign activities, material, methods, and data

A first test campaign took place in Finland in July 2012. In the beginning of July, the sensor was installed in an aircraft operated by Specim, and first inflight data were recorded on 10 July in the area of Oulu (Northern Finland).

Subsequently, the aircraft with the HyPlant sensor was transferred to Helsinki-Malmi airport, and briefing of aircraft and ground teams took place. Several flight lines were recorded, which included the University of Helsinki's dedicated calibration site (cf. chapter 3.1), where the ground measurements took place. Selected flight lines were chosen to elaborate the technical performance of the sensor.

4.1 HyPlant: Technical description, sensor characteristics and performance

The HyPlant sensor is a high-performance imaging spectrometer for vegetation monitoring developed by the Forschungszentrum Jülich (Germany). SPECIM Spectral Imaging Ltd (Finland) was the contractor for the development and manufacture of the HyPlant sensor. Development time was 2.5 years, and the final system consists of five components:

- dual-channel VNIR & SWIR imager with a common fore optics
- fluorescence imager
- data acquisition and power unit
- position and altitude sensor
- adjustable mount.

The dual-channel imager is a line-imaging, push-broom, hyperspectral sensor, which provides contiguous spectral information from 370 to 2500 nm in one device utilising a common fore objective lens with 3 nm spectral resolution in the VIS/NIR spectral range and 10 nm spectral resolution in the SWIR spectral range. The vegetation fluorescence signal is measured with a separate push-broom sensor, the fluorescence imager, which produces data at high spectral resolution (0.25 nm) in the spectral region of the two oxygen absorption bands. The data acquisition and power unit contain two rack modules. The first module includes the data acquisition computer with system control and data acquisition software and the power supply and control electronics for the dual-channel imager and GPS/INS sensor. The second module includes the same equipment for the fluorescence imager. The position and altitude sensor (GPS/INS sensor) provides, synchronously with the image data, aircraft position and altitude data for image rectification and georeferencing. Both imagers (dual channel imager and fluorescence imager) are mounted in a single platform with the mechanical capability to align the FOV.

4.1.1 Sensor characteristics and performance in 2012

In summary, the sensor was performing very well, especially when we consider the new development and the high requirements for radiometric performance. The fluorescence module was performing very well, and we expect to have a very good basis for fluorescence retrieval. Spectral resolution (FWHM) of the fluorescence module was characterised as 0.25–0.30 nm (spectral sampling 0.11 nm) with a reasonably good signal-to-noise ratio; thus, we expect that fluorescence can be quantified using this module. The performance of the dual module was not optimal but sufficient enough for the objectives of the campaign. Performance of the VIS/NIR detector was satisfactory though not outstanding. Radiometric performance of the SWIR detector was good and signal-to-noise values of the SWIR detector can be characterised as high.

Unfortunately, we also encountered a few technical issues with the performance of the sensor.

4.1.1.1 Fluorescence imager

The major point is related to an unusual high number of ‘flickering’ pixels in some parts of the fluorescence imager during flight operation (Figure 10). These flickering pixels occurred in about 1–2% of the pixels in one detector half. The reasons behind these flickering pixels were most likely related to readout electronics on the detector itself. Such technical issues are normal for a newly developed sensor; however, we may need to deal with an increased noise level in some parts of the detector.

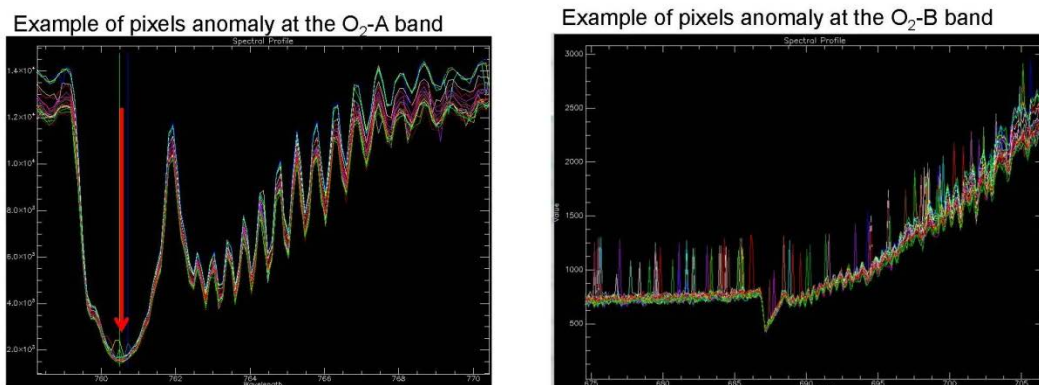


Figure 10: Example spectra of the ‘flickering pixels’.

To correct the flickering pixels in the 2012 dataset and reduce the noise in those parts of the detector, the University of Zurich developed a destriping algorithm that was applied to the 2012 HyPlant dataset (Figure 11). Details of the algorithm are described in the Technical Note: HyPlant destriping algorithm [RD-5].

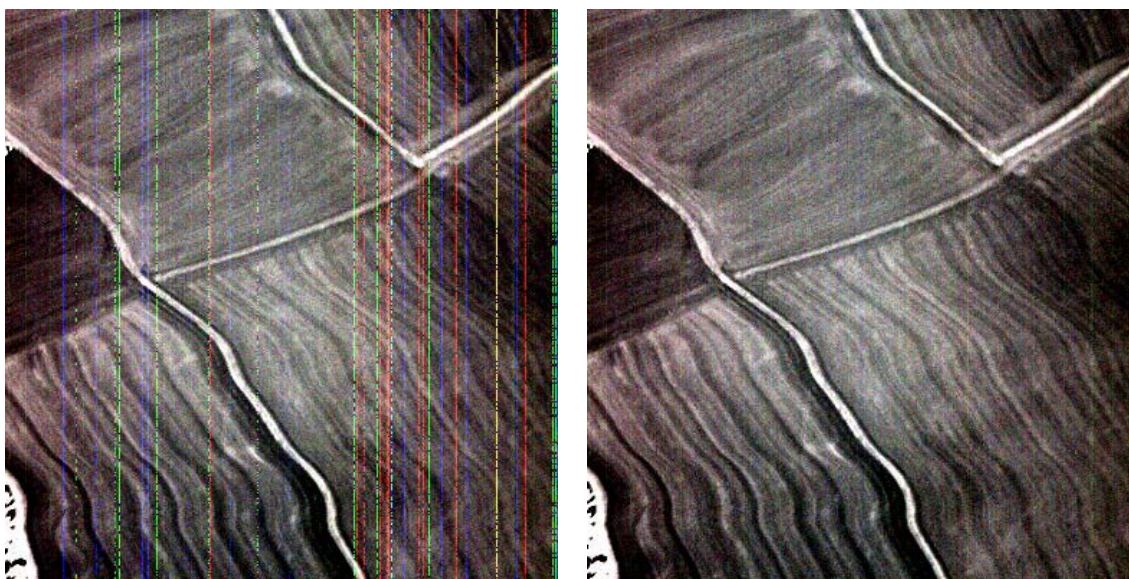


Figure 11: Colour composite of uncorrected (*left*) and corrected (*right*) radiance data. The displayed RGB's consist of three adjacent spectral bands: band number 827 (760.43 nm), 828 (760.54 nm), 829 (760.65 nm).

4.1.1.2 Dual imager

There was a reduced sensitivity in the right edge of the raw images because of the design of the module. The reduced sensitivity was only visible in raw images and was addressed during calibration.

The picture in the dual imager was out of focus, causing a reduced point spread function of the dual data. The Specim engineer evaluated the possibility of refocusing, but no risk was taken to compromise or damage the calibration.

The major point was a double image in the dual sensor (Figure 12). This was identified as the most severe issue and resulted in mixed spectra. It was addressed by masking out edges of objects. As a result, small and heterogeneous objects and fields must to be masked out. The dual image was not a ghost but real double image caused by the fact that the imager is seeing the target through two fields of view that are very close to each other in the scan direction. Therefore, both images have similar signal intensity. For more technical details, refer to the Instrument Test report [RD-4].



Figure 12: Double image above the runway in Oulu showing the double image that affects the VNIR instrument.

Based on intensive discussions, the group agreed that none of the technical issues above will pose a major problem to fluorescence retrieval and the main objectives of the campaign in 2012 can be achieved using the HyPlant sensor. In contrast, radiometric performance of the sensor was regarded as good and especially the fluorescence module performed very well, which will make fluorescence data products very likely.

4.1.2 Sensor characteristics and performance in 2013 as of today

In Winter 2012/2013, HyPlant was sent back to the manufacturer Specim to fix the issue detected during the 2012 campaigns. Radiometric calibration for both sensors was also repeated. A test flight in April 2013 and the flight campaigns conducted in 2013 revealed the following sensor characteristics and performance of HyPlant

4.1.2.1 Fluorescence imager

The dark offset level was jumping randomly in time, which was indicated by the flickering of 1–2% of the sCMOS detector array. This is an inherent feature of the sCMOS technology and was corrected by the camera manufacturer. These pixels are now treated as ‘bad-pixels’ and replaced by the value of the neighbouring pixels in the camera firmware. In 2012, there was a failure in the firmware, which has since been corrected by replacing parts of the camera and upgrading the firmware. During the test flight and the flight operation in 2013, no flickering pixels were detected anymore.

4.1.2.2 Dual imager

A bending in plane mirror caused the double image. This was the mirror that contains the slit and that mirrors the light inside the optical path. To solve this problem a correction in the mirror and totally new optical alignment procedure in the optical path of the instrument was required. During the test flight in 2013, several flight lines were recorded above the runway (Figure 13) to prove that the issue was solved.



Figure 13: At-sensor radiance of the dual imager. Non-georectified flight line recorded on 15 April 2013 at 600 m altitude. No ghost image visible.

4.1.2.3 Sensor characteristics as of today

Sensor characteristics were evaluated on basis of the data acquired in 2013. The sensor characteristics of both the fluorescence and the dual imager can be found in Table 6.

Table 6: Sensor characteristics evaluated on 2013 in flight data (the nominal/specified performance values are given in brackets).

Sensor	Dual-Channel Module		Fluorescence Module
Spectral Performance			
Range [nm]	370 – 970	970 – 2500	670 – 780
Bands #	350	272	1024
Sampling Interval [nm]	1.7 (1.75)	5.5 (6.0)	0.11 (0.11)
Resolution (FWHM) [nm]	4.0 (<3.5)	13.3 (<10)	0.25 at O ₂ -A (<0.26) 0.23 at O ₂ -B (<0.26)
Band broadening [nm]	0.2	0.2	0.01 at O ₂ -A (-) 0.03 at O ₂ -B (-)
Spectral Shift [nm]	1.2	2.4	< 0.04 (-)
Smile [nm]	0.4 (<0.42)	1.2 (<0.66)	<0.01 at O ₂ -A (<0.03) 0.01 at O ₂ -B (<0.03)
Radiometric Performance			
Accuracy	-	-	-
Linearity	-	-	-
SNR with full scale signal	- (510)	- (1100)	- (240)
Stray light and pixel cross talk [%]	- (<0.5)	- (<0.6)	- (<0.5)
Spatial Performance			
Spatial pixels	384	384	384
FOV [deg]	32.3		32.3
IFOV* [deg]	0.0832		0.0832
Swath [m]	380 @ 600m AGL		380 @ 600m AGL
Spatial Sampling Interval (across track) [m]	0.98 @ 600m AGL		0.98 @ 600m AGL
Keystone [µm]	- (<3.925)	- (<3.925)	- (<3.925)
PSF	-	-	-
Sensor Type			
Type	CMOS	MCT ²	sCMOS ³
Dynamic Range	12 bit	14 bit	16 bit

4.1.2.4 Pixel Crosstalk

During the characterisation of the fluorescence imager, a crosstalk effect was detected. The symptom of this crosstalk effect was the signal infilling in-filling from neighbouring regions across-track. This effect can be detected especially when the contrast between neighbouring pixels is high, for example, white surface on black surface. The flight lines over the runway for example reveal how the brightness from the white markings over the runway spills out laterally onto the neighbouring ground at both sides (Figure 14).

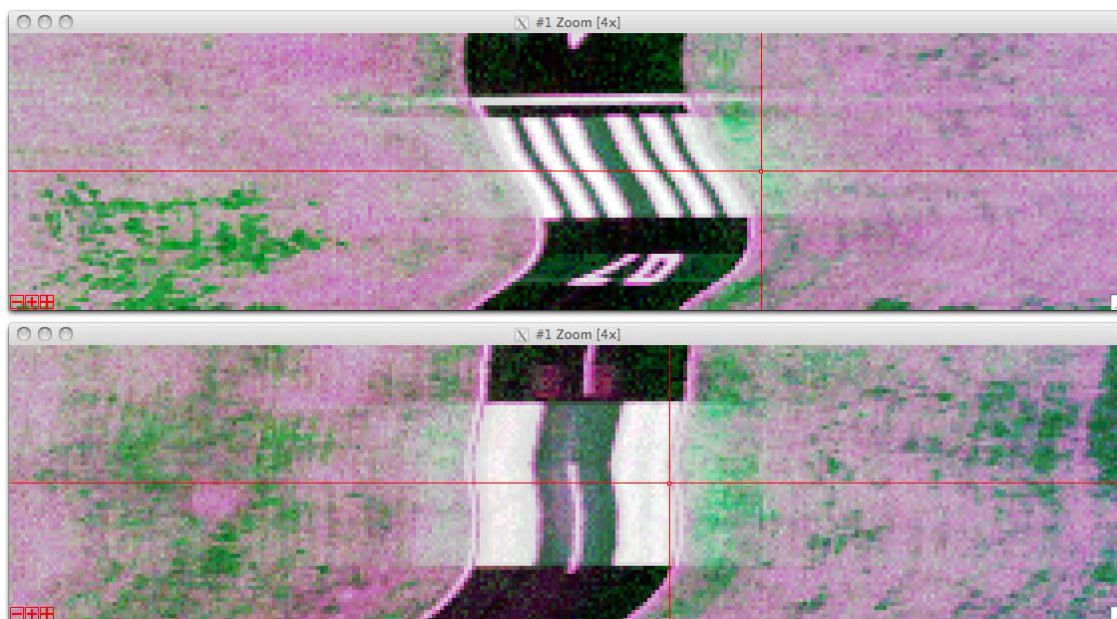


Figure 14: Airborne data with visible crosstalk effect recorded on 10 April 2013.

This crosstalk effect was already present in the 2012 campaign data. Images taken over the large areas with green vegetation did not show much contrast; therefore, the effect was not that obvious. However, a reanalyses of a test flight over Luxemburg airport buildings reveal the effect as well (Figure 15).

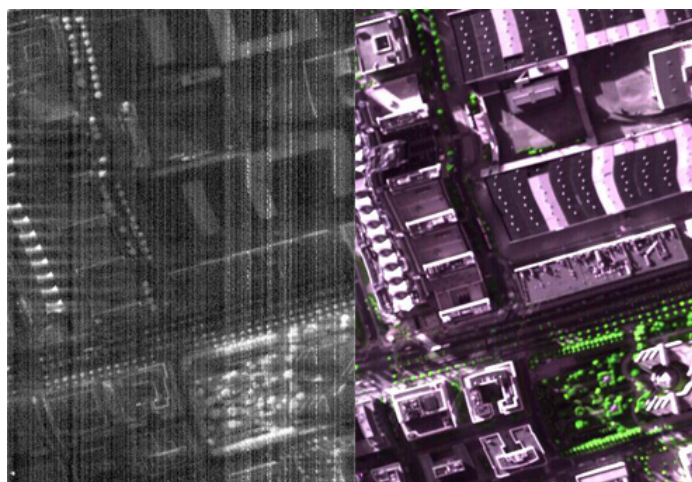


Figure 15: Airborne data with contrast enhancement to visualise the pixel crosstalk (horizontal striping at bright spots in left part of image). Data were recorded on 17 August 2012.

Using flight data the crosstalk effect can be detected but not quantified. Therefore, dedicated lab measurements were conducted to analyse the point spread function (PSF) and quantify the effect. Based on those calibration measurements (Specim, Jülich, and NASA calibration facility), a PSF with wings of 10^{-3} (as a maximum) could be estimated (Figure 16). This amount of stray light and crosstalk is good, especially considering the price and the components used in HyPlant. Nevertheless, a substantial error in retrieved fluorescence is possible because of the great contrast in brightness on the detector. To date, the spatial response function is roughly understood, but more laboratory measurements are needed to quantify it. The laboratory measurements will be performed in the winter months 2013–2014 with the aim to develop a software correction (deconvolution) for future HyPlant campaigns.

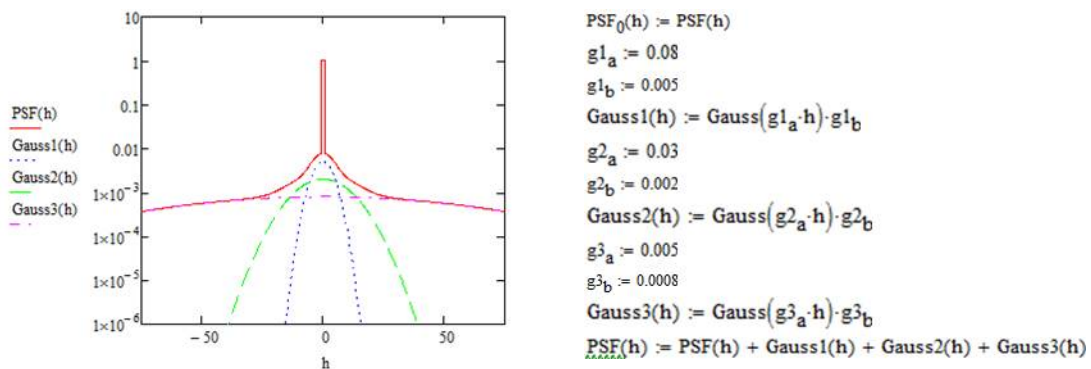


Figure 16: Spatial response function with wings between 10^{-3} and 10^{-4} . The scale in the h is in pixels, which corresponds to an angle of 0.085 degree per pixel.

4.2 Airborne measurements 2012

The HyPlant sensor was installed and certified in an aircraft of CAE, Luxemburg and transferred to Bonn Hangelar airport on 20 August 2012. Functionality of the sensor was successfully tested during the overpass by recording several flight lines.

4.2.1 Jülich campaign, Germany

4.2.1.1 HyPlant measurements on 22 August

On 22 August, weather conditions were promising, and we decided to have test flight in the morning with the aim to test communication between the operators and pilots and to give the pilots the opportunity to become familiar with the study sites and to practice visual orientation according to land marks. During the afternoon, first measurements flights were attempted. The following flight pattern was agreed.

1. The aircraft took off at 10:00 local time for the first test flight. The aim of this test flight was to practice all the flight lines and to make the pilots and operators familiar with the location. Test flights were 600 m above ground level (agl) covering the two test sites. A few sample flight lines were recorded.
2. Starting at 13:30 local time (solar noon), the two main measurement sites, Campus Klein-Altendorf (Figure 17, Table 7) and Selhausen (Figure 18, Table 8), were recorded from both elevations in the following flight pattern. All together twelve flight lines were recorded.

- Lines 1–3: three parallel flight lines over Campus Klein-Altendorf, 600 m agl, 23% overlap of the flight lines, N-S orientation
- Line 4: one perpendicular flight line over Campus Klein-Altendorf, 600 m agl, E-W orientation; crossing point was the corn/*Miscanthus* site in Campus Klein-Altendorf
- Line 5–7: three parallel flight lines over Selhausen, 600 m agl, 23% overlap of the flight lines, N-S orientation
- Line 8: one perpendicular flight line over Selhausen, 600 m agl, E-W orientation; crossing point is the position of the lidar
- Line 9: one flight line over Selhausen, 1780 m agl, N-S orientation
- Line 10: one perpendicular flight line over Selhausen, 1780 m agl, E-W orientation
- Line 11: one flight line over Campus Klein-Altendorf, 1780 m agl, N-S orientation
- Line 12: one perpendicular flight line over Campus Klein-Altendorf, 1780 m agl, E-W orientation



Figure 17: Flight lines of Campus Klein-Altendorf. Flight lines L1–L4 were flown at 600 m agl and flight lines L11 and L12 (centre N-S line plus perpendicular line) were flown at 1780 m agl.

Table 7: Flight coordinates of the Campus Klein-Altendorf test site.

Line	600 m agl, mean elevation 180 m, spatial resolution 1 m, solar noon 13:34 local time			
	lat	long	lat	long
1	50.634209	6.994838	50.603216	6.994776
2	50.634464	6.990228	50.603297	6.990157
3	50.634306	6.985716	50.603286	6.985949
4	50.615202	6.970227	50.615115	7.008573
Line	1780 m agl, mean elevation 180 m, spatial resolution 3 m, solar noon 13:34 local time			
	lat	long	lat	long
11	50.634464	6.990228	50.604931	6.990157
12	50.615202	6.970227	50.615115	7.008573



Figure 18: Flight lines for the Selhausen test site. Flight lines L5–L8 were flown at 600 m agl and flight lines L9 and L10 (centre N-S line plus perpendicular line) were flown at 1780 m agl.

Table 8: Flight coordinates of the Selhausen test site.

Lines	600 m agl, mean elevation 105 m, spatial resolution 1 m, solar noon 13:36 local time.			
	lat	long	lat	long
5	50.883979	6.455578	50.839036	6.455495
6	50.882616	6.451177	50.838014	6.451155
7	50.881413	6.446956	50.837115	6.446735
8	50.868335	6.416760	50.868294	6.469751
Lines	1780 m agl, mean elevation 105 m, spatial resolution 3 m, solar noon 13:36 local time.			
	lat	long	lat	long
9	50.882616	6.451177	50.838014	6.451155
10	50.868335	6.416760	50.868294	6.469751

4.2.1.2 HyPlant measurements on 23 August

Weather conditions on 23 August were very good and a stable high-pressure system with no clouds was predicted. The main objective of the campaign to record a time series of sun-induced fluorescence that reflect potential diurnal changes was addressed. Thus, the same flight pattern from 22 August (Figure 17, Table 8, Figure 18, Table 8) was repeated three times on 23 August, having the first measurement cycle 2.5 hours before solar noon, the second measurement cycle at solar noon, and the third measurement cycle 2.5 hours after solar noon.

Flight operation went well and thirty-three flight lines were recorded throughout the day. Two high overpasses, one in the Klein-Altendorf area and one high overpass in the Selhausen area, could not be recorded because of air-traffic restrictions (over-crowded airspace).

4.2.1.3 HyPlant measurements on 27 August

After three days of overcast conditions, weather conditions were favourable again on 27 August. The second objective of the campaign, namely to record a large map of sun-induced fluorescence in a heterogeneous landscape was addressed. A map (12x13 km²) of the central

Transregio study site was recorded with fifteen parallel flight lines (Figure 19, Table 9). Orientation along the flight lines was good, and only a few gaps may be present between them. Additionally, a few clouds were present in the area, which will most likely cause some uncertainties in the map.

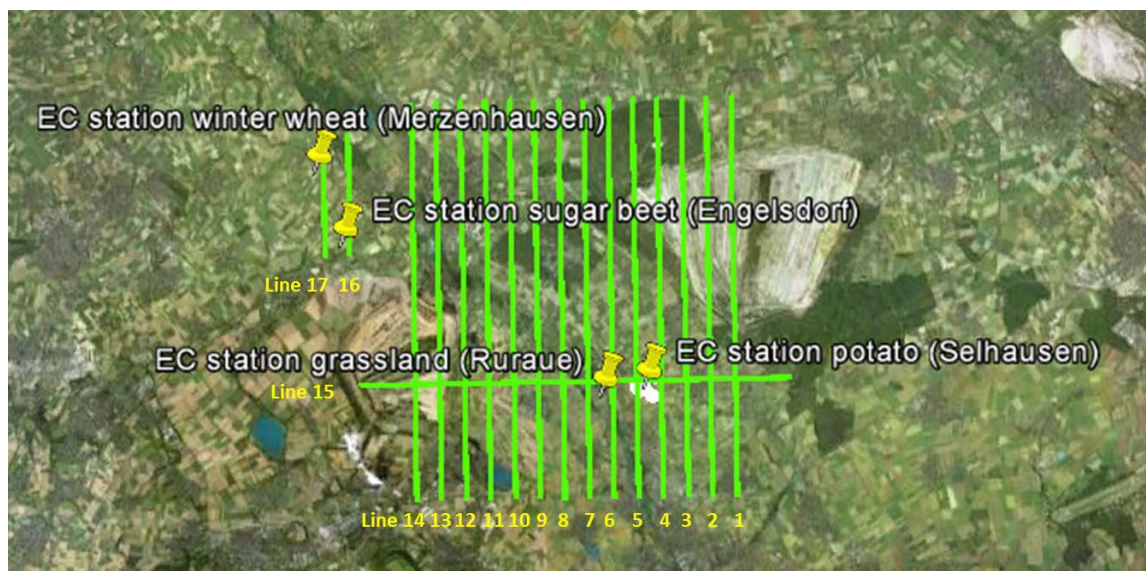


Figure 19: Flight lines for the Selhausen test site. All flight lines will be flown at 1780 m height above ground.

Table 9: Flight coordinates of the Selhausen/Merzenhausen area, flight height 1780 m agl, mean elevation height of the area 105 m.

Line	lat	long	lat	long
1	50.833873	6.490631186	50.95065695	6.490631186
2	50.833873	6.479252095	50.95065695	6.479252095
3	50.833873	6.467873004	50.95065695	6.467873004
4	50.833873	6.456493913	50.95065695	6.456493913
5	50.833873	6.445114821	50.95065695	6.445114821
6	50.833873	6.43373573	50.95065695	6.43373573
7	50.833873	6.422356639	50.95065695	6.422356639
8	50.833873	6.410977548	50.95065695	6.410977548
9	50.833873	6.399598456	50.95065695	6.399598456
10	50.833873	6.388219365	50.95065695	6.388219365
11	50.833873	6.376840274	50.95065695	6.376840274
12	50.833873	6.365461183	50.95065695	6.365461183
13	50.833873	6.354082091	50.95065695	6.354082091
14	50.833873	6.342703	50.95065695	6.342703
15	50.868294	6.316767	50.868294	6.516048102
16	50.905526	6.313162596	50.94145952	6.313162596
17	50.905526	6.301766	50.94145952	6.301766

4.2.2 Bílý Kříž campaign, Czech Republic

The aircraft with the installed sensor was transferred to Ostrava airport on 30 August 2012 and ready for a first potential flight day.

4.2.2.1 HyPlant measurements on 3 September

On 3 September, weather conditions seemed favourable in the afternoon. Starting at 15:20 local time, we recorded twelve flight lines. Flight lines L1–L9 were recorded at a flight height of 600 m agl, whereas the flight lines L10–L11 were recorded at a flight height 1780 m agl (Figure 20 and Table 10).

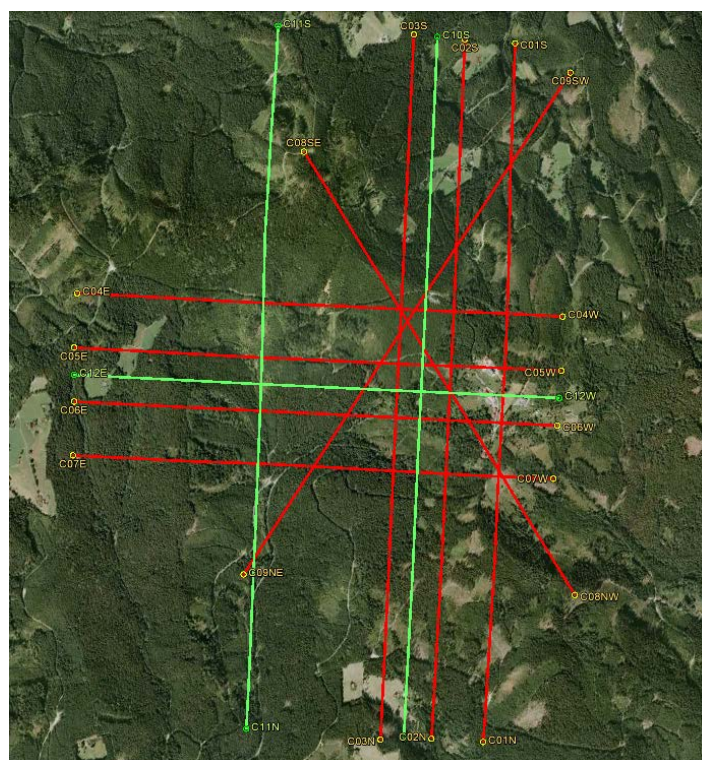


Figure 20: Flight lines for the Bílý Kříž test site. Lines L1–L9 were flown at 600 m above ground and lines L10–L12 at 1780 m above ground.

Table 10: First set of flight lines of the Bílý Kříž test site.

Start and end of flight lines (WGS84), Elipsoidal heights (WGS-84)					
	start		end		Altitude
	E [m]	N [m]	E [m]	N [m]	H el. [m]
BK_NS_low_1	49.513888	18.544535	49.483355	18.542328	1540
BK_NS_low_2	49.513993	18.541102	49.483460	18.538897	1540
BK_NS_low_3	49.514099	18.537669	49.483566	18.535466	1540
BK_EW_low_4	49.502722	18.515681	49.501747	18.547303	1540
BK_EW_low_5	49.500424	18.515514	49.499448	18.547135	1540
BK_EW_low_6	49.498126	18.515348	49.497150	18.546967	1540
BK_EW_low_7	49.495827	18.515182	49.494852	18.546800	1540
BK_SE-NW_low_8	49.508704	18.530467	49.489915	18.548188	1540
BK_SW-NE_low_9	49.490612	18.526278	49.512490	18.548179	1540
BK_NS_high_10	49.514051	18.539241	49.483517	18.537037	2720
BK_NS_high_11	49.514374	18.528651	49.483841	18.526454	2720
BK_EW_high_12	49.499275	18.515431	49.498299	18.547051	2720

4.2.2.2 HyPlant measurements on 5 September

The flight pattern as shown in Figure 20 was repeated three times on 5 September. Equivalent to the airborne measurements of the Jülich campaign, HyPlant completed one morning flight (10:50–11:55 local time), one solar noon flight (12:13–13:17; solar noon at 12:45 local time), and one afternoon flight (13:53–14:55 local time). Additionally, flight lines L1–L3 were repeated after finishing the afternoon flight pattern. Flight lines L1–L3 were determined to be priority lines because they cover the area with the ground measurements, for example, S-Fluor Box on top of the tower and grassland experiment (see chapter 4.3 and 5.5).

4.2.2.3 HyPlant measurements on 7 September

On 7 September, weather conditions seemed promising around noon and in the afternoon. It turned out that the atmospheric conditions that day were unstable. Therefore, we decided to repeat the three priority lines to have the possibility to use cloud gaps. The three priority lines (L1–L3) were recorded six times (12:17–14:16 local time). Subsequently, the atmospheric conditions seemed stable enough to record a large map (10 x 10 km) of the area with a ground pixel size of approximately 3 metres (Figure 21 and Table 11). The data acquisition started at 14:20 and finished at 15:30 local time.

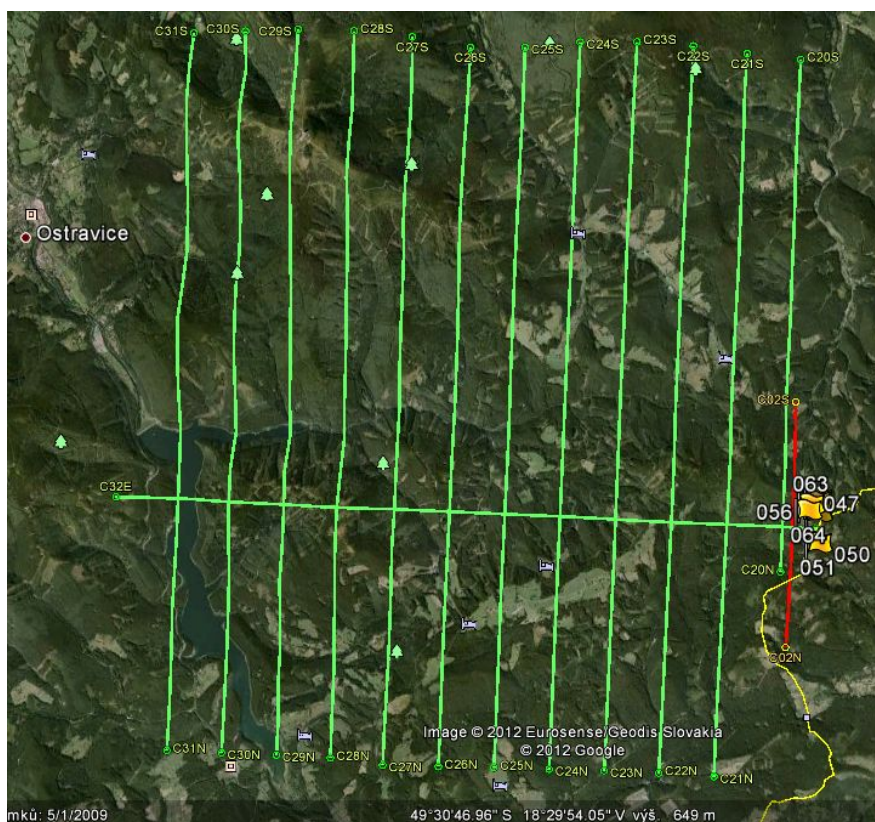


Figure 21: Second set of flight lines for the Bílý Kříž site.

Table 11: Second set of flight lines of the Bílý Kříž test site.

Start and end of flight lines (WGS84), ellipsoidal heights (WGS-84)

	start		end		Altitude
	E [deg]	N [deg]	E [deg]	N [deg]	H el. [m]
20_NS	49.556658	18.542323	49.492998	18.537720	2720
21_NS	49.556982	18.531724	49.467205	18.525258	2720
22_NS	49.557306	18.521125	49.467527	18.514678	2720
23_NS	49.557628	18.510526	49.467849	18.504099	2720
24_NS	49.557950	18.499927	49.468169	18.493519	2720
25_NS	49.558270	18.489327	49.468489	18.482939	2720
26_NS	49.558590	18.478728	49.468807	18.472358	2720
27_NS	49.558908	18.468128	49.469125	18.461778	2720
28_NS	49.559226	18.457528	49.469441	18.451197	2720
29_NS	49.559542	18.446928	49.469757	18.440616	2720
30_NS	49.559858	18.436327	49.470071	18.430035	2720
31_NS	49.560173	18.425727	49.470385	18.419454	2720
32_EW	49.502417	18.410567	49.498386	18.544215	2720

4.2.2.4 HyPlant measurements on 9 September

On 9 September, the large map was repeated two times (11:45–12:50 and 13:30–15:00 local time). In between the large maps and after the acquisition of the second map, priority lines were repeated.

4.3 Complementary ground data

4.3.1 TOC fluorescence ground reference measurements

During the campaigns, a network of dedicated and specialised ground measuring facilities were installed and operated throughout the campaign windows that recorded top-of-canopy fluorescence of different species and added supporting parameters that facilitated the continuous quantification of canopy fluorescence and the canopy photosynthesis on selected sites. Sun-induced fluorescence was recorded by custom-made S-FLUOR boxes comprising high-performance spectrometers. Continuous measurements were complemented by mobile teams that were equipped with calibrated field Spectrometers (ASD FieldSpec) to measure top-of-canopy reflectance/radiance of various vegetation types during times of overpass.

4.3.1.1 Quantification of spatial distribution of top-of-canopy sun-induced fluorescence

Different ground teams were employed to measure top-of-canopy (TOC) radiances on several surfaces covering a wide range of reflectance characteristics including different vegetation types (Figure 22). Each ground team consisted of two people and was equipped with a calibrated ASD FieldSpec spectrometer. TOC reflectance was measured by recording incoming radiation using a spectralon reflectance panel and upwelling radiation from the surface. Measurements were performed 1 hour before and 1 hour after the overpass. These measurements can be used to calculate surface reflectance with high precision.

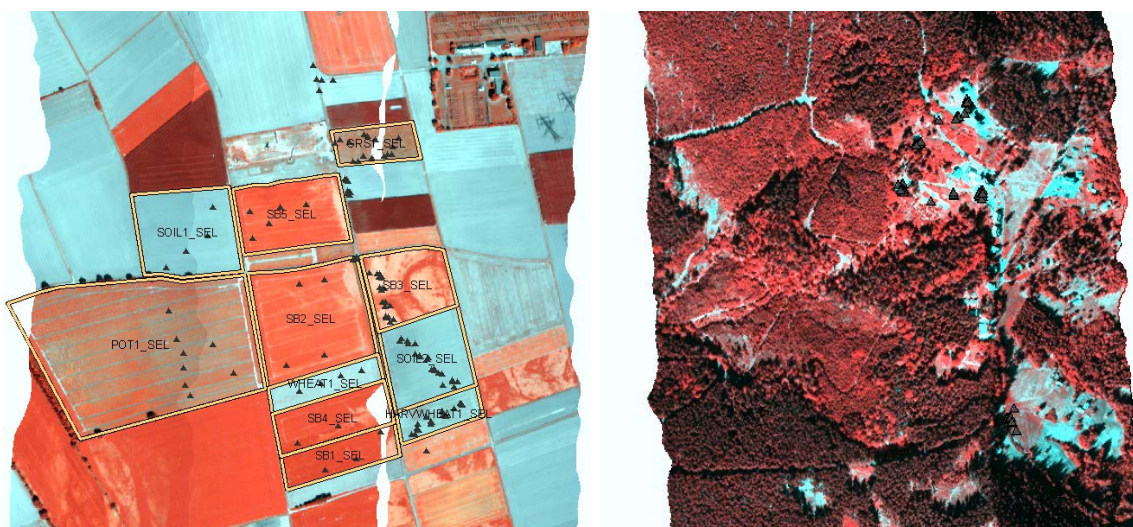


Figure 22: Location of ASD FieldSpec reference measurements in Selhausen (left) and Bílý Kříž (right). Underlying image is a false colour image of HyPlant flight lines.

4.3.1.2 Continuous monitoring of sun-induced fluorescence on selected intensive measurement sites

The S-FLUOR box is designed for high-temporal frequency acquisition of continuous radiometric measurements. It consists of two spectrometers (HR4000, OceanOptics, USA) characterised by different spectral resolutions. One spectrometer is characterised by a Full Width at Half Maximum (FWHM) of 0.2 nm and a 670–860 nm spectral range that can be used to estimate fluorescence at the O₂-A band (760 nm) and O₂-B band (686 nm). The second spectrometer (FWHM = 0.8 nm, 200–1100 nm spectral range) is used to compute vegetation indices. The spectrometers are housed in a Peltier thermally regulated box that maintains the internal temperature at 25°C in order to reduce dark current drift (Figure 23).



Figure 23: S-FLUOR box for continuous observation of spectral reflectance and fluorescence at different vegetation sites.

Spectrometers will be spectrally calibrated with known standards (Pen-Ray argon lamp, LOT Oriel Group, Germany), while the radiometric calibration will be inferred from cross-calibration measurements performed with a calibrated FieldSpec spectrometer (ASD, USA).

Measurements are acquired using a cosine-response optic to observe irradiance and a bare fibre optic with an angular FOV of 25° to observe the target surface. Signal is divided by a computer-controlled multiplexer (MPM-2000, OceanOptics, USA). Two S-FLUOR boxes provided by the Forschungszentrum Jülich will be available to the campaign.

In addition, the University of Milan will provide a similar optical system named MRI (Multiplexer-based Radiometer Irradiometer, Figure 24).



Figure 24: MRI system for continuous observation of spectral reflectance and fluorescence at different vegetation sites.

The MRI system, based on the same commercial optical multiplexer (MPM-2000, OceanOptics, USA), is able to switch between a channel measuring the incident irradiance (cosine response optic), a downward-looking bare fibre (FOV of 25°) for the measurement of the upwelling radiance, and a 'blind' channel for the dark current measurement. It also hosts two portable spectrometers (HR4000, OceanOptics, USA) operating in the visible and near-infrared region but with different spectral resolutions. The first one covers the 400–1000 nm spectral range with a full width at half maximum (FWHM) of 1 nm and allows the computation of vegetation indexes. The second one covers a finer resolution (FWHM = 0.1 nm) with a restricted spectral range

(700–800 nm) and is specifically intended for sun-induced fluorescence measurements in the O₂-A oxygen absorption band. The spectrometers will be spectrally calibrated with known standards (CAL-2000 mercury argon lamp, OceanOptics, USA), while the radiometric calibration will be inferred from cross-calibration measurements performed with a calibrated FieldSpec spectrometer (ASD, USA).

Finally, the University of Milan will also provide a Manual Spectrometric System (MSS) to allow additional measurements of high-resolution TOC radiances during the overpass (1 hour before and 1 hour after) (Figure 25). Also, this system is composed of two portable spectrometers (HR4000, OceanOptics, USA) operating in the visible 400–1000 nm spectral range with a FWHM of 1 nm and the 700–800 nm spectral range with a finer resolution (FWHM = 0.1 nm). Bare fibre optics with a FOV of 25° will be used alternately to measure a white reference calibrated panel (Optopolymer GmbH, Germany) and the target. Spectrometers will be spectrally calibrated with known standards (CAL-2000 mercury argon lamp, OceanOptics, USA) while the radiometric calibration will be inferred from cross-calibration measurements performed with a calibrated FieldSpec spectrometer (ASD, USA).

An overview of the location of the different continuous measurement systems is given in Table 12:



Figure 25: Portable spectrometer system in a sugar beet field in Selhausen.

Table 12: Overview of the continuous observation of spectral reflectance and fluorescence at different vegetation sites.

System	Date	Place	Species
MRI	23 Aug	Klein-Altendorf	sugar beet
MRI	27 Aug	Selhausen	grassland
MSS	23 and 27 Aug	Selhausen	sugar beet
S-FLUOR	3–9 Sept	Bílý Kříž	spruce (tower)
MSS	5 and 9 Sept	Bílý Kříž	spruce (hydraulic platform)
MIR	5 and 9 Sept	Bílý Kříž	grass carpet

4.3.2 Unmanned Arial Vehicle measurements

The Unmanned Arial Vehicle (UAV), a microdrones GmbH md4-1000 quadcopter that has a payload capacity of 1500 grams and a flight duration of 15–20 minutes, was used in autopilot mode, which allows an autonomous following of a predefined track. Flying this track, multiple images were acquired then combined into a mosaic. The UAV was equipped with two different sensors: a Tetracam Mini-MCA and a Zeiss UCM.

4.3.2.1 Tetracam Mini-MCA

The Tetracam Mini-MCA is a six-channel multispectral camera. The camera is composed of six individual detectors, each sensitive of 350 to 950 nm. The detector can be equipped with an individual filter that is chosen accordingly to the parameter that should be derived. For the Jülich campaign, the filters were chosen in order to calculate vegetation indices, such as PRI, NDVI, and a fluorescence index based on the fluorescence retrieval method published by Maier et al. (2003) using reflectance instead of radiance. Table 13 lists the different central wavelengths and the FWHM of every filter used:

Table 13: Central wavelength and FWHM for the filters used on the multispectral camera.

Central Wavelength [nm]	FWHM [nm]
530	10
580	10
670	10
750	10
760	1
780	10

Prior to index calculation, the data was atmospherically corrected using a midsummer latitude atmosphere with rural aerosol type and an assumed H₂O concentration of 2 g/cm². Because the sky had been partially covered with cirrus and cumuli clouds, images were taken with an automatic exposure setting; thus, histogram matching was applied to level out grey value differences between overlapping image areas.

4.3.2.2 Zeiss UCM

The second sensor that was used in combination with the UAV was a Zeiss uncooled module UCM, which is a broadband, thermal infrared camera, sensitive from 7–14 µm. The camera does not provide temperatures but raw DN values. In order to obtain actual temperature values, calibration is needed, which was not performed during the Jülich campaign.

The UAV measurements were taken above the sugar beet experiment site in Klein-Altendorf on 22 and 23 August 2012. On 23 August 2012, diurnal UAV flights were carried out using the multispectral camera over the same sugar beet field at Klein-Altendorf where the Milan group had their tower installed. From the multispectral imagery, multiple indices and products such as the photochemical reflectance index (PRI) and the normalised difference vegetation index (NDVI) were derived (Figure 26, *left*). From the thermal camera, only raw DN values were derived (Figure 26, *right*).

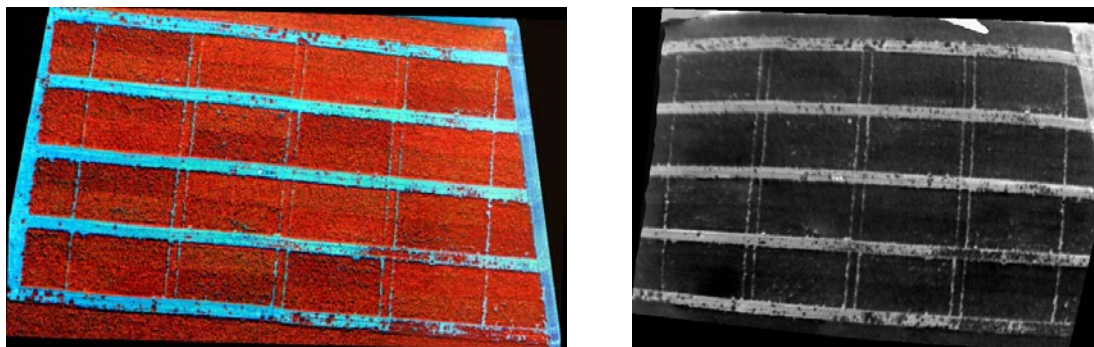


Figure 26: RGB-composite of the 6-channel multispectral camera (*left*) and thermal mosaic (*right*).

4.3.3 Characterisation of atmospheric properties to test the influence of atmospheric variations on the signal and for atmospheric correction

Knowledge of the atmospheric conditions, especially the aerosol optical depth (AOD), its vertical profile and the water content, is required to perform accurate atmospheric correction. During the campaign two instruments for accurate characterisation of atmospheric parameters were employed.

4.3.3.1 Cimel sun photometer (1 University of Valencia)

The CE318 is a commercial sun photometer designed for the automatic measurement of direct solar irradiance and sky radiance. The unit measures in channels centred at 340, 380, 440, 500, 670, 870, 940, 1020, and 1640 nm, with the 940 nm channel dedicated to obtaining the atmospheric columnar water vapour and with the 1640 nm channel dedicated to obtaining Aerosol Optical Depth (AOD) at 1640 nm. The full width at half maximum (FWHM) of each channel varies from 2 to 40 nm, shorter for the UV and wider for the 1640 nm. In the VIS range, the bandwidth is about 10 nm. The sensor head is equipped with a double collimator with a 1.2° field of view. Due to issues with the calibration file of the Cimel sun photometer, the data could not be used for further analyses.

4.3.3.2 Lidar (operated by the National Observatory of Athens, NOA)

EMORAL (Esa's MOBILE Raman Lidar) is a portable depolarisation, Raman lidar mounted in a minivan (Figure 27 (A)), capable of detecting polar and cross-polar signal at 355 nm, total linear polarised signal at 532 nm, and nitrogen's Raman return at 387 nm. The emitter consists of three subunits, the laser source the reflective mirrors, and the beam expander units. The laser source is a pulsed Nd:YAG laser (CFR 400) operating at 1064 nm (145 mJ), 532 nm (120 mJ), and 355 nm (72 mJ). The pulse repetition rate is 10 Hz, and the pulse FWHM is 8.3 ns. The beam divergence at 86.5% of energy is 0.8 mrad for both second and third harmonics before the beam expanders. The beam expander unit contains two expanders with beam expansion factor $\times 4$, for the two wavelengths of interest (355 nm, 532 nm). This reduces the beam divergence of the two beams down to 0.2 mrad at the exit windows of the system (separate windows for each wavelength, symmetrically positioned on one side of the telescope) (Figure 27 (B)).

The receiving system consists of a Cassegrain telescope and the wavelength separation/detection optical box. The diameter of telescope's primary mirror is 400 mm and the focal length 4000 mm, coated with HR coatings and with very small thermal expansion coefficient. The diaphragm, mounted beneath the primary mirror, has adjustable diameter (from

1 mm up to 12.5), depending on the atmospheric conditions and the strength of the aerosol load, giving the ability to detect from the lower to upper atmosphere. The spectrometer (optical box) is equipped with dielectric dichroic beam splitters (BS) to separate the three backscattered lidar signals at wavelengths 355 nm, 532 nm (elastic lidar signals) and 387 nm (Raman lidar signal). A polarised beam splitter cube is additionally mounted in order to separate the backscattered polar and cross-polar signal at 355 nm (Figure 27 (C)). Very narrow band interference filters (<1 nm at FWHM) are used to suppress the atmospheric background light, which affects all the signals and especially the backscattered Raman signal. Photo-multiplier tubes-PMTs - operated both in the analog and photon-counting mode – are employed in order to detect the lidar signals at 355, 387, and 532 nm. The combination of powerful A/D converters (12 Bit at 40 MHz) with a 250 MHz fast photon counting systems provides a spatial raw resolution of the detected lidar signals of 7.5 m, for the acquired and stored lidar signals. The National Observatory of Athens (NOA) currently operates EMORAL system.

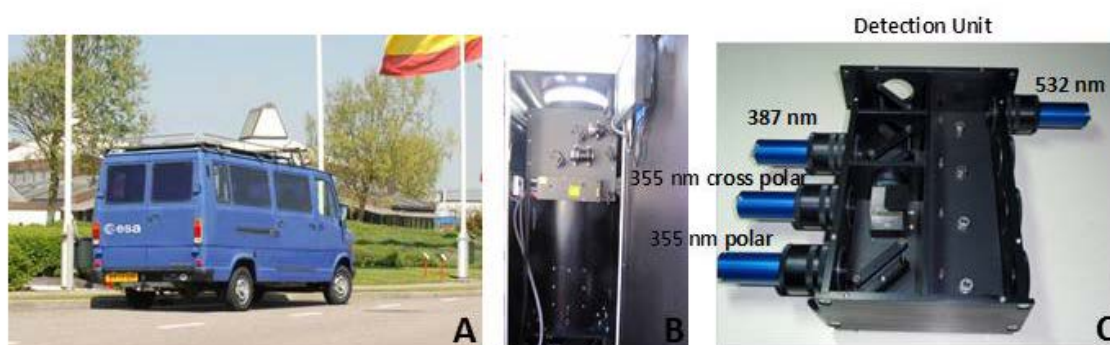


Figure 27: (A) ESA's Minivan; (B) Emission Unit of EMORAL; (C) Detection Unit of EMORAL.

In August 2012, the EMORAL started travelling to Northern Europe in order to participate in HYFLEX campaign, taking place in Jülich, Germany, and later, in September 2012, in Bílý Kříž, Czech Republic. The starting point was Athens, Greece, since systematic lidar measurements were performed there from February 2012.



Figure 28: a) Travel route from Athens (Greece) to Jülich (Germany); b) EMORAL located in Selhausen; c) EMORAL during operation in Selhausen; d) travel route from Jülich (Germany) to Bílý Kříž (Czech Republic); e) installation on field; f) ready for measurements on forest.

4.3.4 Characterisation of the structural and functional status of vegetation using leaf and canopy level methods

Structural and functional status of vegetation was characterised at the leaf and at the canopy level (Table 15, Figure 29). The parameters were used in forward modelling to validate and understand the airborne measurements of sun-induced chlorophyll fluorescence and at-sensor reflectance.

Actual leaf-level fluorescence emission spectra were measured using the FLUOWAT device. For the same leaves, biochemical measurements (e.g., chlorophyll content, water content) were collected. Canopy structural parameters (e.g., canopy height, leaf area index) are needed to scale from the leaf to the canopy.

Table 15: In-situ functional and structural measurements.

In-situ measurements	Definition	proposed method
Leaf-level		
Fluorescence ratio	Fluorescence emission at 690 and 740 nm will be quantified at a representative number of leaves within the canopy.	Custom made hand-held instrument (FLUOWAT).
Chlorophyll content	Leaf chlorophyll content will be quantified at a representative number of leaves within the canopy using the SPAD. For calibration of SPAD data, chlorophyll content will be determined biochemically by pigment extraction.	Leaf-level absorbance measurements in the red and near-infrared (SPAD) and biochemical pigment extraction.
Cw (Leaf Water Content); Cdm (Leaf Dry Matter Content)	The amount of water and leaf dry matter in weight per unit of leaf surface will be measured in the lab using fresh and oven dried leaves.	Leaf samples in the field and drying and weighing in the lab.
Canopy-level		
Plant structural parameters	Vegetation height that will be used for the canopy radioactive transfer modelling will be determined in the field.	Basic algometric measurements.
LAI (Leaf area index)	LAI is the area of foliage per unit area of ground. LAI can be quantified by harvesting a 50 x 50 cm plot of biomass and analyse it afterwards in the lab.	LAI measurements with the LI-3100C Area Meter.

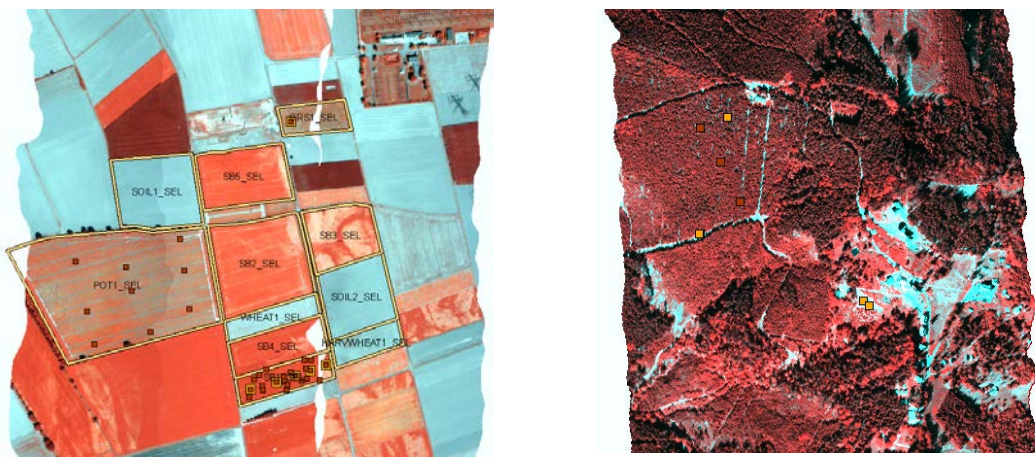


Figure 29: Location of leaf area index (brown marks) and chlorophyll measurements (yellow marks) of the Selhausen (*left*) and Bílý Kříž (*right*) measurement site.

4.3.5 Measurements of canopy photosynthesis using eddy covariance techniques

Flux measurements at the surface are related to friction velocity, energy budget, and fluxes of trace species. In general, on the various sites of TR32 and CzechGlobe, the friction velocity and energy budget are measured together with the flux of CO₂. Because the surface energy balance is expressed as the distribution of net radiation R_n into sensible heat flux (H), latent heat flux (LE), and ground heat flux (G), the equipment consists of a 3D sonic anemometer, an infrared gas analyser measuring CO₂ and H₂O concentrations, and one or several radiation sensors. Friction velocity (u*), H, LE, and CO₂ flux are calculated using the eddy covariance technique.

Continuous measurements of net CO₂ ecosystem exchange rates were acquired during the campaigns. Those data can be used to derive gross primary productivity (GPP) (Reichstein et al. 2005). GPP time series can be used to investigate the link between photosynthesis and TOC sun-induced fluorescence.

4.3.6 Thermal measurements

A hyperspectral, thermal, infrared imaging spectroscope was mounted on top of the tower in Klein-Altendorf. The imaging spectrometer is the Telops Hypercam, which has a FPA of 320 x 256 pixels (Figure 30). The detector has a sensitivity from 7.7µm to 11.9 µm with a variable spectral resolution. In this field campaign, a spectral resolution of 126 channels in the thermal spectral domain was chosen. The camera was mounted on a tower, allowing an oblique view of the complete field. The oblique view caused some severe difficulties during processing of the data. On the one hand, the path through the atmosphere was very heterogeneous, which made atmospheric correction almost impossible. On the other hand, the constantly changing oblique view prevented the adequate georeferencing of the data. The Hypercam recorded data on 23 August 2012.



Figure 30: Hypercam mounted on tower in Klein-Altendorf.

Although it was difficult to georeference the different images, a diurnal course of leaves' temperatures could be derived. We could not identify variations in spectral emissivity resulting from different treatments or heat stress could not be identified.

4.4 Campaign database

4.4.1 Data archive

A secure FTP server has been set up to ensure fast, fair, and constructive data exchange and joint analyses.

FTP site access:

Host: sftp://134.94.64.97

Port: 22

For user name and password, please contact u.rascher@fz-juelich.de, f.pinto@fz-juelich.de, or a.schickling@fz-juelich.de.

FTP site content

The FTP server contains the acquired and processed data, organised as follows:

/incoming/01- Finland Campaign- July 2012
 /incoming/02- Luxemburg test- August 2012
 /incoming/03- Juelich Campaign- August 2012
 /incoming/04- Czech Rep campaign- September 2012
 /incoming/05- GIS HyPlant 2012
 /incoming/06- Results 2012

Campaign related documents (reports, presentations):

/Reports/HYFLEX 2012

The stored data documented by the various working groups. The server is regularly checked and backed up. A complete copy of the data of the ftp server is delivered with this final report on a portable hard drive, according to the agreement of the negotiation meeting.

4.4.2 Campaign GIS

A Geographical Information System (GIS), based on the commercial software package ArcGIS was developed to provide a proper overview about the data and their spatial overlap and to simplify the data access using attributive and spatial queries. This spatial database contains most of the acquired data sets, including airborne and ground base measurements (Table 16).

Table 16: Data organisation of the GIS database.

Level 1	Level 2	Level 3	Description
GIS_HYPLANT2012	BK	BK_img	Folder with GIS images*
		BK_shape	Folder with GIS shapefiles
		BK_xls	Folder with database (Excel files) used for shapefiles
		Bily Kříž.mxd	GIS
	CKA	CKA_img	Folder with GIS images**
		CKA_shape	Folder with GIS shapefiles
		CKA_xls	Folder with database (Excel files) used for shapefiles
		Kleinalten-dorf.mxd	GIS
	SEL	SEL_img	Folder with GIS images***
		SEL_shape	Folder with GIS shapefiles
		SEL_xls	Folder with database (Excel files) used for shapefiles
		Selhausen.mxd	GIS
	Overview	-	Overview on database and GIS (this document)

The image data of the GIS database are based on recorded HyPlant data. All produced vector data were provided in the *.shp data format at the FTP server. Additionally, an ArcGIS project (*.mxd) consisting of the vector data is listed in Table 17 (also refer to Figure 31).

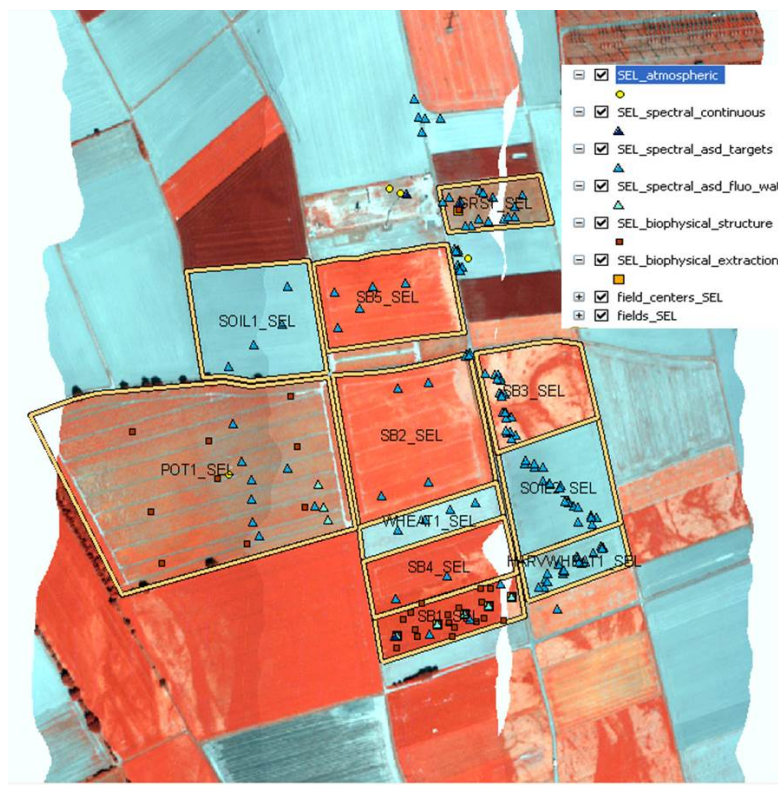


Figure 31: Overview of the measurements at the Selhausen site (*.mxd file). False colour images of HyPlant fluorescence imager.

Table 17: Structure of the ArcGIS Project files.

File	Layer Category	Layer Name	Content
Bílý Kříž.mxd	Atmospheric measurements	BK_atmospheric	Cimel, Microtops, lidar, eddy, and meteorological
	Spectral measurements	BK_spectral_continuous	Fluo box, manual system, ASD, and irradiance
		BK_spectral_asd_targets	ASD
	Biophysical measurements	BK_biophysical_extractions	Pigment, N and C extractions
		BK_biophysical_structure	LAI
	Land use reselected flight lines	1310FLUO600.tif 1334FLUO1800.tif	Land use of the reselected flight lines
	Area (600 m)	20120909-BK-1527-600-L1-FLUO-rect.tif 20120909-BK-1304-600-L2-FLUO-rect.tif 20120909-BK-1310-600-L3-FLUO-rect.tif	Measured area, 600 m flight lines
Kleinalten-dorf.mxd	Atmospheric measurements	CKA_atmospheric	Microtops, meteo
	Spectral measurements	CKA_spectral_continuous	Fluo box and MRI
		CKA_spectral_asd_targets	ASD
	Biophysical measurements	CKA_biophysical_extractions	Pigment extractions
		CKA_biophysical_structure	Biomass and LAI
	Fields	fields_CKA	Measured fields borders
		field_centres_CKA	Measured fields centres with text labels
	Land use	mosaic_CKA_land_use.tif	Land use
	Area (600 m)	20120823-CKA-1115-0600-L1-FLUO-rect.tif 20120823-CKA-1121-0600-L2-FLUO-rect.tif 20120823-CKA-1539-0600-L3-FLUO-rect.tif	Measured area, 600 m flight lines
Selhausen.mxd	Atmospheric measurements	SEL_atmospheric	Cimel, Microtops, lidar, eddy, and meteo
	Spectral measurements	SEL_spectral_continuous	Manual system, MRI and irradiance
		SEL_spectral_asd_targets	ASD
		SEL_spectral_asd_fluo_wat	FluoWat
	Biophysical measurements	SEL_biophysical_extractions	Pigment extractions
		SEL_biophysical_structure	Biomass and LAI
	Fields	fields_SEL	Measured fields borders
		field_centers_SEL	Measured fields centres with text labels
	Land use	mosaic_SEL_land_use.tif	Land use
	Land use reselected flight lines	1350FLUO600.tif 1423FLUO1780.tif	Land use of the reselected flight lines
	Area (600 m)	20120823-SEL-1150-0600-L1-FLUO-rect.tif 20120823-SEL-1350-0600-L2-FLUO-rect.tif 20120823-SEL-1204-0600-L3-FLUO-rect.tif	Measured area, 600 m flight lines

5 Results

5.1 Weather conditions during the campaign

5.1.1 Agriculture, Jülich campaign, Germany

Meteorological parameters during the measurement period (21–31 August) are shown in Figure 32. Maximum PAR values reached up to 1600 $\mu\text{mol}/\text{m}^2/\text{s}$ under clear sky conditions. Air temperature showed highest values at the beginning of the measurement period. On airborne observation days (DOY 235, 236, and 240), air temperature values did not exceed 25°C. Relative humidity showed minimum values with highest temperature values.

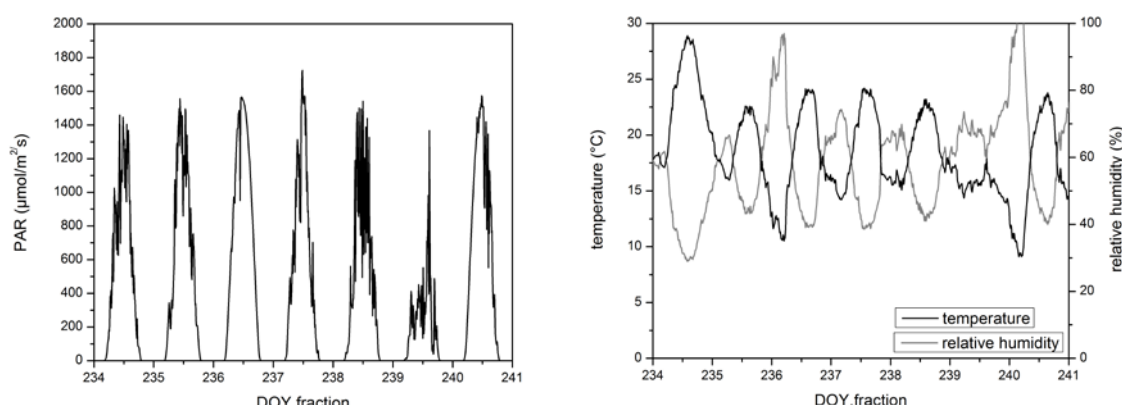


Figure 32: Photosynthetic active radiation (PAR, *left*), temperature and relative humidity (*right*) in Selhausen during the measurement period.

5.1.2 Forest, Bílý Kříž campaign, Czech Republic

Meteorological parameters of Bílý Kříž were recovered above the spruce forest (Figure 33, 4–11 September). PAR values showed maximum values up to 1200 $\mu\text{mol}/\text{m}^2/\text{s}$ on clear sky days. Air temperature showed maximum values of 27°C during the measurement period. The relative humidity of Bílý Kříž was in general higher than that of the Selhausen measurement site, the former showing saturated conditions during the night at the beginning of the measurement period.

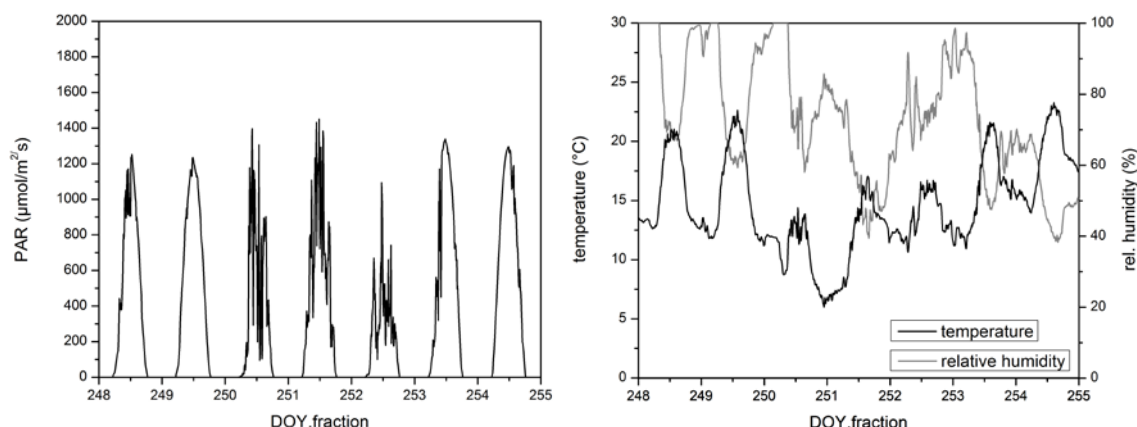


Figure 33: Photosynthetic active radiation (PAR, *left*), temperature and relative humidity (*right*) in Bílý Kříž during the measurement period.

5.2 Atmospheric characterisation

5.2.1 Agriculture

5.2.1.1 Selhausen, 22 August 2012

On 22 August, EMORAL was operating in Selhausen from 08:53 to 13:39 UTC (Figure 34). During this time period, high-altitude (10 to 11 km) cirrus clouds with thickness ranging from 1.5 to 0.3 km were present over the experimental site. During the day, some scattered low-altitude (below 2 km) cumulus clouds developed above the Planetary Boundary Layer (PBL); stable illumination conditions prevailed on the ground. The PBL height during the measurement period ranged from 1004.9 m up to 1818.3 m, trapping all aerosol load produced by local sources, while during the morning hours (08:53–10:00 UTC) a free tropospheric layer was observed at 7.5 km with 1 km thickness.

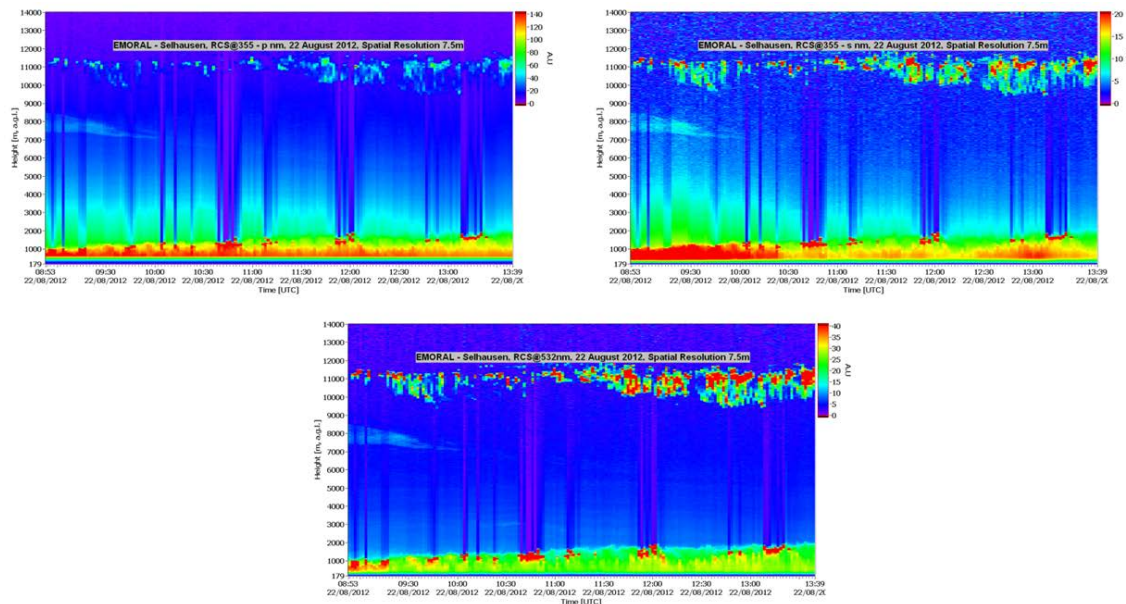


Figure 34: Range-Corrected lidar Signal (RCS, in Arbitrary Units) obtained by EMORAL at 355-p, 355-s, and 532 nm over Selhausen (Germany) on 22 August 2012.

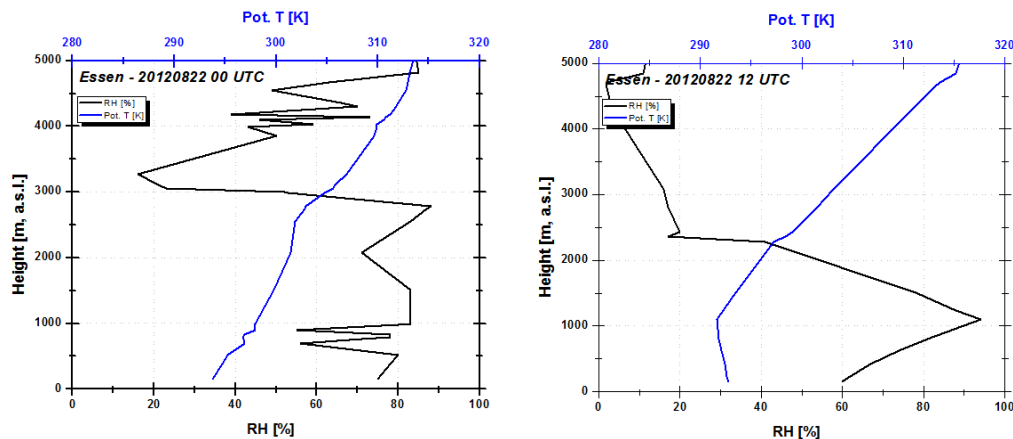


Figure 35: Vertical profiles of Relative Humidity (%) and Potential Temperature (°K) for Essen on 22 August at 00:00 UTC and 12:00 UTC.

Approximately 90 km north eastern of Selhausen, in Essen, radiosondes are launched every day at 12:00 and 00:00 UTC (<http://www.weather.uwyo.edu/upperair/sounding.html>). The soundings provide vertical distribution of temperature, relative humidity, and wind speed/direction during the entire campaign period in Germany. No meteorological balloons were available in the exact campaign spot. Assuming that there are uniform conditions in this greater area, we can use those data to have an initial idea about the prevailing meteorological situation. In the lower part of the troposphere (below 2 km), high relative humidity values were measured, ranging from 60% to 90% (22 August at 00:00 and 12:00 UTC; Figure 35). Those values greatly contribute to the cloud formation. This was already verified by the lidar, which detected clouds in the lower troposphere. In addition, the level 1.5 (cloud screened) AERONET data from Jülich site (http://aeronet.gsfc.nasa.gov/cgi-bin/type_one_station_opera_v2_new?site=FZJ-JOYCE&nachal=2&level=2&place_code=10) verify the existence of clouds in the greater area.

5.2.1.2 Selhausen, 23 August 2012

On 23 August, EMORAL took measurements in Selhausen from 09:57 to 14:56 UTC (Figure 36). The atmospheric conditions were homogeneous with stable aerosol layers but no turbulence during the entire time period. Some scattered ice-formed cirrus clouds were detected. They were denser during the first period of flights (09:50–10:25 UTC) and ranged in altitudes from 8 km up to 10.5 km. The PBL height during the measurement period varied from 1 km up to 1.8 km, trapping all aerosol load produced by local sources. A stable mid-altitude (1.5–3.8 km) aerosol layer overlay the PBL height, while a thinner, low, depolarising aerosol layer was detected in higher troposphere (7–8 km).

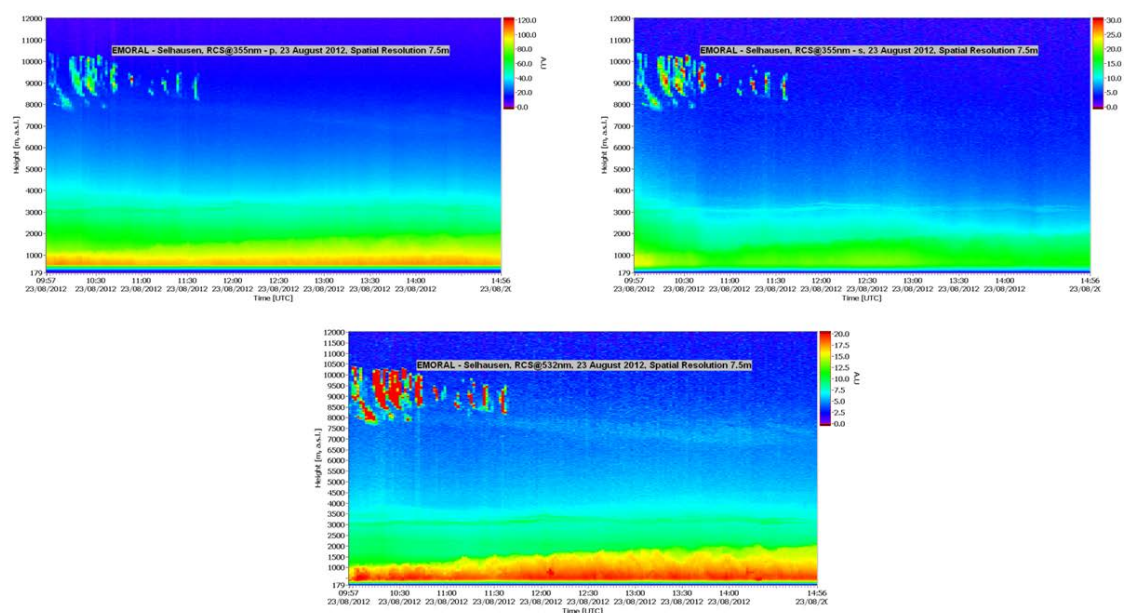


Figure 36: Range-Corrected lidar Signal (RCS, in Arbitrary Units) obtained by EMORAL at 355-p, 355-s, and 532 nm over Selhausen (Germany) on 23 August 2012.

In general, illumination conditions were much better and cloud free time windows were larger on 23 August than on 22 August, which gave us the opportunity to analyse lidar and sun photometric data more in detail (Figure 36). On 23 August (12:00 UTC), lower RH values, ranging from 20 to 60%, were found in the lower troposphere (Figure 37).

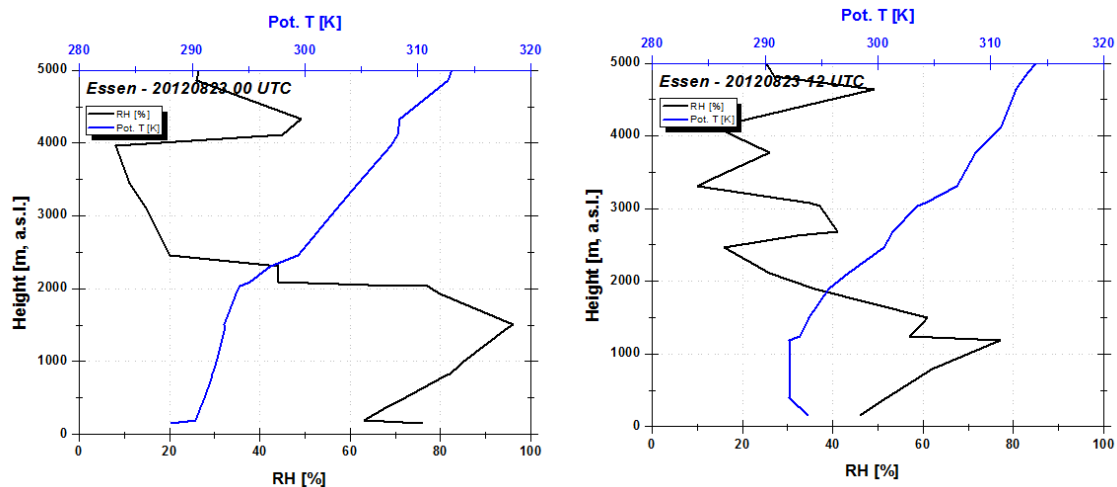


Figure 37: Vertical profiles of Relative Humidity (%) and Potential Temperature (°K) for Essen on 23 August at 00:00 UTC and 12:00 UTC.

The fit of the normalised lidar signals at 532 and 355 nm (Figure 38) corresponds well to the molecular atmosphere at 11 km and 10 km respectively, ensuring good data quality, system performance, and alignment (Figure 38).

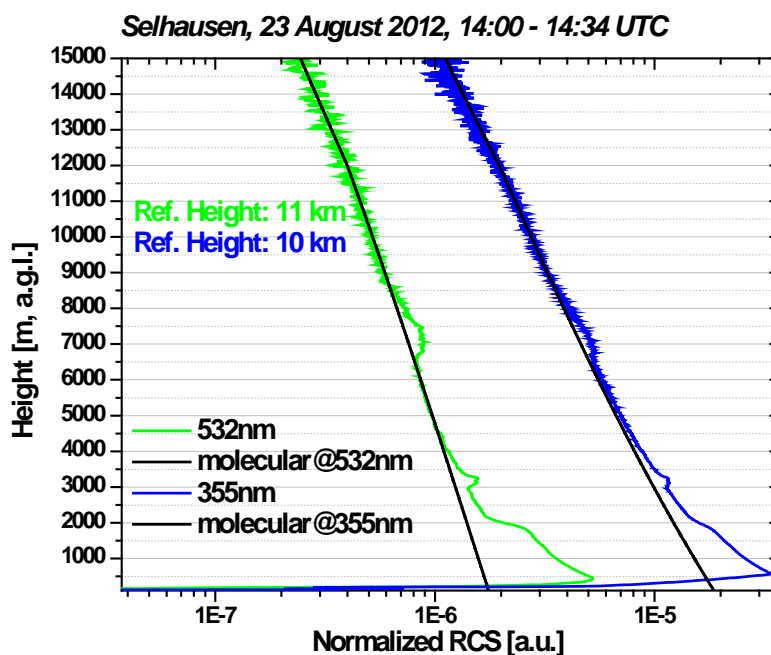


Figure 38: Normalised Range Corrected lidar signals at 532 and 355 nm, on 23 August 2012, fitted to Rayleigh atmosphere.

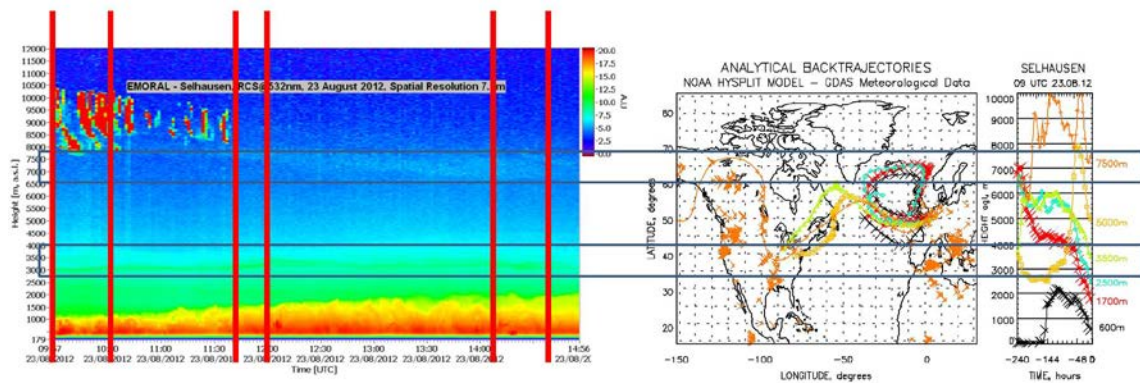


Figure 39: RCS at 532 nm recorded by EMORAL (*left*) and ten-day back trajectory analysis of air masses arriving over Selhausen at different heights in August 2012. Vertical red lines mark the time window of the airborne data acquisition, and grey horizontal lines mark the height aerosol layer height.

In order to identify the origin of the aerosol detected in Selhausen, a ten-day back trajectory analysis was performed on the air masses arriving over Selhausen at different heights (Figure 39, *right*) on 23 August 2012 (09:00 UTC). Vertical red lines (Figure 39, *left*) indicate the time window of the overpasses, while with the grey horizontal lines indicate the height of the aerosol layers. From this analysis, it is clear that the aerosol layers detected over Selhausen at the heights of 3.5 and 7.5 km originated from areas in southern Canada with biomass burning activities.

Table 18: Plane flights over Selhausen and lidar data averaging period during 23 August.

	1 st	2 nd	3 rd
Time [UTC]	09:50 -10:25 (600m a.g.l.)	11:42 -11:58 (600m a.g.l.)	14:02 -14:31 (600m a.g.l.)
	Averaging lidar data		
Time [UTC]	09:59-10:27	11:41 – 12:00	14:00 -14:34

Table 18 contains the time of the airborne data acquisition over Selhausen and the time period used for the lidar signal averaging. Both low- and high-altitude flight lines (600 and 1780 m, agl) over Selhausen, were inside the PBL height range.

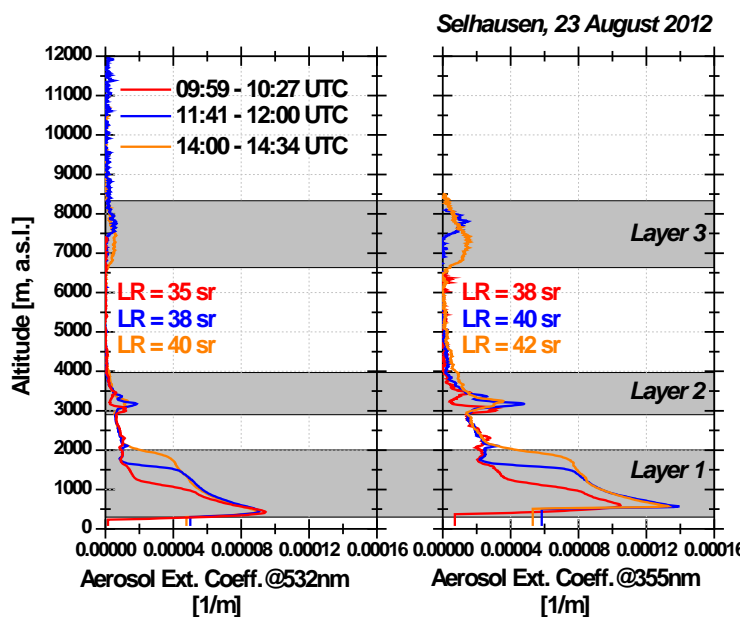


Figure 40: Vertical profiles of the aerosol extinction coefficient at 532 nm and 355 nm (in 1/m), retrieved by EMORAL, during the three flight periods, over Selhausen on 23 August 2012. Colours indicate time of the overpasses; red (09:59–10:27 UTC), blue (11:41–12:00 UTC), and orange (14:00–14:34 UTC).

In Figure 40, the aerosol extinction profiles at 532 nm and 355 nm are given. The three time periods of the overpasses are highlighted in different colours; red (09:59–10:27 UTC), blue (11:41–12:00 UTC), and orange (14:00–14:34 UTC). Three distinct aerosol layers were identified from ground level up to 8 km. The table below (Table 19) summarises the mean aerosol extinction values (at 355 and 532 nm) in the three aforementioned layers on 23 August.

Table 19: Table summarising the mean aerosol extinction values at 355 and 532 nm for each layer and time period.

09:59–10:27 UTC	Aerosol Ext. at 532 nm [1/m]	Aerosol Ext. at 355 nm [1/m]
Layer 1 (105–1727 m)	4.74E-05 ± 2.74E-05	6.00E-05 ± 2.87E-05
Layer 2 (2766–4008 m)	5.08E-06 ± 2.83E-06	1.03E-05 ± 8.36E-06
Layer 3 (-)	NaN	NaN
11:41–12:00 UTC		
Layer 1 (105–1727 m)	5.96E-05 ± 1.82E-05	8.16E-05 ± 3.24E-05
Layer 2 (2766–4008 m)	6.22E-06 ± 4.34E-06	1.45E-05 ± 1.21E-05
Layer 3 (7394–8100 m)	3.13E-06 ± 2.06E-06	7.98E-06 ± 3.55E-06
14:00–14:34 UTC		
Layer 1 (105–2019 m)	5.78E-05 ± 1.52E-05	8.69E-05 ± 1.99E-05
Layer 2 (2766–4008 m)	5.25E-06 ± 3.32E-06	1.36E-05 ± 8.63E-06
Layer 3 (6528–8498 m)	3.16E-06 ± 1.75E-06	8.48E-06 ± 4.57E-06

*The error values indicate the property variation and not the actual error.

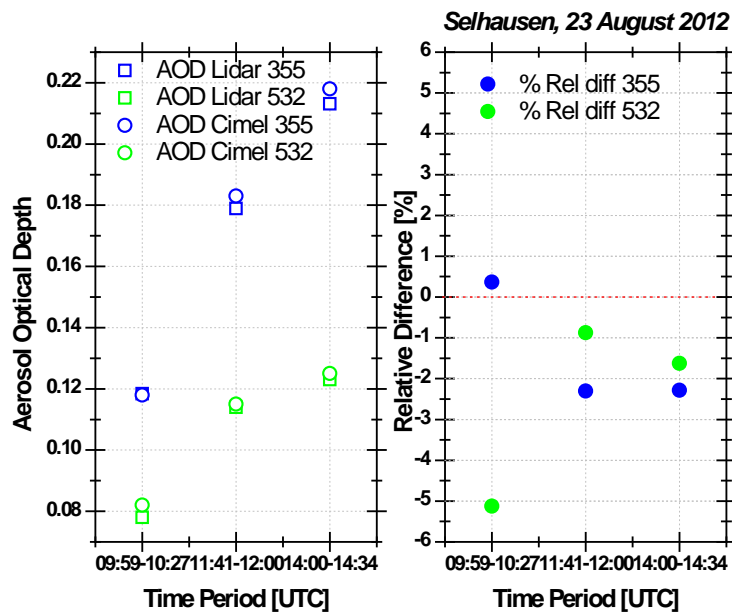


Figure 41: Aerosol extinction coefficient at 532 nm on August 23rd in Selhausen.

The AOD (at 355 nm and 532 nm) retrieved from lidar and the Cimel measurements are shown in Figure 41. Good agreement between the two instruments was found. Their absolute relative difference varied from 0.3 to 2.2 at 355 nm and from 0.8 to 5.1 % at 532 nm. The AOD at 532 nm showed a value of 0.118 at the early morning measurement (09:59 UTC). This value increased to 0.211 (14:00 UTC) due to the anthropogenic activity. Those AOD values in combination with the small Angstrom exponent (ranging from 1.1 up to 1.4), and with the small LR values, are most likely linked with a continental aerosol type as a major component in the atmospheric column.

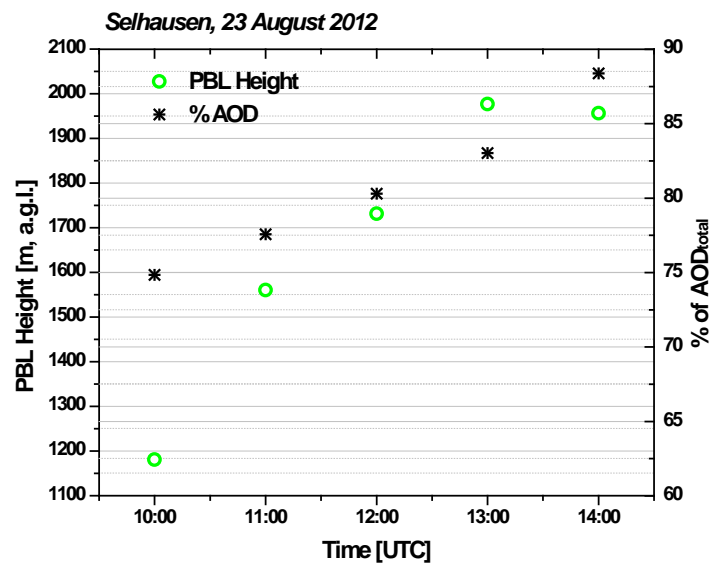


Figure 42: Hourly variability of PBL height and percentage of AOD trapped in Selhausen on 23 August.

By analysing hourly averaged lidar data, we were able to observe the PBL height evolution in Selhausen and correlate it with the AOD at 532 nm, directly linked to the aerosol layer trapped below this physical border (Figure 42). The PBL height ranged from 1181.6 m up to 1977.2 m. The aerosol load trapped below those height ranges contributed from 75% to 87% to the total AOD at 532 nm retrieved by lidar measurements. This 25% to 13% difference is related to the atmospheric extinction produced by the low-mid and high tropospheric aerosol layers (layer 2, layer 3 in Figure 40). Those values could be even higher in mid-latitude regions (e.g., Eastern Mediterranean), where transboundary pollution is more pervasive (Amiridis et al. 2010, Kokkalis et al. 2013, Papayannis et al. 2009).

5.2.1.3 Selhausen, 27 August 2012

Figure 43 shows the range-corrected lidar signal (Arbitrary Units) obtained by EMORAL at 532, 355-p, and 355-s nm over Selhausen on 27 August 2012. During the measurement period (08:11 to 14:28 UTC), cirrus clouds were detected at heights between 9 and 12 km. In addition, some scattered cumulus clouds formed at the top of boundary layer (~ 2 km) after local noon (approximately 12:00 UTC). Once again, high relative humidity values (up to 90%) were observed at low altitudes (Figure 44).

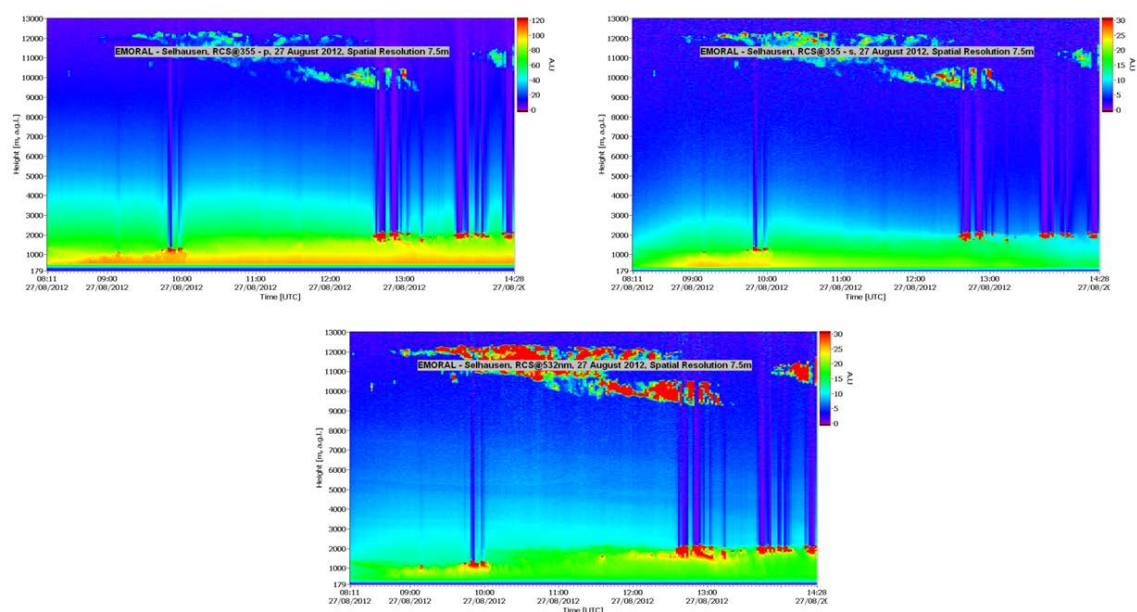


Figure 43: Range-Corrected lidar Signal (RCS, in Arbitrary Units) obtained by EMORAL at 355-p, 355-s, and 532 nm over Selhausen (Germany) on 27 August 2012.

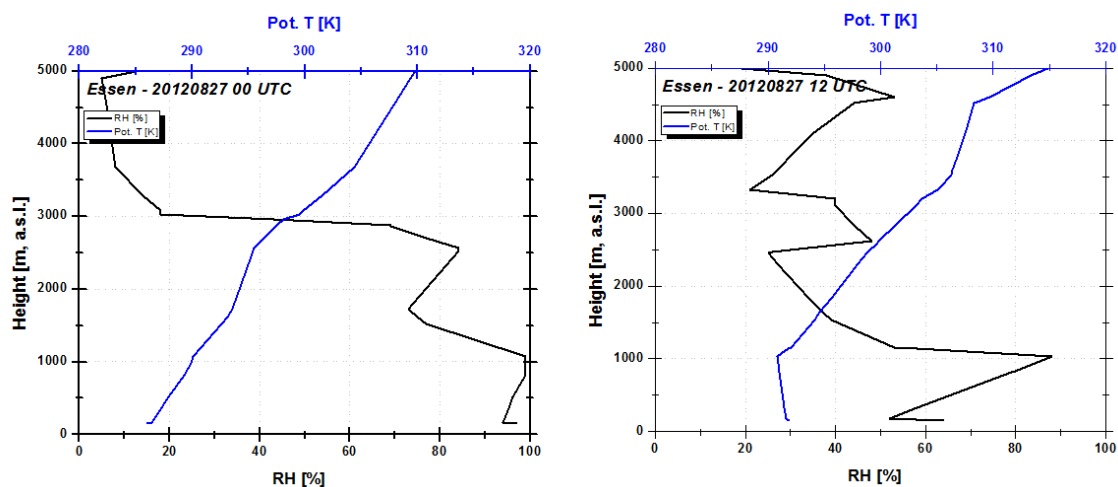


Figure 44: Relative Humidity (%) and Potential Temperature (°K) retrieved by radiosondes launched at 00:00 UTC and 12:00 UTC on 27 August.

5.2.2 Forest

5.2.2.1 Bílý Kříž, 3 September 2012

Figure 45 presents the range-corrected lidar signal obtained by EMORAL at 532, 355-p, and 355-s nm over Bílý Kříž on 3 September 2012. An intense aerosol layer up to 1.5 km height above ground could be clearly protected. During the period of measurement (12:15 to 15:00 UTC), mid-tropospheric clouds were detected at the height of approximately 5 km. The only cloud-free window occurred between 13:00 and 14:00 UTC.

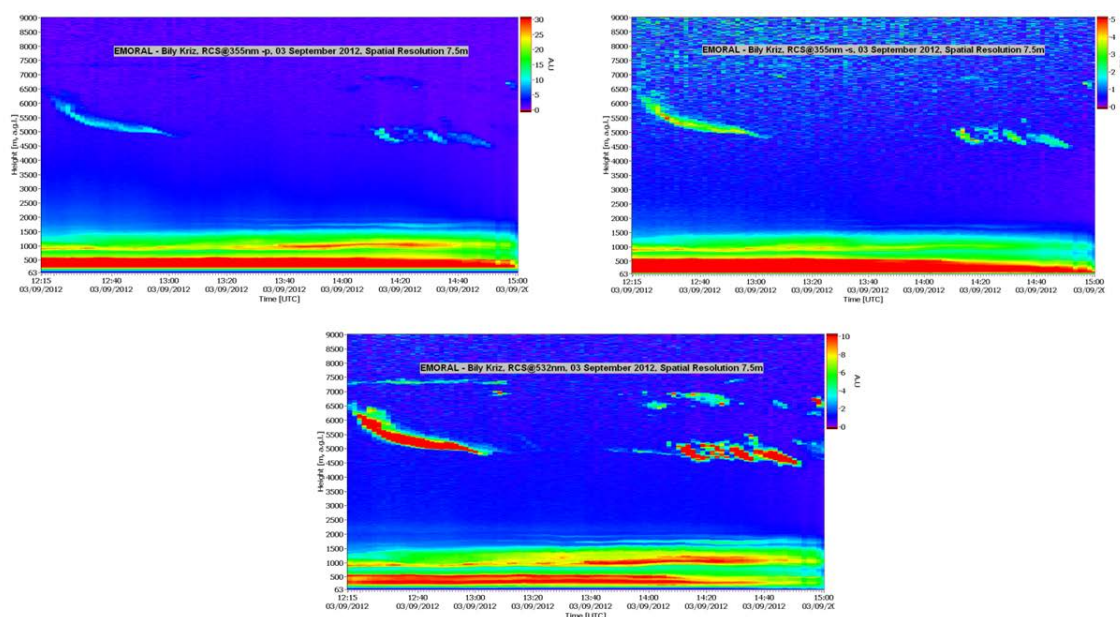


Figure 45: Range-Corrected lidar Signal (RCS, in Arbitrary Units) obtained by EMORAL at 355-p, 355-s, and 532 nm over Bílý Kříž (Czech Republic) on 3 September 2012.

5.2.2.2 Bílý Kříž, 4 September 2012

On 4 September 2012, EMORAL was operating in Bílý Kříž from 12:26 to 14:15 UTC. Figure 46 presents the recorded range-corrected lidar signal at different wavelengths (532, 355-p, and 355-s nm). Aerosol layers were detected at low altitude (from ground up to 1.7 km above ground level).

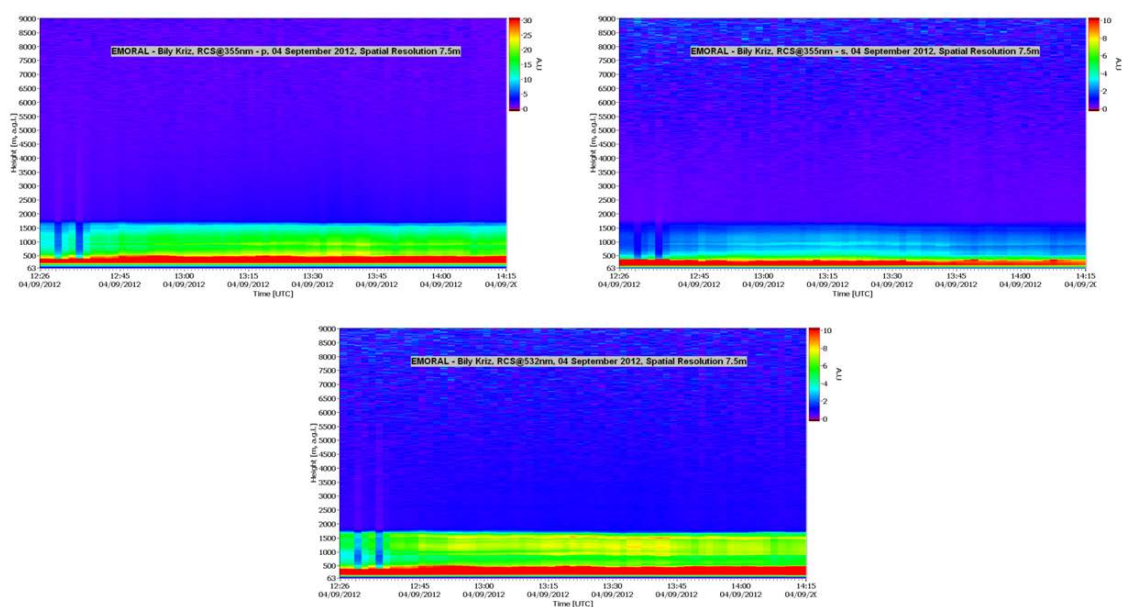


Figure 46 Range-Corrected lidar Signal (RCS, in Arbitrary Units) obtained by EMORAL at 355-p, 355-s, and 532 nm over Bílý Kříž (Czech Republic) on 4 September 2012.

5.2.2.3 Bílý Kříž, 5 September 2012

On 5 September 2012, several distinct low-altitude aerosol layers (with a centre of mass at 2.5 km) were observed by EMORAL during the measurement period 07:57–14:34 UTC. Some thin, high-altitude clouds appeared once in a while at 7 km above sea level (Figure 47). From the logarithm of the RCS signal at 532 nm (Figure 48), we can observe that the temporal evolution of the PBL top height ranged from 1.5 km to 1.75 km above sea level.

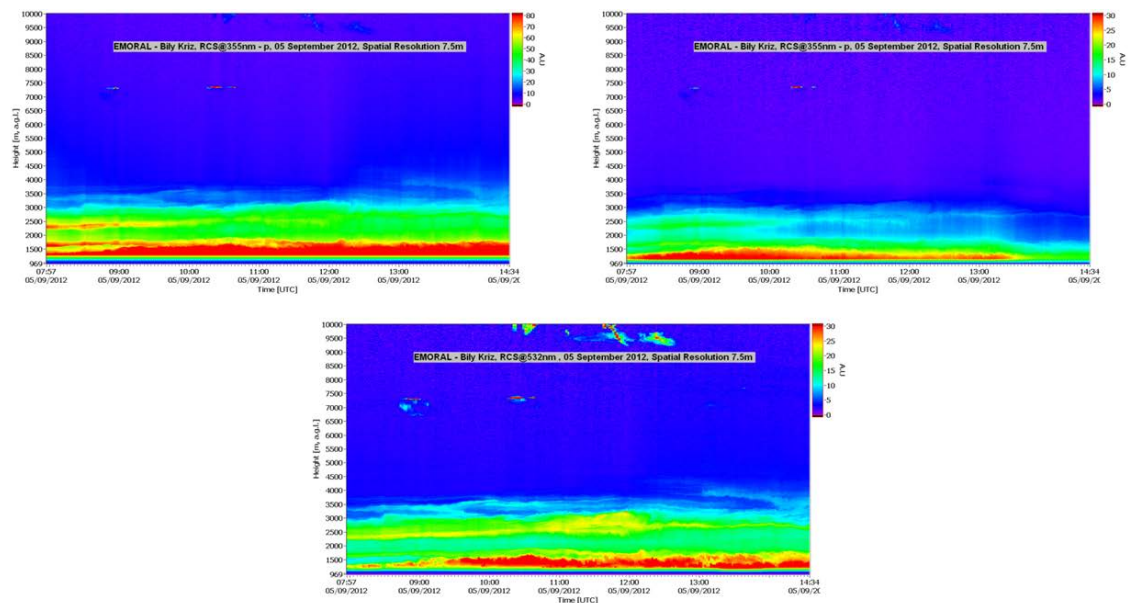


Figure 47: Range-Corrected lidar Signal (RCS, in Arbitrary Units) obtained by EMORAL at 355-p, 355-s, and 532 nm over Bílý Kříž (Czech Republic) on 5 September 2012.

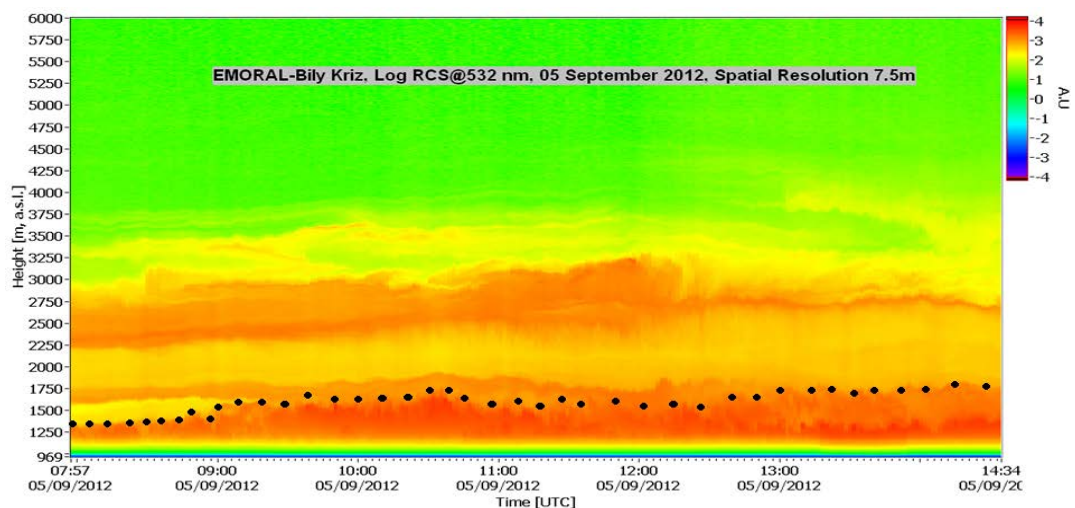


Figure 48: The logarithm of the Range-Corrected lidar Signal (LogRCS, in Arbitrary Units) obtained by EMORAL at 532 nm over Bílý Kříž (Czech Republic) on 5 September 2012.

Table 20: Plane flights over Bílý Kříž and lidar data averaging period during 5 September.

	1 st	2 nd	3 rd
Time [UTC]	09:10 -09:15 (600m a.g.l.)	10:31 (600m a.g.l.)	12:45 -12:50 (1800m a.g.l.)
	Averaging lidar data		
Time [UTC]	09:00-09:20	10:28 – 10:45	12:30 -13:00

In Table 20, we give the time of the flights over Bílý Kříž as well as the time period used for the lidar signal averaging. The low-altitude flight line (600 m agl) was below the PBL top height, while the high-altitude flight line (1800 m agl) was above PBL.

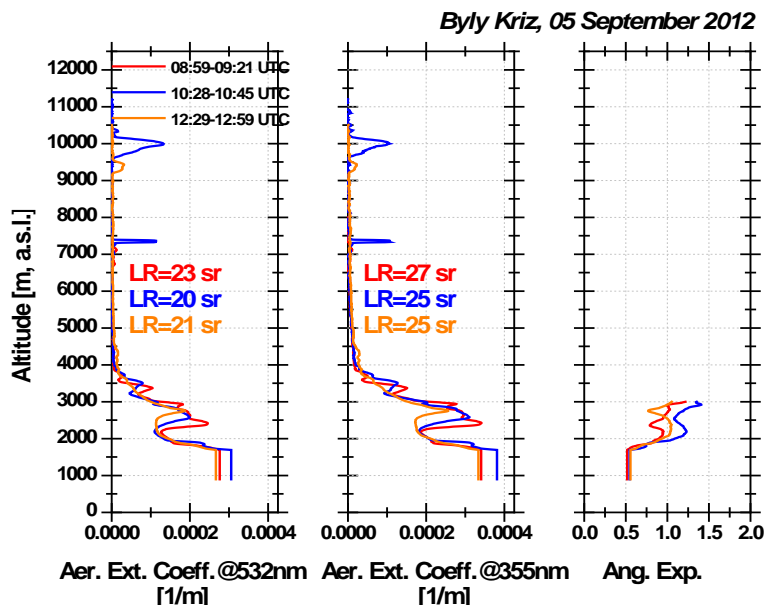


Figure 49: Vertical profiles of the aerosol extinction coefficient at 532 nm and 355 nm (in 1/m), retrieved by EMORAL during the three flight periods over Bílý Kříž on 5 September 2012.

In Figure 49, the aerosol extinction profiles at 532 nm and 355 nm are given. The three time periods of the overpasses over Bílý Kříž, are highlighted in different colours; red (08:59–09:21 UTC), blue (10:28–10:45 UTC), and orange (12:23–12:53 UTC). A thick and rather stable aerosol layer centred at 2.5 km could be observed. The AOD at 532 nm derived by EMORAL varied from 0.08 to 0.12, while the corresponding values at 355 nm varied from 0.12 to 0.18. Those values, in combination with the rather low AOD related Angstrom exponent (~ 1), are linked with coarse particles in the atmospheric column.

5.2.2.4 Bílý Kříž, 7 September 2012

On 7 September 2012, EMORAL operated from 07:26 to 14:42 UTC. During this time period, the laser sounding revealed a highly turbulent atmosphere with clouds moving rapidly in the low and mid troposphere (heights from 2 km to 8 km above sea level; Figure 50).

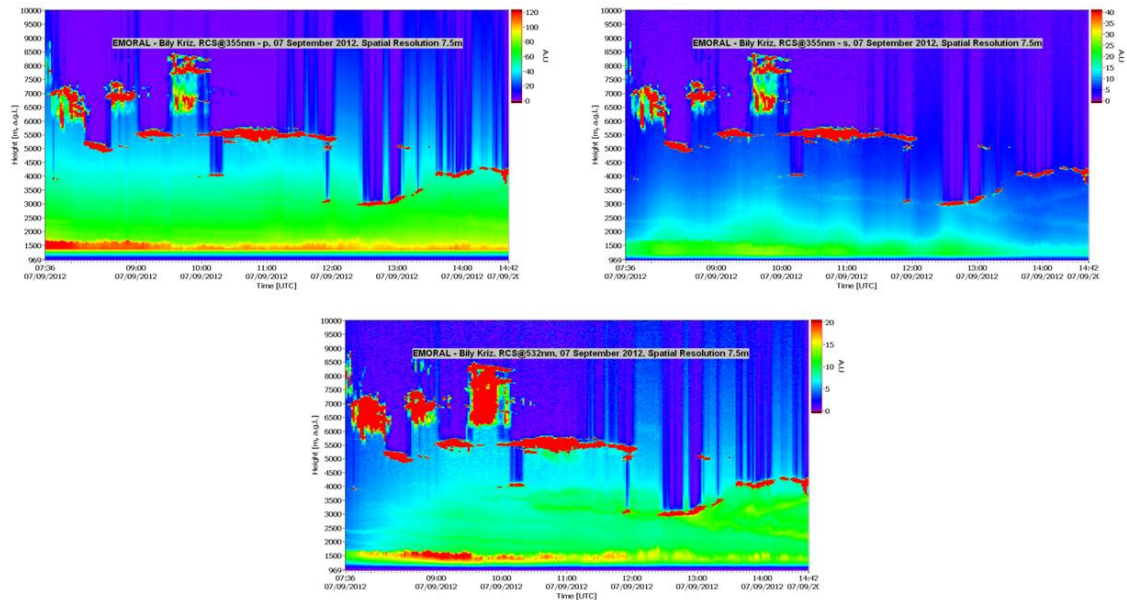


Figure 50: Range-Corrected lidar Signal (RCS, in Arbitrary Units) obtained by EMORAL at 355-p, 355-s, and 532 nm over Bílý Kříž (Czech Republic) on 7 September 2012.

5.2.2.5 Bílý Kříž, 9 September 2012

The atmospheric conditions were much better on 9 September 2012 with respect to luminosity, aerosol load, and turbidity. Figure 51 presents the range-corrected lidar signal obtained by EMORAL for the measurement period from 08:41 to 15:57 UTC. Cirrus clouds, with a centre of mass at 10.5 km, were detected during the early afternoon hours (until 14:00 UTC). From the logarithm of the RCS signal at 532 nm (Figure 52), the temporal evolution of the PBL top height was observed. It ranged from 1.5 km to 1.75 km above sea level.

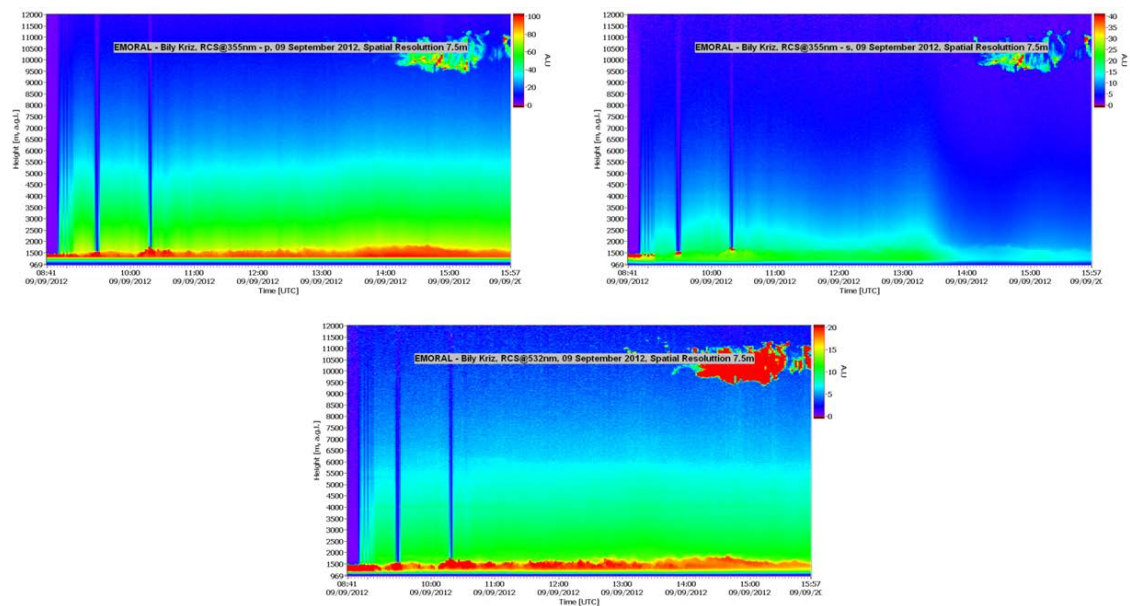


Figure 51: Range-Corrected lidar Signal (RCS, in Arbitrary Units) obtained by EMORAL at 355-p, 355-s, and 532 nm over Bílý Kříž (Czech Republic) on 9 September 2012.

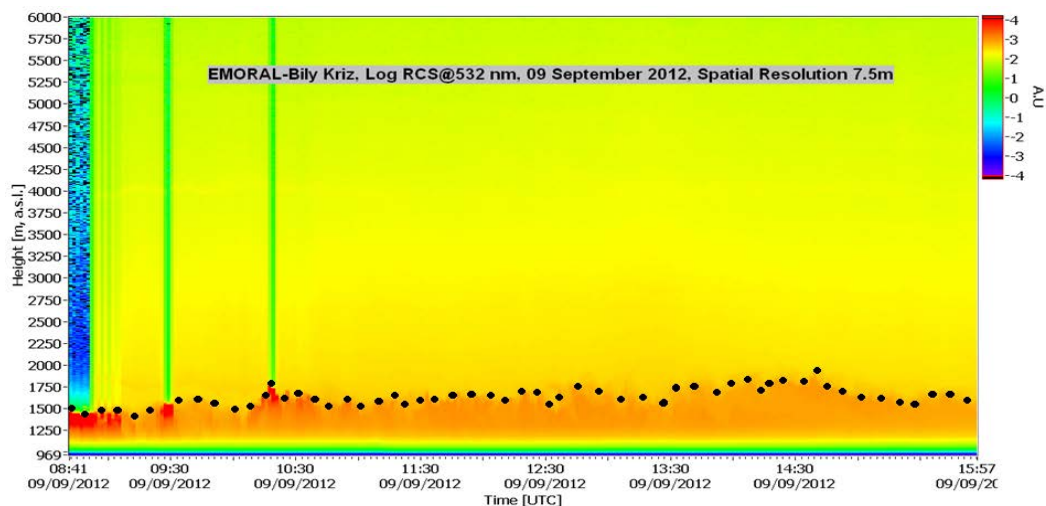


Figure 52: The logarithm of the Range-Corrected lidar Signal (LogRCS, in Arbitrary Units) obtained by EMORAL at 532 nm over Bílý Kříž (Czech Republic) on 9 September 2012.

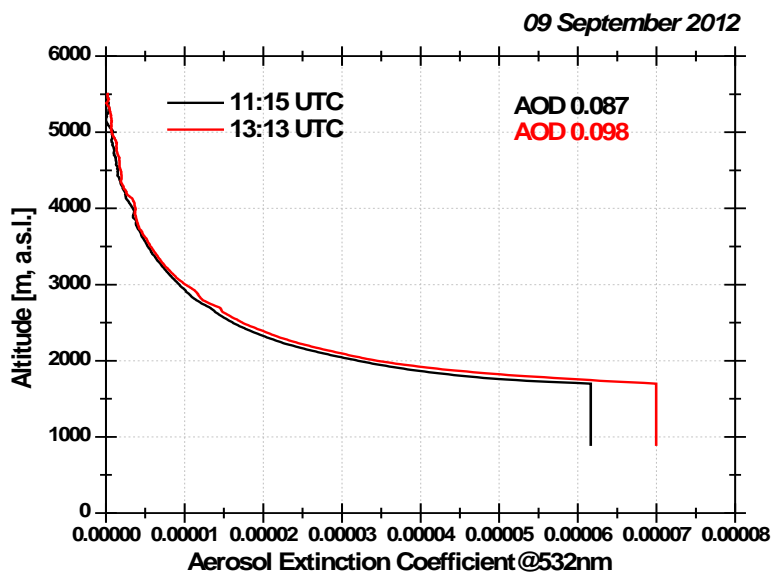


Figure 53: Vertical profiles of the aerosol extinction coefficient at 532 nm (in 1/m) retrieved by EMORAL during the two flight periods over Bílý Kříž on 9 September 2012. Black: profile at 11:15 UTC; red: profile at 13:13 UTC.

In Figure 53, the aerosol extinction profiles at 532 nm are given for the two time periods of flights over Bílý Kříž. Denoted in black is the profile at 11:15 UTC and in red, the profile at 13:13 UTC. The aerosol load seemed to be stable through time and insignificant because the AOD at 532 nm was found to be equal, 0.08 and 0.09, respectively.

The 10-day back trajectories, together with MODIS hot spot observations on 5 and 9 September 2012 are presented in Figure 54. The figure shows only three different times of the day (09:00, 12:00, and 14:00 UTC) on two selected days (5 and 9 September). The analysis, however, was performed with a one-hour temporal resolution for the whole campaign period in Bílý Kříž (3–9 September). Nevertheless, Figure 54 clearly shows that two different air mass patterns were affecting the experimental field.

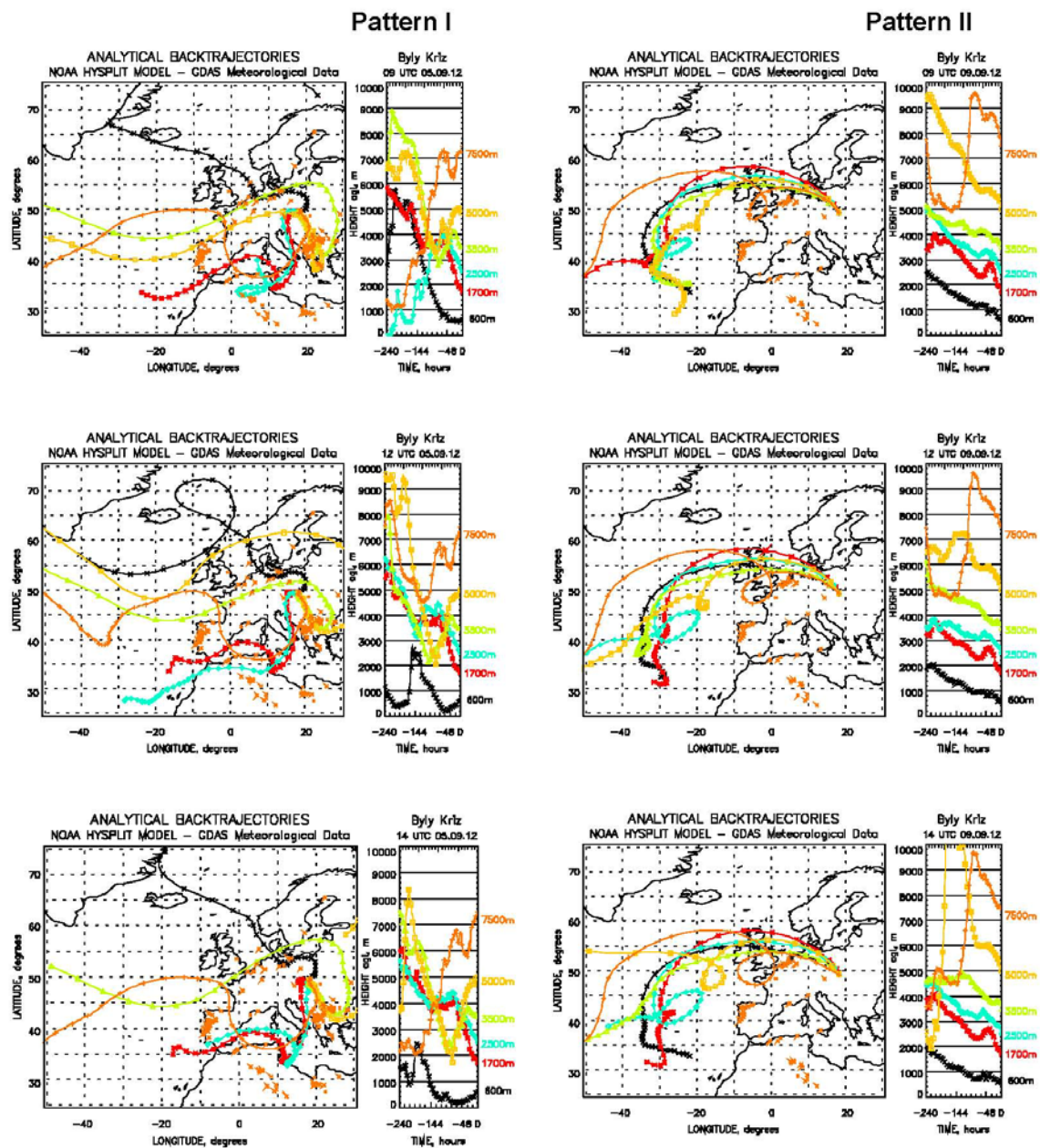


Figure 54: Air mass, 10-day back trajectories ending over Bílý Kříž at different heights, from 5 (left column – Pattern I) and 9 (right column – Pattern II) September 2012 at 09:00, 12:00, and 14:00 UTC.

During Pattern I, the air masses started from North Africa and South Eastern Iberian peninsula, affected mostly by coarse dust particles passing through the highly industrialised northern part of Italy (Po Valley) before reaching Bílý Kříž at heights below 3 km, advecting a mixture of different aerosol types there. The meteorological fields favoured this pattern for the time period between 3 and 5 September. For the period 6–9 September 2012, a different pattern (Pattern II) of air masses was dominant over Bílý Kříž. Clean marine aerosol (originating from the Atlantic Ocean) and less affected by pollution particles was transported long range over Bílý Kříž at heights below 3 km.

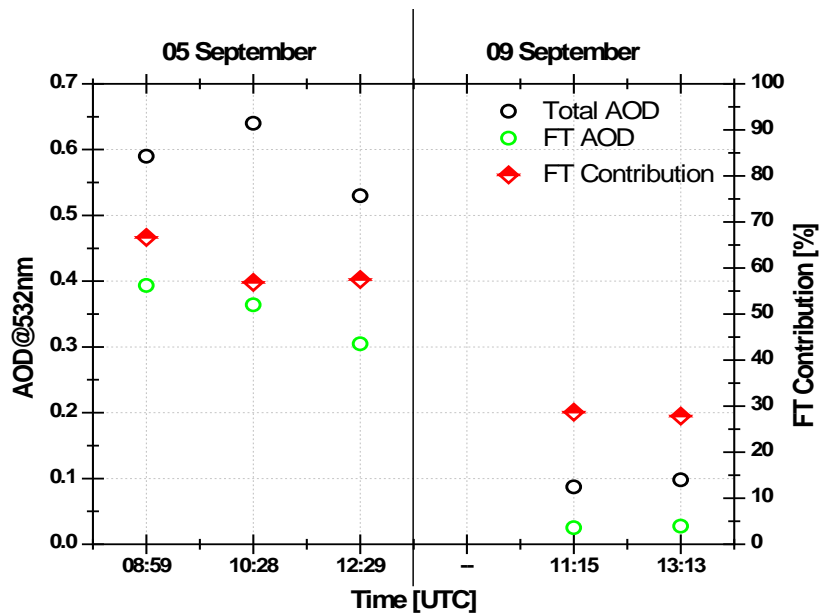


Figure 55: Columnar AOD, free tropospheric AOD values, and free tropospheric AOD contribution, at 532 nm for the measurements of two dates in Bílý Kříž that were obtained by EMORAL.

A synoptic situation of the AOD variability at 532 nm (as retrieved by EMORAL), for the two patterns affecting Bílý Kříž, is presented in Figure 55. During Pattern I (5 September), high aerosol load was observed over Bílý Kříž, with the AOD at 532 nm varying from 0.52 to 0.64, with mean free tropospheric contribution to the total AOD of 56%. During Pattern II (9 September), almost clear aerosol conditions prevailed, with the AOD at 532 nm of 0.09 and low free tropospheric contribution (~ 30%).

5.2.2.6 Supplementary Information

In the frame of LIVAS (Lidar Climatology of Vertical Aerosol Structure for Space-based Lidar Simulation Studies) (ESTEC Contract No. 4000104106/11/NL/FF/fk), a four-year aerosol statistical analysis from CALIPSO satellite with a global covering of $1^\circ \times 1^\circ$ spatial resolution is performed (Figure 56).

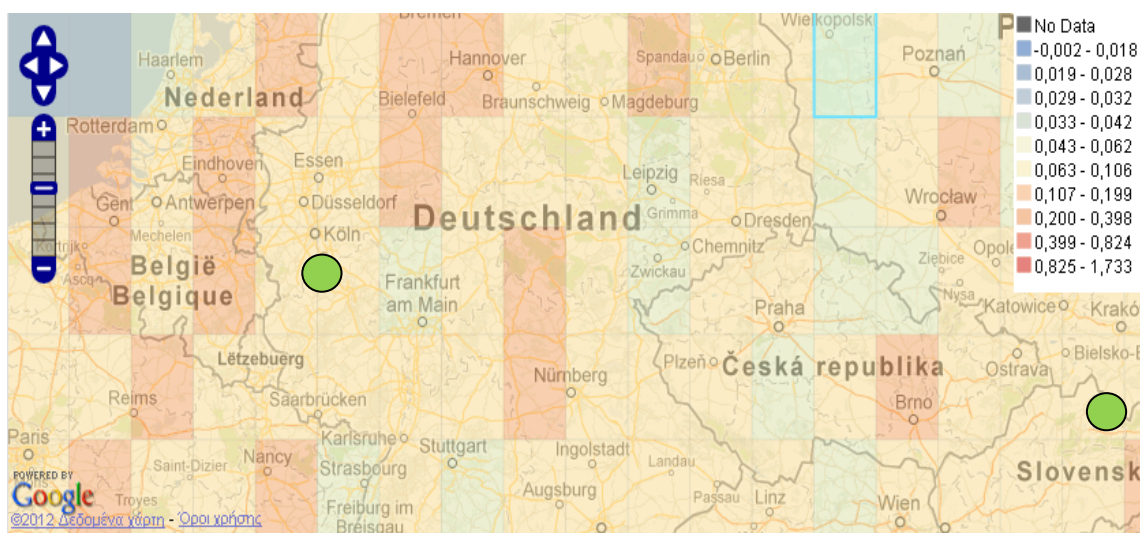


Figure 56: Mean Aerosol Optical Depth at 532 nm based on four years of CALIPSO climatology in $1^\circ \times 1^\circ$ cell bin. Areas of our interest are marked with green circles.

We used this analysis to have a better knowledge of the mean aerosol load and prevailing aerosol type in the regions where the HYFLEX campaign took place. Mean AOD at 532 nm of the study sites ranged between 0.107–0.199. Those values agree with our observations.

In addition, for both experimental fields, CALIPSO's algorithm characterised the aerosol type as pure smoke (S) for the majority of aerosol observations (~ 40%); 30% of the aerosol observations for the Czech site and 22% of aerosol observations for the corresponding German site were characterised as polluted dust (PD), a mixture of dust particles and smoke (Figure 57).

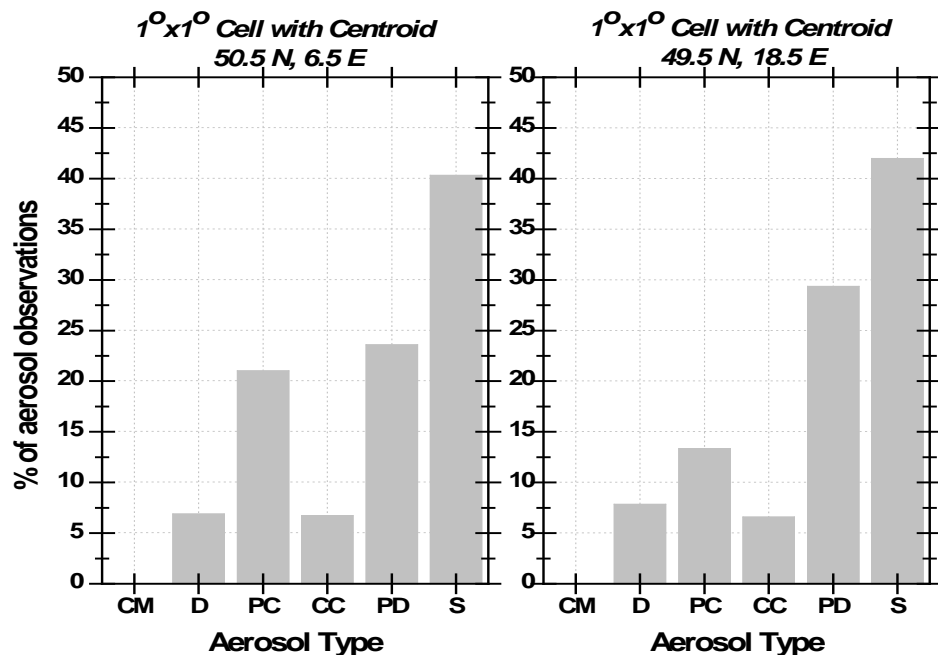


Figure 57: CALIPSO's aerosol type characterisation vs the % of aerosol observations for Selhausen (*left*) and Bílý Kříž (*right*). LIVAS: Global statistical climatology from CALIPSO [ESA project]; CM=Clean Marine, D=Dust, PC=Polluted Continental, PD=Polluted Dust, S=Smoke.

In order to have a better idea of the usage of the lidar system within the HYFLEX project, we proceeded with a simulated scenario where atmospheric correction for HyPlant could be done with the usage of a lidar or a simple radiative transfer model. We present our procedure in Figure 58.

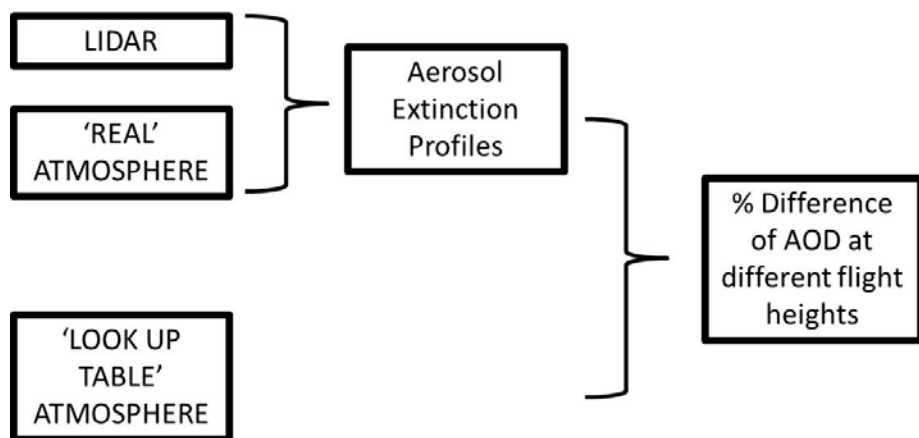


Figure 58: Procedure of a simulated scenario for atmospheric correction.

Initially, we considered a lidar system operating at 532 nm with an overall efficiency of 34%. This system is equipped with a receiving telescope having a focal length of 1000 mm and diameter of 300 mm. The laser beam (nominal) divergence and diameter are of the order of 0.6 mrad (full angle) after beam expansion (x3) and 10 mm, respectively. The energy of the laser beam is 125 mJ/pulse. The system is also equipped with a field stop diaphragm of 1.5 mm diameter. Those characteristics lead to a system that has a full overlap distance above 1 km (Figure 59).

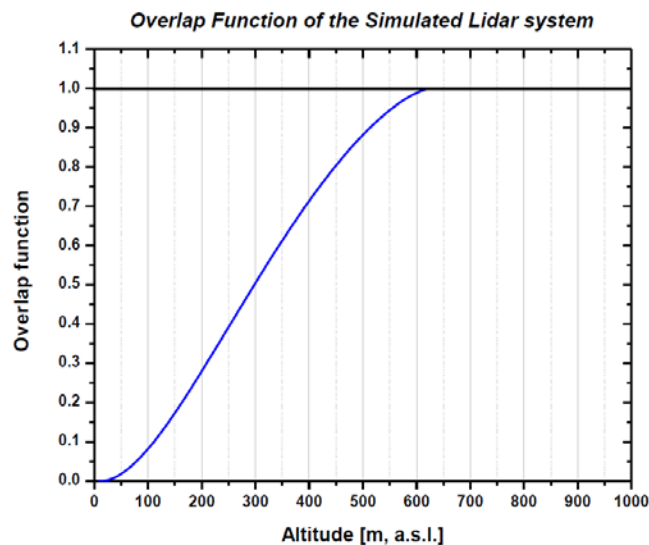


Figure 59: The overlap function of the simulated ground based lidar system.

A standard atmospheric model (U.S. Standard Atmosphere, 1976) fitted to temperature and pressure values (20°C, 1013hPa) at the ground level simulated the atmospheric density and the Rayleigh scattering coefficient. Up to 1.5 km, a typical planetary boundary layer (PBL) aerosol with mean backscatter coefficient of $1.48 \times 10^{-6} \text{ m}^{-1} \text{ sr}^{-1}$ and LR=75 sr was considered for our simulation. A typical aerosol layer having LR=40 sr and an aerosol backscatter coefficient of $2.82 \times 10^{-6} \text{ m}^{-1} \text{ sr}^{-1}$ was considered between 3–4 km. Furthermore, a Saharan mineral dust layer having LR=40 sr, and an aerosol backscatter coefficient of $3.18 \times 10^{-6} \text{ m}^{-1} \text{ sr}^{-1}$ was considered between 4.5–5 km height. Finally, a cirrus cloud (with $\text{baer} = 8.10 \times 10^{-6} \text{ m}^{-1} \text{ sr}^{-1}$ and LR=30 sr) is also used as input in our simulation in the 9–10 km altitude region. In all cases, a vertical resolution of 7.5 m is considered for the received lidar signals.

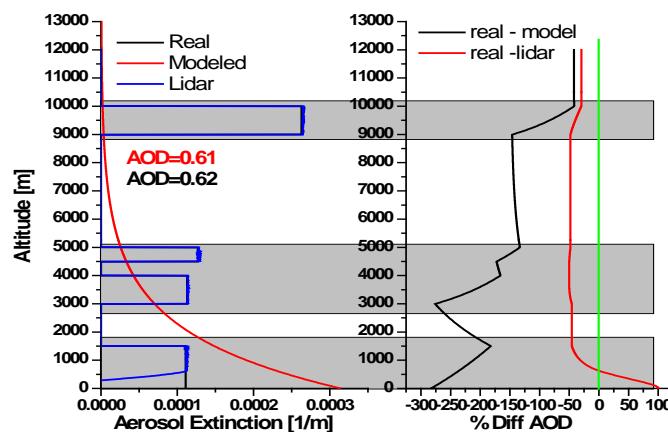



Figure 60: Altitude vs aerosol extinction is on the *left*: simulated atmosphere (black line), lidar retrieval (blue line), and typical exponential extinction profile from a radiative transfer model (red line). Relative difference in the AOD (%) is on the *right*.

The aforementioned conditions produce an aerosol optical depth of 0.62 at 532 nm.

Figure 60 demonstrates the aerosol extinction profile (blue line) as it was retrieved by the simulated lidar system for the simulated atmosphere (black line). It can be clearly seen that all aerosol and cloud layers are well revealed by the lidar system. A typical radiative transfer model

 JÜLICH FORSCHUNGSZENTRUM	Doc.: HYFLEX – Final Report		
	Date: 16-04-2014	Issue: 8	Revision: 0
	Ref.: ESA Contract No. 4000107143/12/NL/FF/If		Page: 63 / 113

describes the atmosphere, usually with an exponential extinction profile (red line). If the sensor flies at higher altitudes (higher than 10 000 m, above all aerosol and cloud layers), the atmospheric correction will most likely be correct because the choice of the aerosol type from the radiative transfer model produced AOD values similar to the observed ones (Figure 60, *right*). Problematic situations could occur if the sensor flies at heights where the aerosol contribution to the total columnar AOD is insignificant. In those lower parts of the atmosphere, the relative difference between the true AOD values and the AOD used by the radiative transfer model could dramatically increase thereby leading to wrong atmospheric corrections and results.

5.3 Top of canopy fluorescence

5.3.1 Agriculture

5.3.1.1 Selhausen, 23 and 27 August 2012

On 23 and 27 August, high-resolution top-of-canopy radiance measurements were collected in a sugar beet field at the Selhausen site (50° 51' 49.993" N; 6° 27' 3.36" E) using the manual portable spectrometric system. Spectrometer fibres were mounted on a tripod placed in the sugar beet field (Figure 25) and the average canopy plane was observed from nadir at a distance of 140 cm from the top of the canopy (average height of the canopy 75 cm). The manual rotation of a mast-mounted horizontally on the tripod allowed observation of the calibrated white reference panel (Labsphere Inc., USA) and three different circular areas of the canopy (diameter 65 cm). Tripod, white reference panel, and operators were positioned about 2 m north of the areas observed. For every acquisition, eight and three scans (for spectrometer 1 and 2, respectively) were averaged and stored as a single file.

The NDVI and F_{760} diurnal courses collected over the sugar beet field during the days of the HyPlant overpasses are shown in Figure 61. The sampling area was characterised by a LAI of $7.4 \text{ m}^2 \text{ m}^{-2}$ and a leaf chlorophyll concentration of $78 \mu\text{g cm}^{-2}$.

The sky was clear on 23 August, as evidenced by the diurnal shape of the incident radiance (Lin) at 747.5 nm. On August 27, the sky conditions were stable, though not optimal, only during the morning. The NDVI course during the day was quite stable, with a slightly decreasing trend from early morning to midday/mid-afternoon, with values higher than 0.9, in agreement with a LAI value of $7.4 \text{ m}^2 \text{ m}^{-2}$ of the area sampled by the spectrometers.

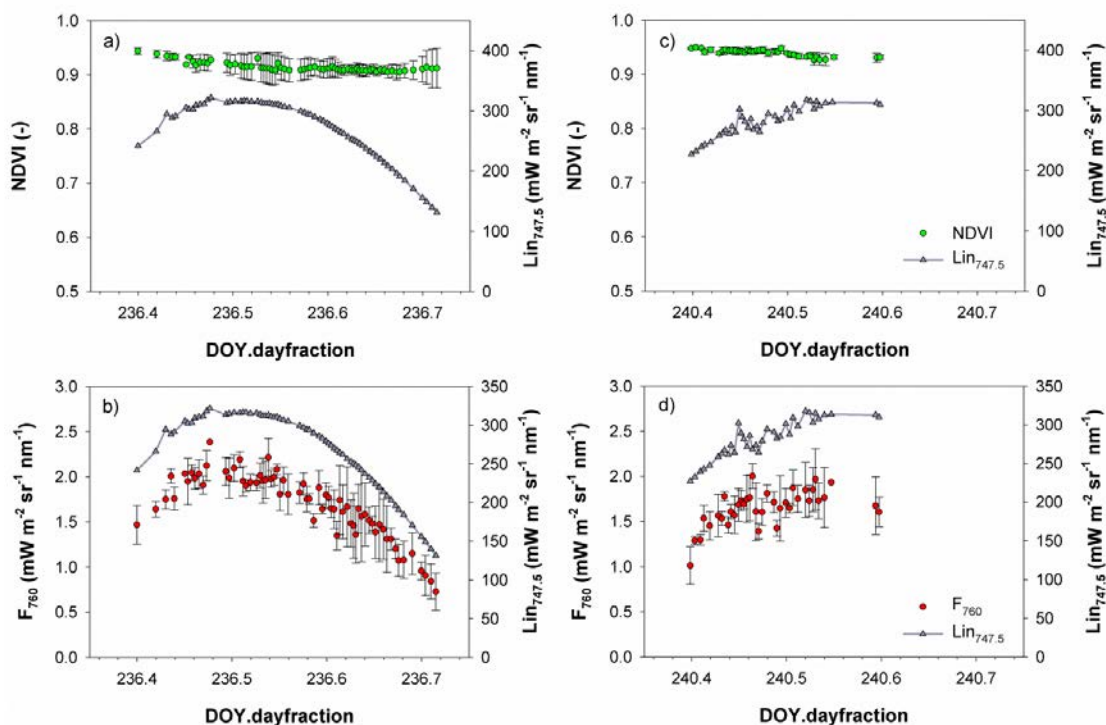


Figure 61: NDVI and F_{760} ($\text{mW m}^{-2} \text{ sr}^{-1} \text{ nm}^{-1}$) diurnal courses measured at the Selhausen site on sugar beet on 23 August (a, b) and 27th (c, d). $\text{Lin}_{747.5}$ is the incident radiance ($\text{mW m}^{-2} \text{ sr}^{-1} \text{ nm}^{-1}$) at 747.5 nm. DOY is day of the year.

F_{760} in both days clearly mirrored the course of the incident radiance, with the highest values around midday (F_{760} slightly higher than $2 \text{ mW/m}^2/\text{sr}^1/\text{s}^1$). At the diurnal time scale, in fact, the variation in F_{760} is modulated by photosynthetic activity that is in turn mainly driven by the incident PPFD. Both NDVI and F_{760} values are similar in the two days of measurement. Compared to NDVI, F_{760} is more affected by the unstable sky conditions on 27 August.

On 27 August, the MRI system was placed in a grassland field ($50^\circ 52' 9.538'' \text{ N } 6^\circ 27' 7.153'' \text{ E}$) and a second validation point was measured. Spectrometer fibres were mounted on a tripod (Figure 24), allowing the measurement of the grassland (average height of 42 cm) from nadir at a distance of 128 cm. A circular area of the canopy with 60 cm diameter was observed by the spectrometers. For every acquisition, five and three scans (for spectrometer 1 and 2, respectively) were averaged and stored as a single file.

With a leaf chlorophyll concentration of 1.4 mg g^{-1} fresh weight, the grassland was senescing at the time of the HyPlant survey. The senescence experienced by the grassland also manifested in the canopy spectral properties (Figure 62). The grassland was, in fact, characterised by an NDVI value of 0.6 at midday, and F_{760} values were stable during the day and lower than $0.5 \text{ mW/m}^2/\text{sr}^1/\text{nm}^1$, indicating a really low photosynthetic activity typical of the senescence phase.

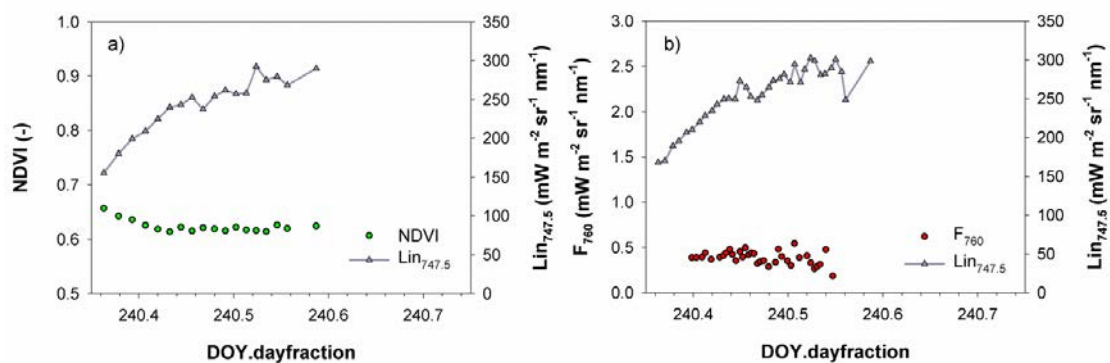


Figure 62: NDVI (a) and F_{760} ($\text{mW m}^{-2} \text{ sr}^{-1} \text{ nm}^{-1}$) (b) diurnal courses measured at the Selhausen site on the grassland on 27 August. $\text{Lin}_{747.5}$ is the incident radiance ($\text{mW m}^{-2} \text{ sr}^{-1} \text{ nm}^{-1}$) at 747.5 nm. DOY is day of the year.

5.3.1.2 Klein-Altendorf, 23 August 2012

Spectrometer fibres were mounted on a stair placed in the sugar beet field (Figure 24) ($50^\circ 36' 54.498'' \text{ N } 6^\circ 59' 31.009'' \text{ E}$). The average canopy height was 46 cm and was observed from nadir at a distance of 224 cm. A circular area of the canopy with 105 cm diameter was therefore observed by the spectrometers.

For every acquisition, five and three scans (for spectrometer 1 and 2, respectively) were averaged and stored as a single file.

Figure 63 shows the diurnal course of NDVI and F_{760} the day of the HyPlant overpass. Sky conditions were slightly unstable during the morning, as highlighted by the variability of the incident irradiance (as a reference, the incident radiance at 747.5 nm is reported in Figure 62). Sky conditions improved from 14:00 local time onward. The NDVI course during the day is quite stable, with a slightly decreasing trend from early morning to midday/mid-afternoon. F_{760} shows a course that mirrors the one of the incident radiance, with the highest values around midday (F_{760} equal to $2.15 \text{ mW m}^{-2} \text{ sr}^{-1} \text{ s}^{-1}$). NDVI was little affected by the unstable sky conditions experienced in the morning, while the effect of the variable illumination conditions was evident on the F_{760} course.

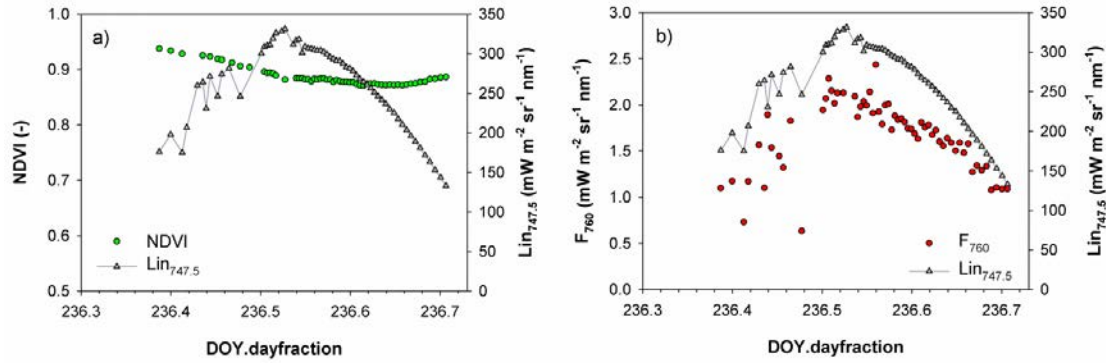


Figure 63: NDVI (a) and F_{760} ($\text{mW m}^{-2} \text{sr}^{-1} \text{nm}^{-1}$) (b) diurnal courses measured at the Klein-Altdorf site on the sugar beet field on 23 August. $\text{Lin}_{747.5}$ is the incident radiance ($\text{mW m}^{-2} \text{sr}^{-1} \text{nm}^{-1}$) at 747.5 nm. DOY is day of the year.

5.3.2 Forest

5.3.2.1 Atmospheric correction of the top of canopy measurements collected over the spruce forest

Recent studies (Daumard et al. 2010) suggested that the distance (i.e., path-length) between the instrument and the top of the canopy affects the F_{760} values retrieved using the oxygen absorption bands. However, a proper quantification of this effect is still missing.

In this context, a preliminary analysis of high-resolution spectral measurements around the $\text{O}_2\text{-A}$ band collected during the Bílý Kříž field campaign is carried out with the aim to:

- provide a preliminary evaluation of the atmospheric impact on F_{760} field spectroscopy measurements from high towers
- develop a F_{760} retrieval method capable of accounting for the atmospheric effect on F_{760} field spectroscopy measurements.

High-resolution spectra collected using the s-Fluor installed at 21 m above the spruce canopy on the eddy covariance tower are used to test the atmospheric correction approach.

The methodology used combines ground measurements with atmospheric radiative transfer (RT) simulations using Modtran5.2.1 at full resolution (0.1 cm^{-1}).

Downwelling (L_{wr}) and upwelling (L_{s}) radiances as measured by the field spectrometers over the forest were modelled according to the canopy-atmosphere RT interaction recently proposed by W. Verhoef to account for the vegetation fluorescence emission. Top-of-canopy reflectance and fluorescence are simulated using the FluorMod3.0 model (considering Lambertian conditions $r_{\text{so}}=r_{\text{do}}=r_{\text{sd}}=r_{\text{dd}}$) and propagated in the atmosphere using Modtran5.2.1.

Downwelling Radiance

$$L_{\text{wr}}^{\text{mod}} = \rho_{\text{so}} \frac{E_s^o \cos \theta_s}{\pi} + \left[\frac{\tau_{\text{ss}} r_{\text{so}} E_s^o \cos \theta_s / \pi + F_s}{(\tau_{\text{sd}} + \tau_{\text{ss}} r_{\text{sd}} \rho_{\text{dd}}) E_s^o \cos \theta_s / \pi + F_d \rho_{\text{dd}} r_{\text{do}}} \right] \tau_{\text{oo}} + \frac{(\tau_{\text{sd}} r_{\text{dd}} + \tau_{\text{ss}} r_{\text{sd}}) E_s^o \cos \theta_s / \pi + F_d \tau_{\text{do}}}{1 - r_{\text{dd}} \rho_{\text{dd}}} \tau_{\text{do}}$$

$r_{\text{so}} = r_{\text{do}} = 1;$ $r_{\text{sd}} = r_{\text{dd}} = R_{\text{canopy}}$ simulated with FluorMod

(Eq.1)

Canopy Radiance

$$L_s^{\text{mod}} = \rho_{so} \frac{E_s^o \cos \theta_s}{\pi} + \left[\frac{\tau_{ss} r_{so} E_s^o \cos \theta_s / \pi + F_s}{1 - r_{dd} \rho_{dd}} \right] \tau_{oo} + \frac{(\tau_{sd} \overline{r_{dd}} + \tau_{ss} \overline{r_{sd}}) E_s^o \cos \theta_s / \pi + \overline{F_d} \rho_{dd} r_{do}}{1 - r_{dd} \rho_{dd}} \tau_{do}$$

$r_{so} = r_{do} = r_{sd} = r_{dd} = R_{\text{canopy}}$ simulated with FluorMod

(Eq.2)

The mean value of the product of two or more atmospheric functions (τ_{ss}) over a spectral interval will not be equal to the product of the mean values of the individual quantities but greater due to the strong correlation within the interval. The novel approach proposed by W. Verhoef to avoid the so-called curve of growth effect requires reformulating the canopy-atmosphere RT interaction according to the equation reported below. Products of atmospheric functions are done before the spectral convolution to the instrument spectral response functions.

$$L^{\text{mod}} = T_1 \left[T_2 + T_8 r_{so} + \frac{T_9 + T_{14} \overline{r_{sd}}}{1 - r_{dd} T_3} r_{do} + \frac{T_{10} \overline{r_{sd}} + T_{11} \overline{r_{dd}}}{1 - r_{dd} T_3} \right] + F_s T_6 + \left[\frac{\overline{F_d} (T_7 + T_{13} r_{do})}{1 - r_{dd} T_3} \right]$$

(Eq.3)

The fourteen atmospheric functions calculated are reported in the table and depicted in Figure 64.

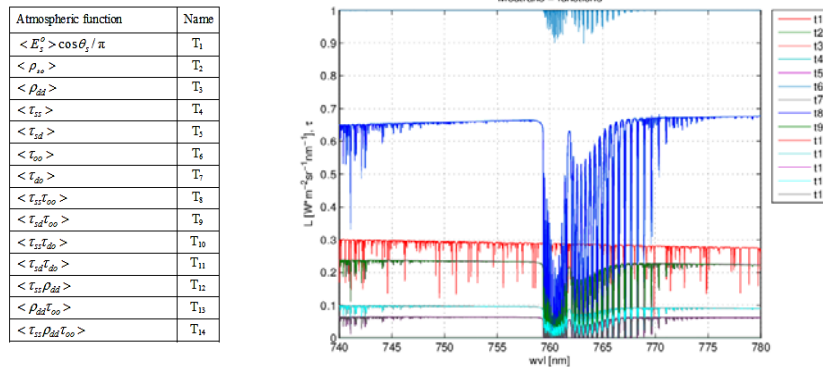


Figure 64: Atmospheric functions used in the canopy-atmosphere RT model.

Three different F_{760} retrieval schemes are tested to assess the impact of the atmosphere in the optical path between the canopy and the sensor:

1. no atmospheric correction (Method-1)
2. basic atmospheric correction considering direct/diffuse transmittance but neglecting the curve-of-growth effect (Method-2)
3. full atmospheric effect correction based on the RT model presented above (Method-3).

Fluorescence values at 760 nm are retrieved using the *Spectral Fitting Methods* (SFM) in the 750–770 nm spectral window modelling the reflectance using a polynomial function of the 3rd order and fluorescence using a Lorentzian line shape in all three of the methods.

The atmospheric impact in the canopy-sensor path length is assessed using RT simulations considering a typical vegetation reflectance/fluorescence spectrum modelled with FluorMod3.0.

The top of canopy radiance propagated through the atmosphere up to different heights above the canopy (5, 10, 15, 20, 50, and 100m), convolved to the instrument spectral response functions and added with a random Gaussian noise typical of the Ocean Optics spectrometers (SNR=300). Figure 65 depicts the scheme (forward and inverse RT calculation) used for the vertical profile simulation test.

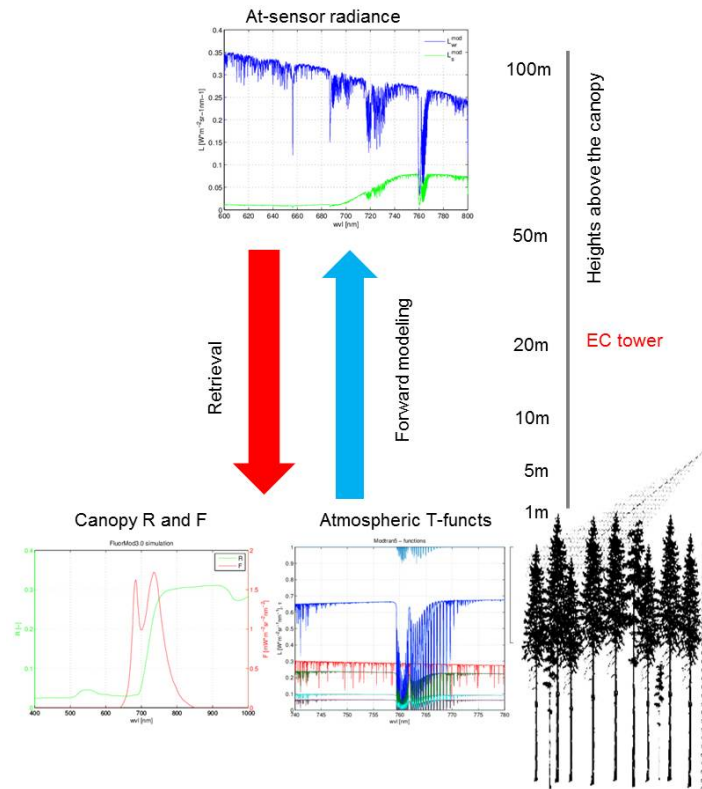


Figure 65: Simulation of the vertical profile: canopy reflectance/fluorescence (FluorMod3.0) are coupled with atmospheric functions calculated with Modtran5.2.1 to propagate the radiance through the atmosphere at different heights above the canopy from 1 to 100 m. Fs and reflectance are retrieved using the three different schemes proposed.

Three F_{760} retrieval methods are tested at this stage assuming a perfect knowledge of the atmospheric status (i.e., Aerosol Optical Thickness AOD, Surface Pressure SPR). Results are evaluated quantifying the difference between F_{760} and R at top-of-canopy level input (before the atmosphere propagation) with the respective values retrieved at the different heights above the canopy Figure 66. Method-1 does not account for the oxygen absorption effect between the top of canopy and the sensor. The resulting F_{760} is underestimated starting from a distance of 20 m (relative error of 25%). On the contrary, the second method overestimates the fluorescence that was probably caused by the curve-of-growth effect of the transmittance. The inversion of the full RT models (Method-3) provides the best results; values of F_{760} at the different heights are constant and close to the input value at the top-of-canopy level ($1.0 \text{ mW/m}^2/\text{sr}^1/\text{nm}^1$ and 0.287 for F_{760} and R respectively).

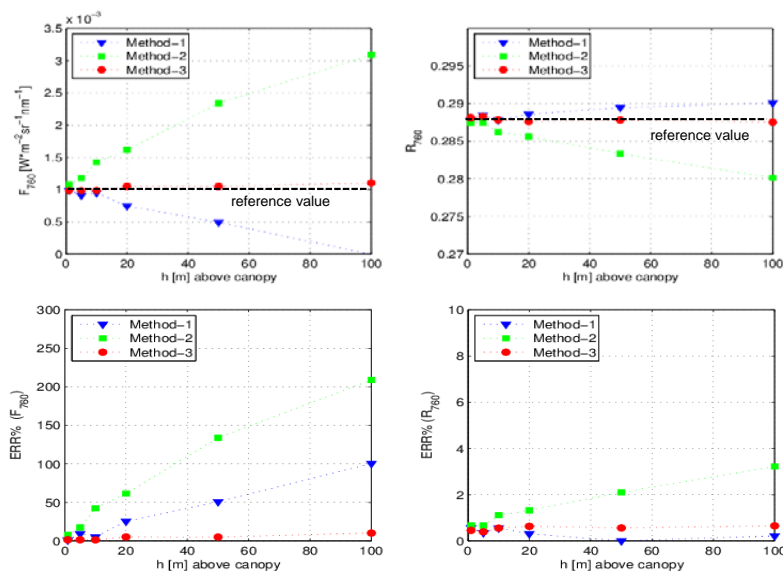


Figure 66: Impact of the different top-of-canopy spectrometer distances (h [m] above the canopy) on the F_{760} retrieval using the three different retrieval schemes. Blue triangles represent the retrieval without atmospheric correction (Method-1); green squares (Method-2) employ a basic atmospheric correction; red dots (Method-3) provide a full modelling of atmospheric effects. On the *left*, the absolute values of F_{760} (*top*) and relative error (*bottom*) are shown; on the *right*, the reflectance is depicted. Dashed lines represent the top of canopy values ($1.0 \text{ mW m}^{-2} \text{ sr}^{-1} \text{ nm}^{-1}$ and 0.287 for F_{760} and R respectively) before the propagation of the radiance through the atmosphere.

Atmospheric impact in the canopy-sensor path length changes with the actual atmospheric status (i.e., scattering and absorption). For this reason, application of Method-3 to correct diurnal course field spectroscopy measurements collected at a significant height above the canopy (from the EC tower) requires an accurate estimation of atmospheric AOD and SPR.

A LUT inversion technique is tested to retrieve atmospheric properties exploiting downward radiance measurements collected using field spectroscopy. A LUT of top of the canopy is generated considering the summer mid-latitude profile (the most commonly used atmospheric profile for Europe during summer), four different AOD levels (0.075, 0.13, 0.18, and 0.3) and three SPR levels (1000, 930, and 880 mb), for a total of twelve RT simulations. To retrieve atmospheric parameters, we compare the RT modelled and ground measurements with an iterative optimisation. AOD and SPR retrieved from high-resolution optical data are compared with those provided from the sun photometer (AOD) and the micrometeorological station (SPR) (Figure 67).

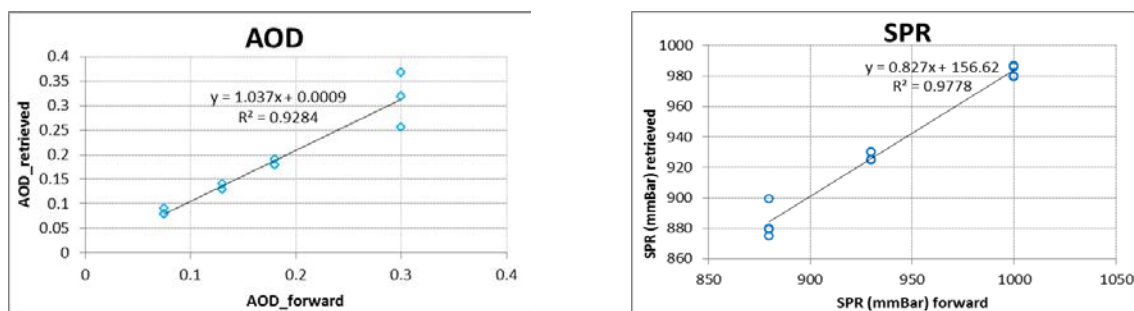


Figure 67: Comparison between input and retrieved values of Aerosol Optical Density (AOD) and Surface Pressure (SPR).

Results show agreement between the AOD and SPR values used as input in the RT model and the values retrieved with the LUT based iterative inversion. The good results are promising and the same atmospheric inversion technique is used to estimate atmospheric properties and the retrieve fluorescence with Method-3. Figure 68 shows the results of the application of Method-3 for the retrieval of F_{760} considering the atmospheric influence. Using the new retrieval method, F_{760} values increase in both the analysed cases (S-FLUOR Box and measurements from the hydraulic platform) due to the correction of the oxygen absorption. We collected field spectroscopy measurements on the same plant species from the eddy covariance tower and the hydraulic platform. However, the field of view of the instruments did not overlap on the same area, which introduced additional uncertainty in the quantitative comparison of the results. F_{760} values calculated with the new, proposed Method-3 are higher, suggesting that the atmosphere also affects field spectroscopy measurements collected tens of metres above the top of the canopy. The impact of the atmospheric correction is lower, at least negligible, on the reflectance estimations.

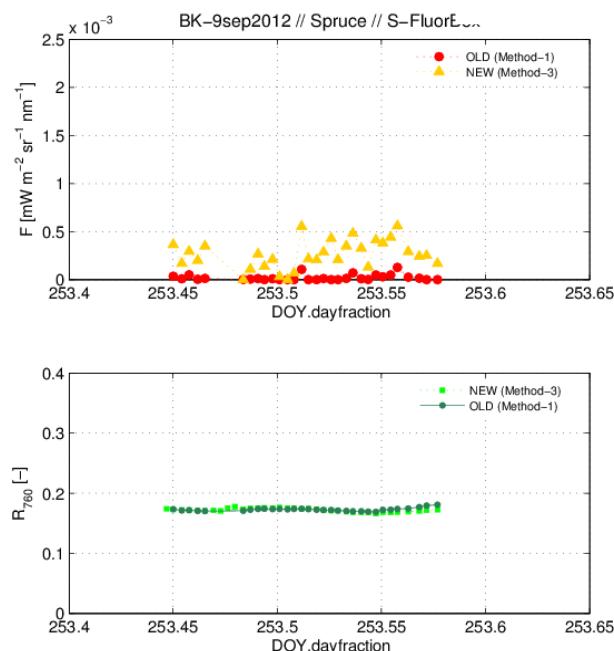


Figure 68: Comparison of F_{760} (top) and R (bottom) retrieved from field spectroscopy measurements collected at Bílý Kříž on 9 September over the spruce forest from the eddy covariance tower. Dark markers refer to the retrieval method without considering atmospheric influence (Method-1); light markers are calculated using the full RT retrieval model scheme proposed (Method-3).

In summary, the atmospheric impact on F_{760} retrieval from field spectroscopy measurements collected at Bílý Kříž was assessed by exploiting RT simulations and real measurements collected during the field campaign. RT simulations considering a scenario of field spectrometers placed at an increasing height above the top of the canopy show that correction of the atmospheric impact is needed starting from 20 m of height. The estimated relative error is around the 25% of the F_{760} signal detected. To overcome this effect, a new retrieval method based on RT models (Method-3) is proposed to account for the atmospheric effect on F_{760} retrieval from field spectroscopy measurements. The new algorithm was tested on real field data collected in Bílý Kříž.

5.3.2.2 Spruce forest, 3–9 September 2012

The forest experimental site of Bílý Kříž consists in a 35-year-old regular plantation of Norway spruce (*Picea abies* (L.) Karst) growing on a moderate slope (13°) with S-SE orientation. Two different areas have been selected for high-resolution top-of-canopy radiance measurements in the spruce forest (Figure 69).

The s-Fluor box has been installed at the top of the eddy covariance tower (38 m). The optical fibres were held at the end of a 3-m-long arm pointing south. The canopy plane was observed from 21 m with an angle of 7°, corresponding to an elliptical field of view of about 9.38 and 9.46 m axes.

The manual system was used from a mobile hydraulic platform positioned 4.4 m above the canopy plane. The optical fibres were held at the end of a 2.5 m long arm allowing the observation of an area of 1.9 m diameter from nadir.

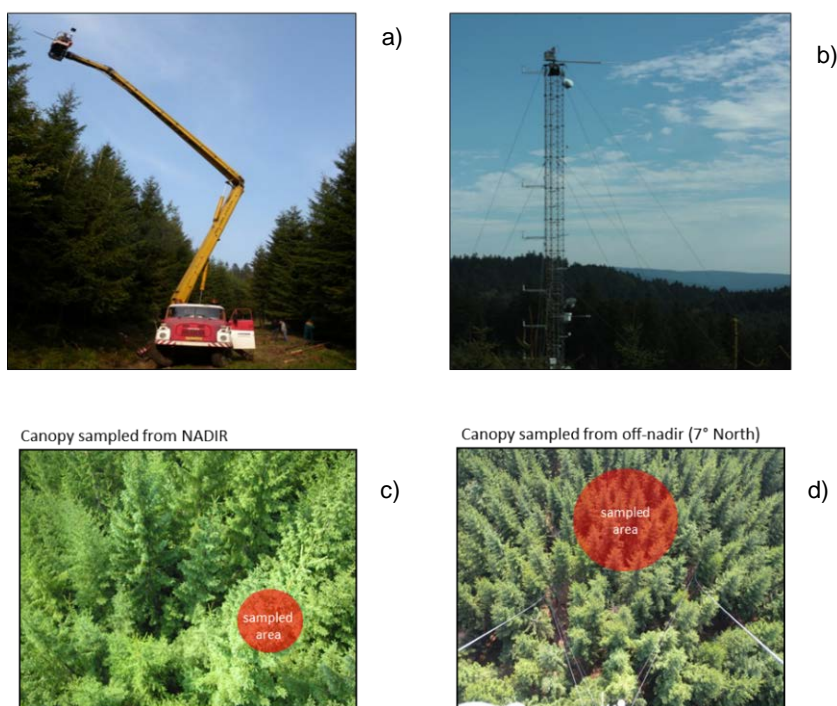


Figure 69: Field set-up used at the Bílý Kříž study site on the spruce forest (3–9 September): manual system operated at 4.4 m above the canopy using the hydraulic platform (a), s-Fluor Box installed on the top of the eddy covariance tower at an average height of 21m above the canopy (b). Pictures in the lower part show the area sampled by the manual system (c) and by the s-Fluor box (d).

The spruce Leaf Area Index (LAI) value close to the eddy covariance tower was $6.4 \text{ m}^2 \text{ m}^{-2}$, while it reached a value of $8 \text{ m}^2 \text{ m}^{-2}$ in the area measured from the mobile platform. Also, needle chlorophyll concentration was lower in the trees sampled from the eddy covariance tower (chlorophyll a+b = 0.54 mg/g fresh weight), whereas it reached values of 1.25 mg/g fresh weight in the trees sampled from the mobile platform. These differences in biochemical and biophysical canopy properties affected the canopy spectral properties. The average reflectances in the visible and near infrared regions measured at midday on the spruce forest from the eddy covariance tower and from the mobile platform are shown in Figure 10. The average reflectance measured from the eddy covariance tower is generally lower than the one measured from the mobile platform in both the visible and near infrared regions. This can be explained by the lower LAI of the plot close to the tower but probably also by the different proportions of sunlit and

shaded canopy components measured from the tower and from the mobile platform. We expect a greater portion of shadowed components in the area observed from the tower due to the wider sampling area and the off-nadir view. Lower reflectance values of the shaded spruce crowns have been also observed by Malenovsky et al. (2013) using airborne AISA Eagle (Spectral Imaging, Specim Ltd., Finland) data collected on the same study area in September 2004. The mean reflectance of shaded crown components can be up to half intensity of the sunlit crown signal.

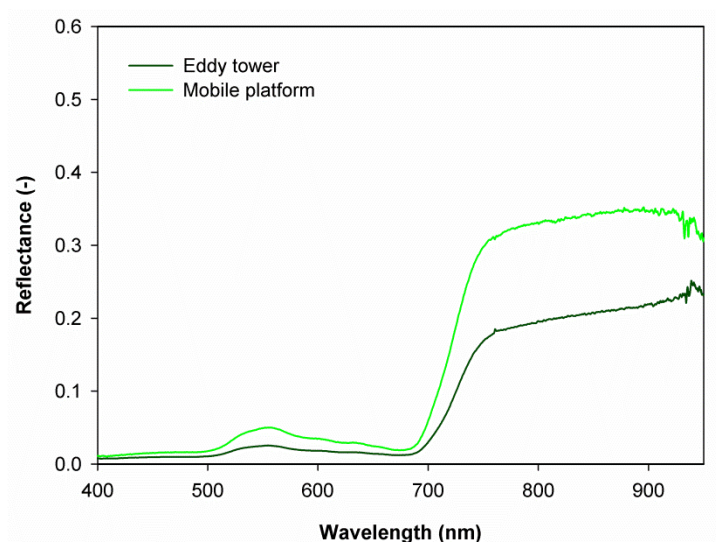


Figure 70: Average reflectances in the visible and near infrared regions measured at midday on the spruce forest from the eddy covariance tower (dark green line) and from the mobile platform (light green line).

The time courses of the normalised difference vegetation index (NDVI) and sun-induced fluorescence at 760 nm (F_{760}) measured from the mobile platform are reported in Figure 71 and Figure 72, respectively.

The NDVI course was quite stable on both days with a value close to 0.9 (Figure 71). The course of F_{760} during the day is different on 5 and 9 September (Figure 72). This different shape can probably be explained by the different sky conditions occurred in the two days, evident in the diurnal course of the incident radiance ($Lin_{747.5}$ in the graph). Besides the diurnal course, F_{760} also showed different absolute values in the two days, with a value at midday of $0.3 \text{ mW/m}^2/\text{sr}^1/\text{nm}^1$ on 5 September and $0.7 \text{ mW/m}^2/\text{sr}^1/\text{nm}^1$ on 9 September.

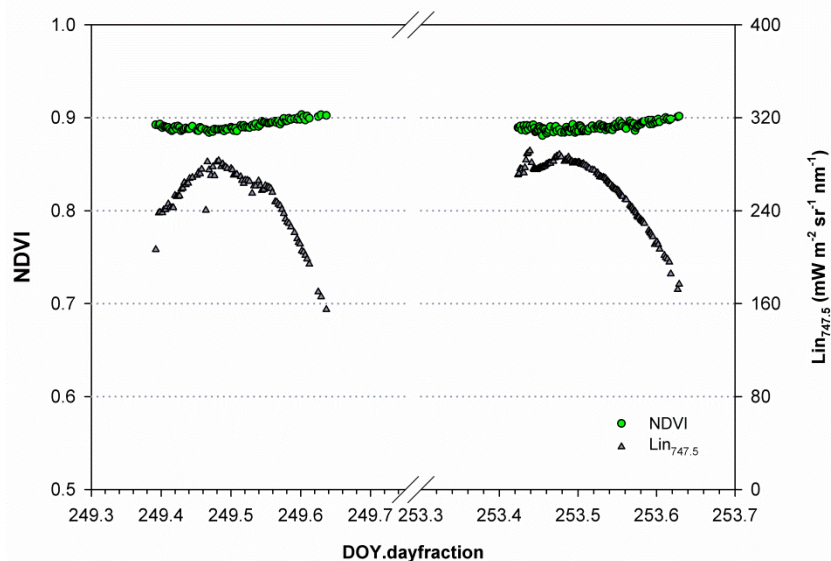


Figure 71: Time courses of the Normalised Difference Vegetation Index (NDVI) measured over the spruce forest from the mobile platform during 5 September (DOY 249) and 9 September (DOY 253). Lin_{747.5} is the incident radiance (mW m⁻² sr⁻¹ nm⁻¹) at 747.5 nm.

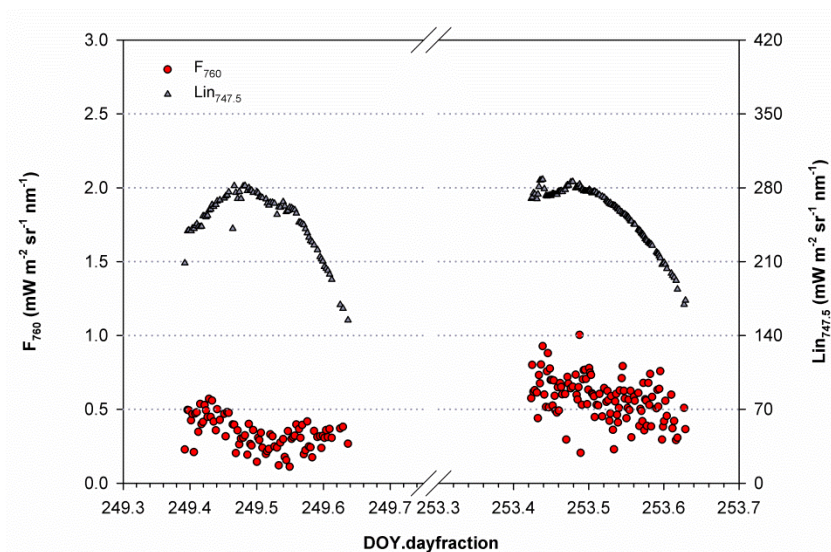


Figure 72: Time courses of F₇₆₀ (mW m⁻² sr⁻¹ nm⁻¹) measured over the spruce forest from the mobile platform during 5 September (DOY 249) and 9 September (DOY 253). Lin_{747.5} is the incident radiance (mW m⁻² sr⁻¹ nm⁻¹) at 747.5 nm.

Figure 73 shows the NDVI time series acquired with the S-FLUOR box installed on the eddy covariance tower over the spruce forest from 3–9 September. NDVI values were quite stable during the seven days of measurements, with value at midday around 0.86. At diurnal level, NDVI showed a characteristic shape due to the anisotropy of target reflectance in the red and near-infrared wavelengths generated by the movement of the Sun from sunrise to sunset. Near-infrared reflectance decreases in the morning with decreasing sun zenith angle and increases in the afternoon when sun zenith angle increases again; red reflectance increases in the morning with decreasing sun zenith angle and decreases in the afternoon when sun zenith angle increases again, probably because the optical path in the canopy is at its minimum when the

sun is at nadir. The anisotropy of the NDVI diurnal course is more evident in the time series collected from the eddy tower compared to the one measured from the mobile platform because of the off-nadir view used from the tower and because of the wider sampling area measured from the tower, including an highly variable proportion of shaded and sunlit crown components during the day.

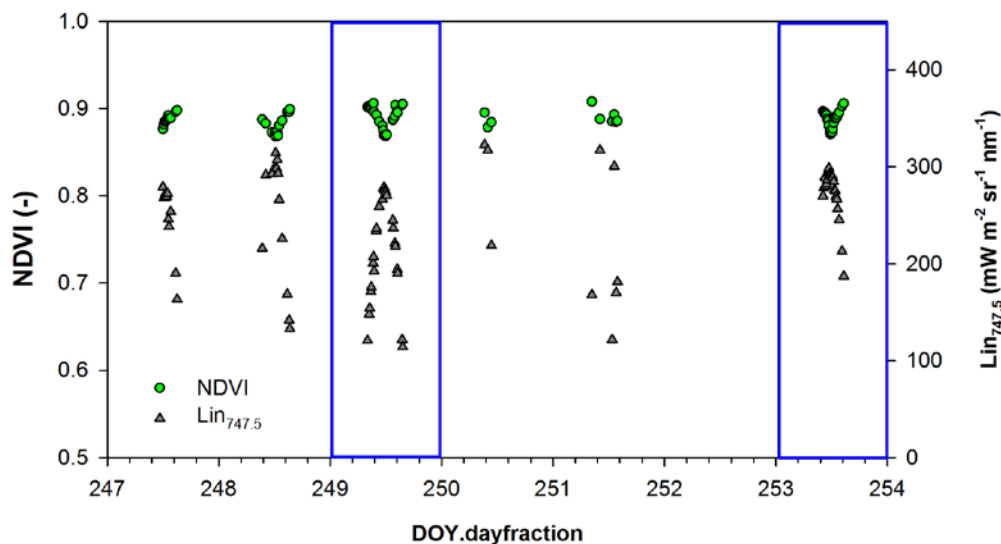


Figure 73: NDVI time series acquired with the S-FLUOR installed on the eddy covariance tower over the spruce forest. The blue boxes highlight the days of the airborne overpasses. $Lin_{747.5}$ is the incident radiance ($mW m^{-2} sr^{-1} nm^{-1}$) at 747.5 nm. DOY is day of the year.

Figure 74 shows the F_{760} time series acquired from the eddy covariance tower over the spruce forest from 3 to 9 September. F_{760} values were very low, with maximum values of $0.5 mW/m^2/sr^1/nm^1$ without a clear diurnal pattern.

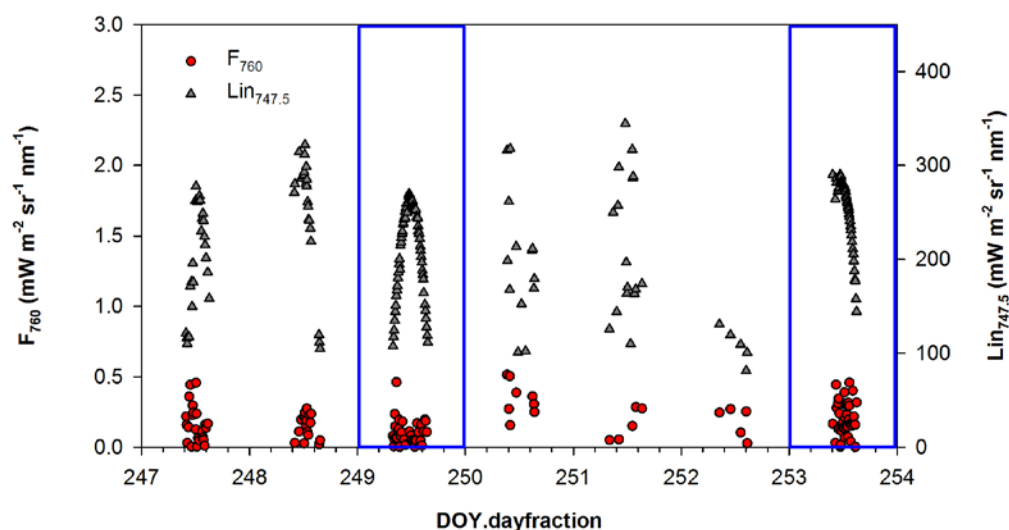


Figure 74: F_{760} ($mW m^{-2} sr^{-1} nm^{-1}$) time series acquired with the S-FLUOR installed on the eddy covariance tower over the spruce forest. The blue boxes highlight the days of the airborne overpasses. $Lin_{747.5}$ is the incident radiance ($mW m^{-2} sr^{-1} nm^{-1}$) at 747.5 nm.

5.4 Airborne mapping of fluorescence using the HyPlant sensor

More than 100 flight lines were recorded during the HYFLEX 2012 campaign. Not all of these flight lines can be processed; thus, we will define and process a core set of flight lines. In addition, four single lines were selected for scientific evaluation of the scientific objectives of this campaign:

- **Jülich campaign:**
 - 20120823-SEL-1350-0600-L2
 - 20120823-SEL-1423-1780-L2
- **Bílý Kříž campaign:**
 - 20120909-BK-1310-600-L3
 - 20120909-BK-1334-1800-L20

Three different methods to retrieve fluorescence maps from the HyPlant Fluorescence Imager were evaluated (Figure 75):

1. a standard 3 FLD like method that includes an atmospheric correction factor
2. a single vector deconvolution (SVD) approach, which was already used for retrieval from GOSAT data
3. spectral fitting methods (SFM). The SFM are the proposed retrieval method for the spaceborne FLEX mission. Thus, special emphasis was placed on further developing this retrieval approach, and two different approaches were evaluated in the frame of this activity.

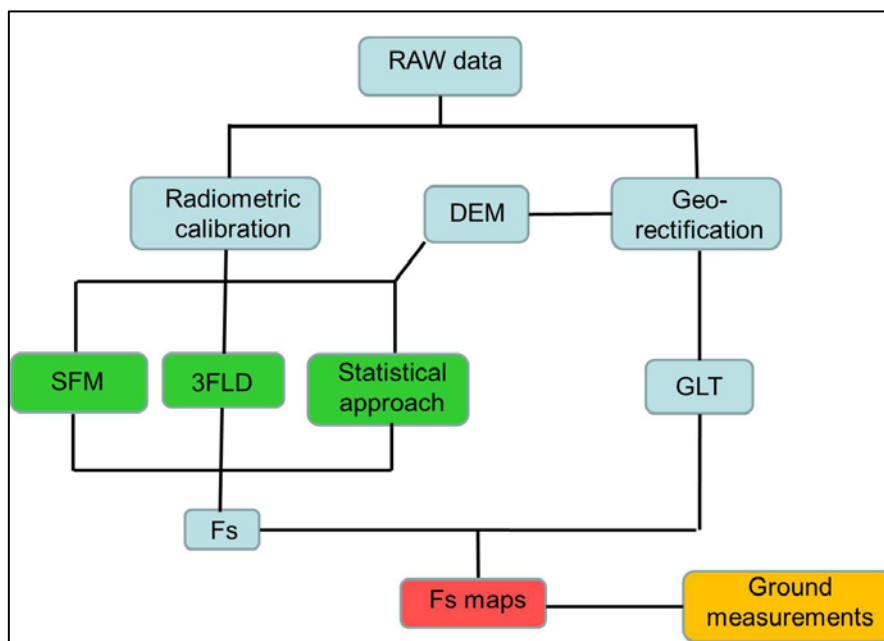


Figure 75: Processing scheme of the HyPlant Data. The retrieval algorithms were performed at radiometrically corrected and spatially unchanged data. Georectification and spatial resampling was performed after fluorescence retrieval.

5.4.1 3-FLD like method

5.4.1.1 Retrieval

Assuming that both spectral canopy reflectance (R) and FS can be considered Lambertian and E° isotropic, then the radiance signal (L) recorded by a sensor observing the canopy (Eq. 4) contains an additive FS signal:

$$L_{\lambda} = L_{\lambda}^p + \frac{\left(E_{\lambda}^0 \frac{R_{\lambda}}{\pi} + FS_{\lambda}\right) \cdot T_{\lambda}}{1 - S_{\lambda} \cdot R_{\lambda}} \quad (\text{Eq. 4})$$

with T accounting for the total atmospheric transmittance, L^p for the atmospheric path radiance, and S for the atmospheric spherical albedo.

The quantification of FS basically requires a separation of both fluxes, which is usually done by exploiting solar absorption lines (so called Fraunhofer lines) or atmospheric absorption bands. Within such absorption bands, the atmosphere appears dark, contrasts the reflected and the emitted flux, and allows the separation of both fluxes. The retrieval of FS using medium-resolution imaging spectrometers (1.0nm<FWHM<5.0nm) (e.g., AISA) is possible for at least the oxygen absorption feature around 760nm (O₂-A band) that originates from atmospheric molecular oxygen absorption (Corp et al. 2006, Liu et al. 2005, Louis et al. 2005). The O₂-A band overlaps with the FS emission spectrum and is wide enough to allow remote quantification of FS with common imaging spectrometers. The Fraunhofer Line Depth (FLD) method was proposed some time ago (Plascyk 1975) and has been successfully applied (Carter et al. 1990, Damm A. et al. 2010, Moya et al. 2004). Currently, the FLD method serves as a de facto standard for remote measurement of FS (see Meroni et al. (2009) for a recent review).

The FLD approach relates two adjacent spectral bands, a reference spectral band outside (o) of the absorption feature to one inside (i) and implicitly makes use of the different contrast between FS and R in these two spectral regions. The formalisation of the FLD concept leads to two equations (Eq.5), where E, T, L^p and S can be modelled using atmosphere radiative transfer models (RTM), for example, the MODerate spectral resolution atmospheric TRANsmittance algorithm MODTRAN-5 as it was used in this study (Berk et al. 2004). The R_i, R_o, FS_i, and FS_o components of the equation are unknown.

$$\begin{cases} L_i = L_i^p + \frac{\left(E_i^0 \frac{R_i}{\pi} + FS_i\right) \cdot T_i}{1 - S_i \cdot R_i} \\ L_o = L_o^p + \frac{\left(E_o^0 \frac{R_o}{\pi} + FS_o\right) \cdot T_o}{1 - S_o \cdot R_o} \end{cases} \quad (\text{Eq. 5})$$

The original FLD method closes up this equation system by assuming a constant R and FS for both spectral bands. Several studies have shown the weaknesses of this assumption (Alonso et al. 2008, Damm Alexander et al. 2011), and many improvements to the FLD concept were developed in the past (Meroni et al. 2009). The 3-FLD method proposed by Maier et al. (2003) was used in this study because it provides an acceptable accuracy of retrieved FS signals and was shown to be robust against noise (Damm Alexander et al. 2011). The 3-FLD method accounts for a linear variation of R over the investigated spectral range and reconstructs the slope of the background R flux by using two reference bands situated on the left and right shoulder of the absorption band. Considering this assumption of the 3-FLD method, FS can be analytically retrieved using equations 6–9.

$$FS = \frac{X_i(E_o^0 + X_o \cdot S_o) - X_o(E_i^0 + X_i \cdot S_i)}{(E_o^0 + X_o \cdot S_o) - (E_i^0 + X_i \cdot S_i)} \quad (\text{Eq. 6})$$

where

$$X_j = \frac{(L_j - L_j^p)}{T_j}, \quad j = i, o \quad (\text{Eq. 7})$$

and

$$E_j^o = \frac{1}{\pi} [E_j^o], \quad j = i, o \quad (\text{Eq. 8})$$

and

$$[E_o^o, L_o, L_o^p, S_o] = w_{o1} \cdot [E_{o1}^o, L_{o1}, L_{o1}^p, S_{o1}] + w_{o2} \cdot [E_{o2}^o, L_{o2}, L_{o2}^p, S_{o2}] \quad (\text{Eq. 9})$$

and

$$w_{o1} = \frac{\lambda_{right} - \lambda_{O2-A}}{\lambda_{right} - \lambda_{left}}, \text{ and } w_{o2} = \frac{\lambda_{O2-A} - \lambda_{left}}{\lambda_{right} - \lambda_{left}} \quad (\text{Eq. 10})$$

L represents the reflected at-sensor radiance flux of a fluorescent canopy, subscripts i and o indicate the wavelength positions within the O_2 -A absorption band and outside (reference band) of the absorption feature, respectively. The reference band located on the left side O_2 -A band is indicated with subscript $O1$, and $O2$ accounts for the reference band on the right.

Convolution of simulated signals

Spectral resampling of the simulated signals was required to meet the sensor configuration of the AISA-spectrometer. A two-step resampling approach as described in Damm et al (2011) was used and consisted of: i) the convolution of the input signal using a Gaussian function with a given FWHM; and ii) the sampling of the convolved signal considering a predefined SSI and an analytically retrieved spectral shift (SS).

Constrain of FS retrieval

The absolute accuracy of the retrieved FS signal depends on the quality of the radiometric input data and a-priori information required to model atmospheric parameters. Instrumental errors, for example, spectral shift residuals, vignetting effects, or other small deviations from nominal sensor characteristics, typically introduce a bias in the retrieved FS signals (Damm Alexander et al. 2011). Further, slightly inaccurate characterisations of the atmosphere that existed during data acquisition (e.g., aerosol load and its distribution) cause notable errors in the retrieved FS signals (Guanter et al. 2010).

The impact of the various sources of uncertainty can be semi-empirically compensated for by constraining the FS retrieval and considering surfaces with known FS emission (e.g., bare soil with zero emission). In the present study, the transmittance correction was applied, which was originally proposed by Guanter (2007). The approach analytically retrieves an effective transmittance T_{EFF} to correct L_{p0} and upward T . The effective upward T_{EFF} and $L_{p0_{EFF}}$ to be used in equations 6–8 are then formalised by equations.11 and 12.

$$L_{j_{EFF}}^p = L_j^p \cdot T_{EFF}, \quad j = i, o \quad (\text{Eq. 11})$$

and

$$T_{j_{EFF}} = T_j \cdot T_{EFF}, \quad j = i, o \quad (\text{Eq. 12})$$

This semi-empirical compensation requires measurements of non-fluorescent surfaces obtained under exactly the same condition as for the measurements of vegetated surfaces. A source of spatial variation can be related to the instrument's optical design (e.g., vignetting, spectral smile), which causes across-track variations and almost no variation along track. With this, we can expect temporal variations to be caused by the atmosphere and sensor-related aspects. To account for both the spatial and temporal variations, all bare soil pixels of each image were selected and averaged in along-track direction. The averaged, image specific across-track profiles were then used to obtain the T_{EFF} coefficients. Some images were characterised by a high fractional cover of vegetation, and only incomplete across-track T_{EFF} profiles could be obtained. In such cases, the missing T_{EFF} values were interpolated using T_{EFF} values of images acquired closest in time.

5.4.1.2 Fluorescence Maps

Agriculture

The abovementioned method was applied to selected flight lines from the campus Klein-Altendorf and the Selhausen area. In all flight lines, extended non-vegetated areas were present; thus, it was easy to select non-fluorescence pixels. Using these pixels, the effective atmospheric transmittance (T_{eff}) was determined for each cross-track position. Line-to-line variations were removed by fitting a 2-factor polynomial function

The fluorescence maps deliver consistent results throughout. Highest fluorescence values were found in sugar beet reaching maximum values of $2.5 \text{ mW m}^{-2} \text{ sr}^{-1} \text{ nm}^{-1}$ (Figure 76). Sugar beet is a bi-annual crop that is still green and has a dense healthy canopy during this time of the year. The plants generally show no sign of senescence and are harvested in October to November. Thus, the high fluorescence fluxes from sugar beet support the hypothesis that sugar beet is the most photosynthetically active group at this time of the year in the Selhausen area. Apple tree plantations (Figure 76) as well as natural pine and mixed forest (upper most part of flight line in Figure 77 and Figure 78) had lower values. All non-vegetated areas such as bare soil, roads, and building have fluorescence values very close to zero (Figure 76–78).

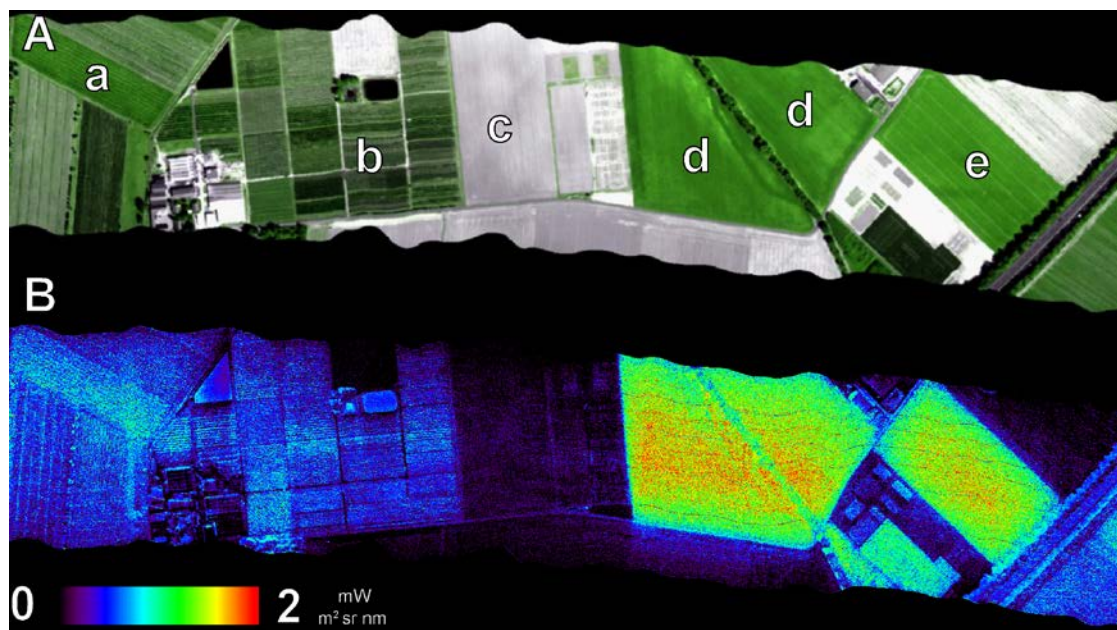


Figure 76: RGB (A) and fluorescence (B) values of the agricultural research campus Klein-Altendorf. Fluorescence was calculated from a flight line recorded 600m agl (flight line: 20120823_CKA_1533_600). Highest values were found in sugar beet (d). Apple trees (b) had lower

values, while all non-vegetated areas such as bare soil (c), roads, and buildings have fluorescence values very close to zero.

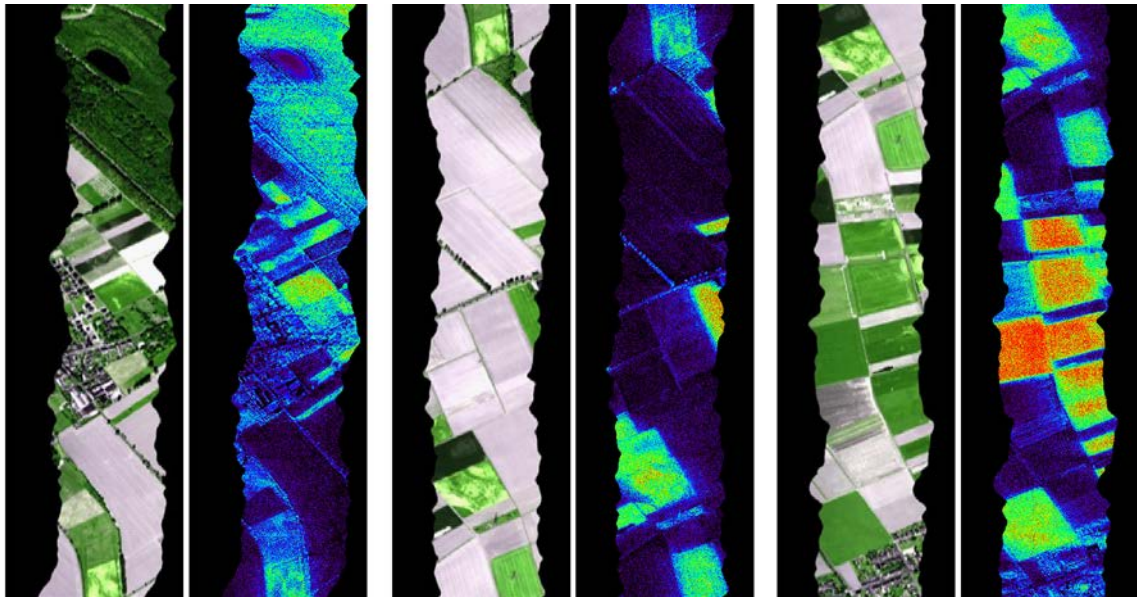


Figure 77: RGB and fluorescence values of the agricultural area derived from a flight line recorded 600m agl (flight line: 20120823_SEL_1350_600). Fluorescence values are coded with the same colour scheme as indicated in Figure 76.

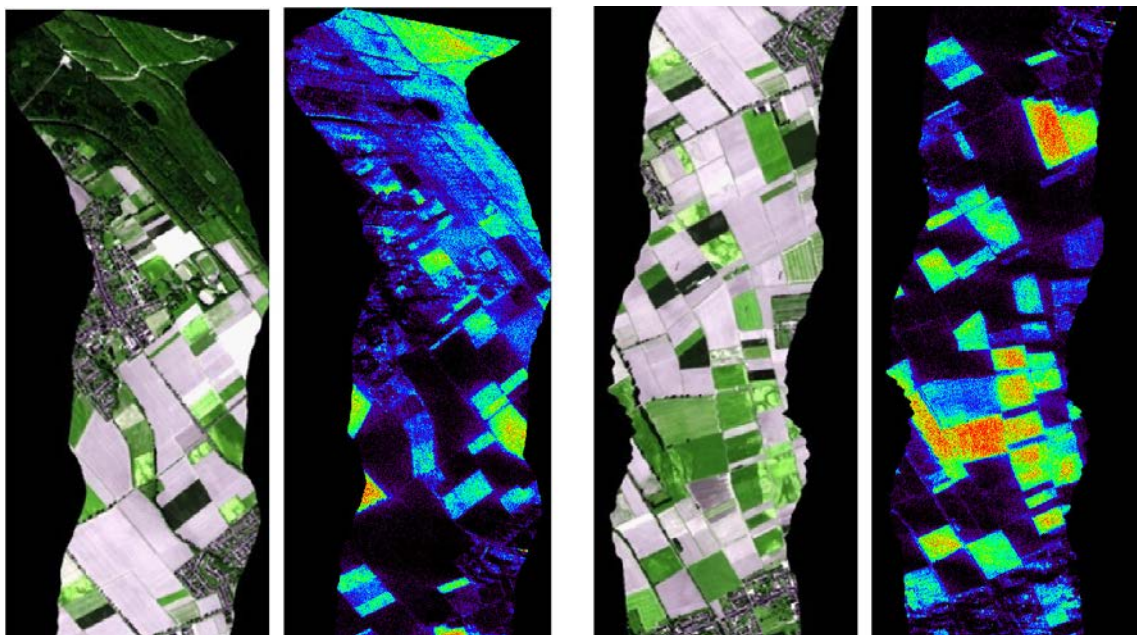


Figure 78: RGB and fluorescence values of the agricultural area derived from a flight line recorded 1780m agl (flight line: 20120823_SEL_1423_1780). Fluorescence values are coded with the same colour scheme as indicated in Figure 76.

The 3-FLD method was only used for the agricultural area and was not applicable for forest measurements of Bílý Kříž because the number of non-vegetation pixels is too small for a proper T_{eff} estimation. In addition, the 3-FLD method assumes a flat terrain for the whole flight

line. This is valid for the agricultural area in Jülich, but it does not account for the mountainous terrain in Bílý Kříž.

5.4.1.3 Comparison of fluorescence maps and TOC fluorescence

Resulting maps of canopy fluorescence were validated with a limited set of ground observations (c.f., 5.3.1.1). Figure 79 shows the agreement between ground-based fluorescence observations taken in two homogeneous agricultural fields (sugar beet and grass) and fluorescence values retrieved from HyPlant. We further investigated a bare soil field and assumed zero fluorescence emissions during the course of the day. Irrespective of the flight height, both HyPlant fluorescence maps are only slightly affected by offsets, and selected values are close to the 1:1 line.

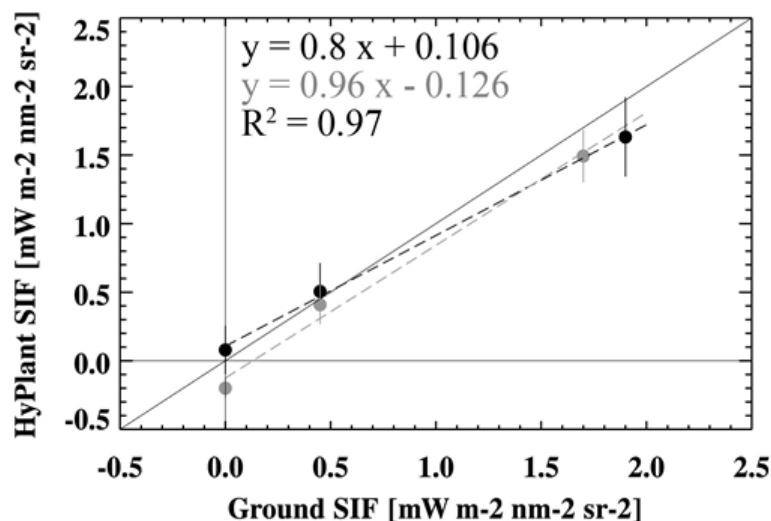


Figure 79: Comparison of ground and airborne-based fluorescence values from three selected crop types. Black dots correspond to sun-induced fluorescence (SIF) retrievals from data flown 600m agl, and grey dots represent SIF values retrieved from data flown 1780m agl. Shown error bars indicate the spatial variability of SIF within the respective fields.

We further evaluated the agreement of both fluorescence maps flown at 600 and 1780 m agl using an extended set of land cover types. From Figure 80, it becomes obvious that both maps agree well with a R^2 of 0.99. There is a slight additive offset where fluorescence values obtained from the high flight are systematically lower compared to fluorescence retrieved from the low flight. This deviation can be considered as realistic and can be related to a short time delay of data acquisitions. The high flight was performed roughly 40 min after the low flight, while the sun elevation angle already decreased during this time of the day. Chlorophyll fluorescence is induced by the surface irradiance, and consequently, emitted fluorescence values must decrease with decreasing sun elevation, irrespective of any physiological changes of the canopy. It is worth noting that the soil and water surfaces also show a decrease of fluorescence. The SNR of HyPlant and related data noise, however, causes uncertainties in retrieved fluorescence values (indicated as vertical and horizontal error bars in Figure 80), and variations of very small fluorescence values should not be interpreted as a physical response of the surface rather than a noise effect.

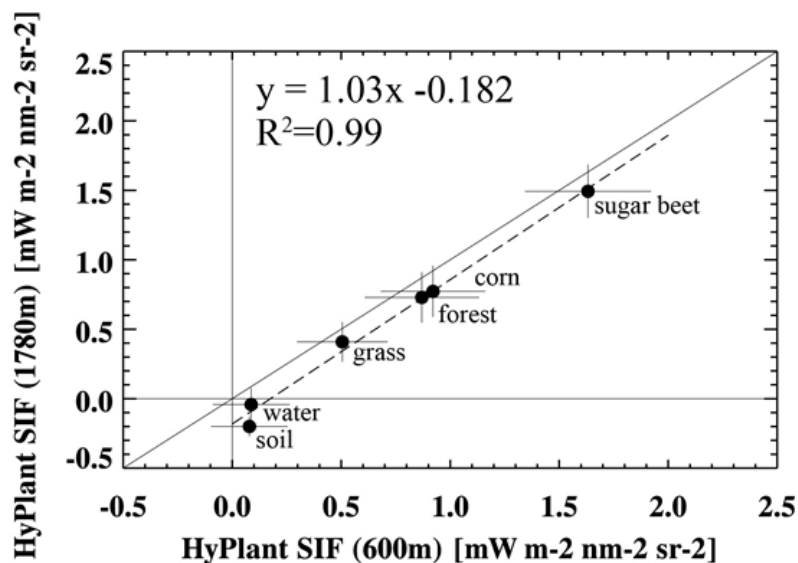


Figure 80: Fluorescence values measured from low (600 metre) and high (1780 metre) overpasses. Corresponding fields were manually selected and the field average of retrieved fluorescence values at 760 nm was compared between the two flight heights.

5.4.1.4 Discussion/Conclusion

Fluorescence maps calculated using the 3-FLD method are consistent and in general coincided with values estimated from the ground. The maps show intra- and inter-field variations of the fluorescence values. The 3-FLD Method including the T_{EFF} correction, is widely used. However, because the 3-FLD method needs to have a large amount of non-vegetation pixels to constrain T_{EFF} , the algorithm is not suitable for dense forest areas. In addition, the algorithm does not take into consideration topographic effects and different canopy heights. Varying fractions of diffuse and direct radiation at trees have a strong impact in the O_2-A band and increases the uncertainties in the red and NIR atmospheric transfer simulations.

5.4.2 Statistical approach for fluorescence retrieval based on singular vector decomposition (SVD)

5.4.2.1 Fundamental basis

The statistical retrieval approach is based on the methods described in Guanter et al. (2013) and Joiner et al. (2013). The main idea is that the measured radiance spectrum can be modelled as a linear combination of a fluorescence-free radiance spectrum plus the fluorescence. The other assumption is that the fluorescence-free spectrum can, in turn, be expressed as a linear combination of spectral functions convolved with a polynomial in wavelength: the spectral functions or singular vectors describe the spectral impact of the atmospheric radiative transfer, whereas the polynomial in wavelength accounts for the spectrally smooth variability in the surface reflectance. Under these assumptions, the forward model f for this statistical retrieval approach can be expressed as:

$$f(a_i, \alpha_i, \overline{F}_s) = \frac{\mu_s I_0}{\pi} \left[\sum_i a_i \lambda^i \sum_j \alpha_j v_j \right] + \overline{F}_s h_F T(\mu_v, \mu_s; T_{\uparrow} T_{\downarrow}) \quad (\text{Eq. 13})$$

where the polynomial $a_i \lambda^i$ represents the background surface reflectance, v_j are the singular vectors accounting for the atmospheric radiative transfer, a_j is the weight of the singular vector j , m_s is the cosine of the illumination angle, I_0 is the solar constant, \overline{F}_s is a scalar representing the intensity of the fluorescence signal within the fitting window, h_F represent a prescribed spectral shape for the fluorescence spectrum, and T is the atmospheric transmittance between the surface and the sensor. T can be estimated from the two-way transmittance defined by $a_i v_j$ or provided by external radiative transfer calculations. The forward model is non-linear in the first case and linear in the second. The unknowns in the inversion of the forward model are \overline{F}_s , a_i , and a_j . The basis of singular vectors is generated by singular vector decomposition of a training set of fluorescence-free spectra extracted from the data set to be processed. An example of the singular vectors calculated from a real HyPlant data set is shown in Figure 81.

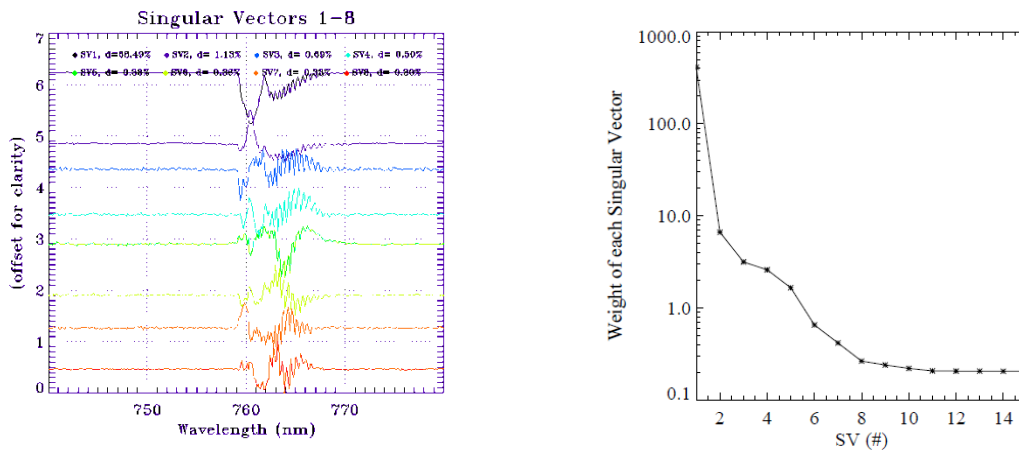


Figure 81: First eight singular vectors derived from a real HyPlant data set (left) and weight of the first fifteen vectors (right). Percentages in the legend refer to the relative contribution of each vector to the total variance.

This statistical approach is intended to circumvent limitations of explicit radiative transfer modelling and the impact of instrumental artefacts. No model assumptions as necessary as all atmospheric parameters (or their effects) are 'inverted'. The statistical method is faster and simpler compared to the physically based models doing explicit radiative transfer calculations

and inversion of atmospheric parameters. However, the approach needs training with non-fluorescence targets, which hamper the application over the most densely vegetated areas (although the requirements for such targets are less demanding than for FLD-like approaches). The statistical approach also needs some ‘fine-tuning’ of the polynomial degree and the number of singular vectors to be used for the processing at each site.

5.4.2.2 Fluorescence retrievals from HyPlant

The statistical retrieval method has been applied to HyPlant data acquired over the Selhausen and Bílý Kříž study sites. The two peaks of the fluorescence spectrum are sampled by fitting windows in 670–700 nm (first peak, centred at 690 nm) and 717–759 nm (second peak, at 740 nm). These two windows are selected through a sensitivity analysis as the ones for which the retrieval is the least biased by the background surface reflectance. Sample fits of the forward model f to real HyPlant spectra are shown in Figure 82. It can be observed that the forward model reproduces both the low and high spectral features within the fitting windows as is required for the estimation of the relatively low fluorescence signal.

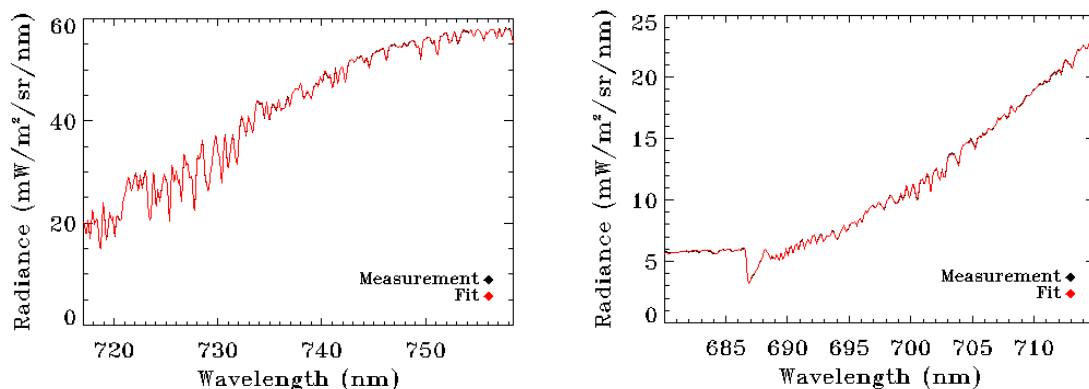


Figure 82: Fits of the forward model to real HyPlant spectra in the 717–759 nm (*left*) and 680–715 nm (*right*) spectral windows.

Agriculture

The maps of fluorescence at 740 and 690 nm derived over the Selhausen area on 23 August 2013 are displayed in Figure 5. The maps are for a flight line acquired in a high-altitude flight (1780 m above ground level) and a subset of a flight line from a low-altitude flight (600 m above ground level), both overpasses occurring within approximately 30 min.

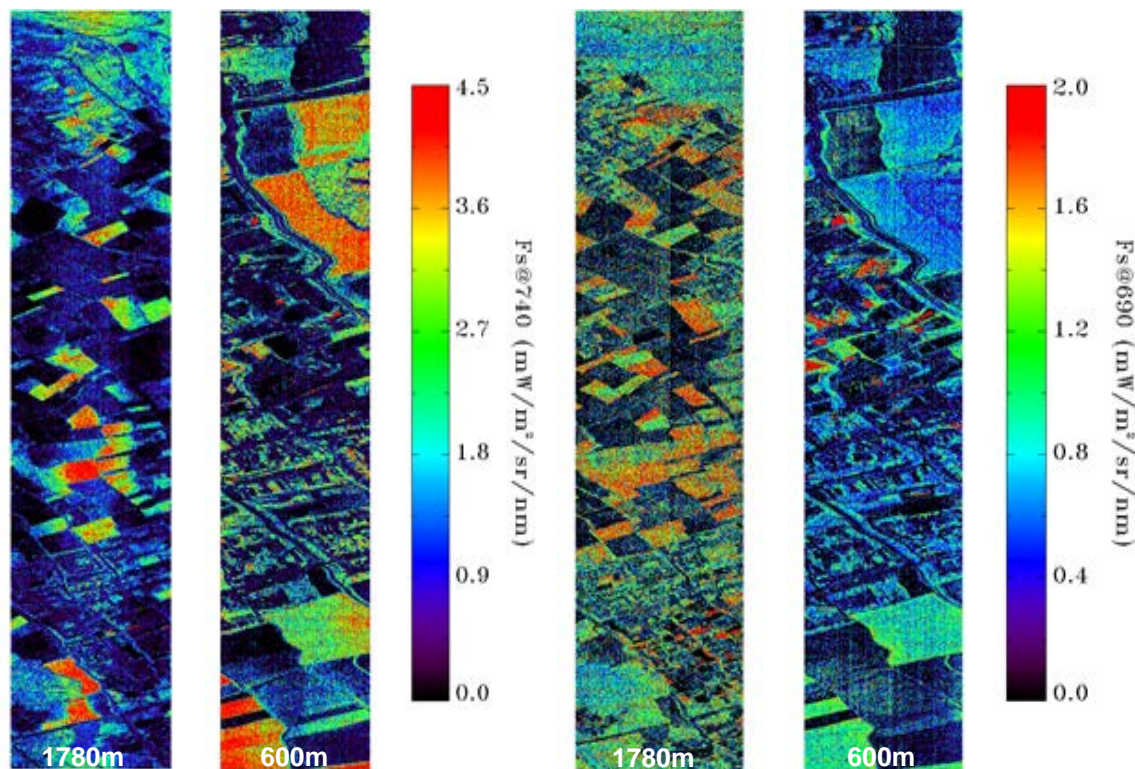


Figure 83: Fluorescence values at 740 nm (Fs@740) and 690 nm (Fs@690) derived from flight lines acquired in an altitude of 1780 m and 600 m above ground level.

Although the maps show a plausible distribution of vegetation and soil surfaces, some inconsistencies are also found. The values at 740 nm appear too high in comparison with the maximum of 2 mW/m²/sr/nm measured in-situ at 760 nm. Even though fluorescence at 740 nm is expected to be higher than at 760 nm due to the negative spectral slope of the fluorescence emission between 740 and 760 nm, the factor 2.5 between the measurements at those two wavelengths looks too large. An across-track gradient is also observed in the central part of the high-altitude flight. We can only explain this effect by an instrumental effect being captured by the singular vectors and propagated to fluorescence. Finally, the fluorescence values at 690 nm for the low-altitude flight are about 30–40% lower than those of the high-altitude flight. The reason for these inconsistencies in the results is still under investigation. One can a priori speculate that the extreme reflectance shapes at the red-edge window over this agricultural area (due to high chlorophyll content and/or leaf-area index) can make the fit of the forward model difficult. Also, the strong spatial and spectral contrast between the crops and the adjacent bare soil can cause stray light effects to be significantly higher over this area than over more homogeneous ones.

Forest

Sample maps of fluorescence at 740 and 690 nm derived with the SVD approach over the Bílý Kříž site on 9 September 2012 are displayed in Figure 84. The entire area shows high levels of green biomass as indicated by the NDVI maps, which are close to saturation, but strong differences are found in fluorescence at different vegetation cover for the two emission peaks. F_s is significantly lower in forest than in grassland areas, which can be explained by the different canopy structure, physiological functioning, or both.

Comparing the maps derived from the two flight altitudes at each spectral window in Figure 84, one can see that the results are more consistent than for the agricultural site. Peak values of 3 and 1.5 $\text{mW}/\text{m}^2/\text{sr}/\text{nm}$ at 740 and 690 nm, respectively, seem to match better the expected range of values.

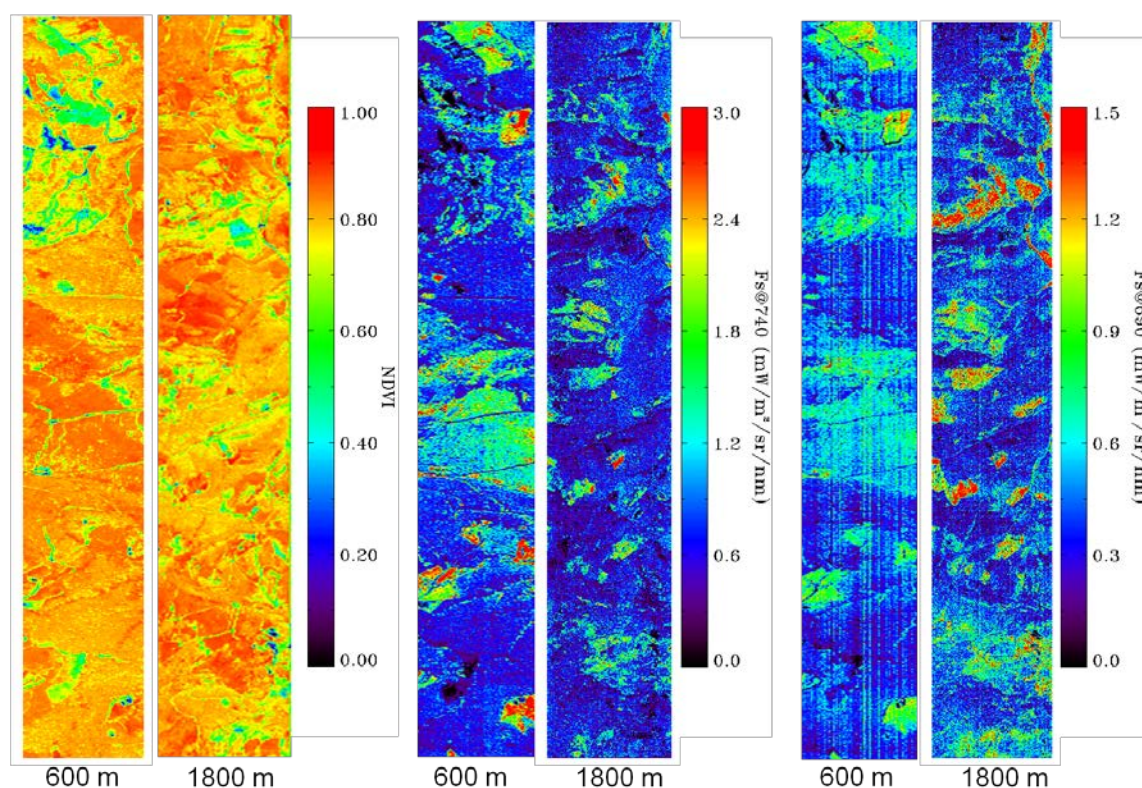


Figure 84: NDVI and fluorescence values at 740 nm and 690 nm of the forest area derived from two flight lines recorded at different altitudes (600 and 1800 m agl).

A time series of 690 nm fluorescence maps over Bílý Kříž on 9 September is displayed in Figure 85. Again, different fluorescence levels are observed for different types of vegetation cover within the maps. We can also observe how the intensity of the retrieved fluorescence signal is modulated by the diurnal cycle of illumination. The retrievals from close acquisition times (e.g., between 15:20 and 15:40) seem to agree very well with each other despite the fact that the different flight lines are processed independently.

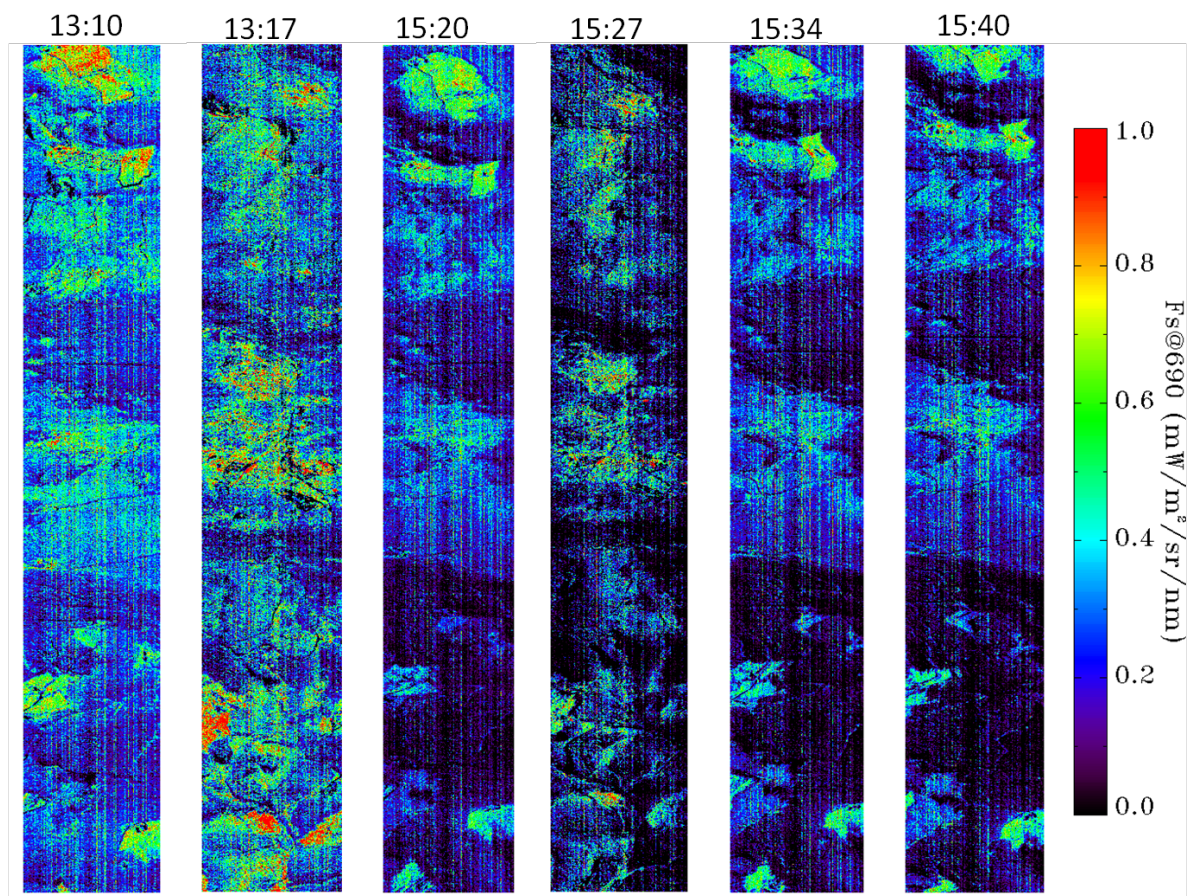


Figure 85: Time series of maps of fluorescence at 690 nm ($F_s@690$) derived from HyPlant acquisitions over the Bílý Kříž site on 9 September.

5.4.2.3 Comparison of fluorescence maps and TOC fluorescence

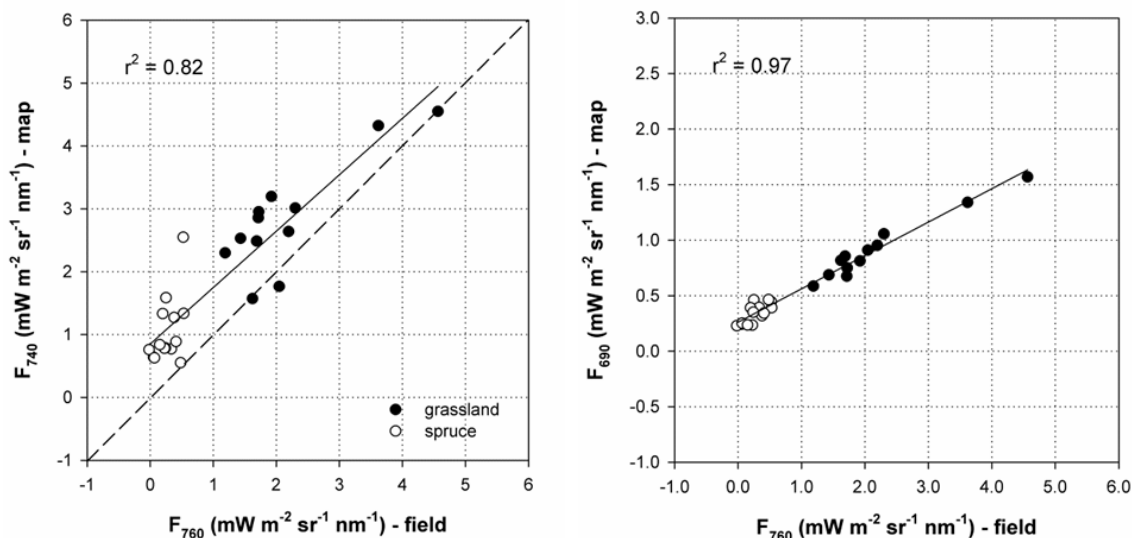


Figure 86: Comparison of airborne and field-based fluorescence retrievals over grassland and spruce forest areas. The field-based retrievals are performed at 760 nm, whereas airborne fluorescence is retrieved at 740 and 690 nm.

Figure 86 shows the comparison of airborne and field-based fluorescence retrievals over grassland and spruce forest areas. The comparison has been performed using all the low-altitude images collected over the four sampling points used for field measurements: two in the spruce forest (from the eddy covariance tower and from the mobile platform) and two in the grassland carpet (the control and the target treated with DCMU). Details about the flight lines used in the analysis are reported in the Table 21 below. Field-based fluorescence retrievals at 760 nm encompass a great range of variation: from F₇₆₀ values lower than 0.5 mW m⁻² sr⁻¹ nm⁻¹ measured in the spruce forest to values of about 5 mW m⁻² sr⁻¹ nm⁻¹ measured in the grassland carpet treated with DCMU. This great variation is also well captured by the fluorescence maps computed from the airborne images at both the O₂-A and O₂-B bands as highlighted by the high determination coefficients of the relationships between field and airborne retrievals (r² = 0.82 and 0.97 for the O₂-A and O₂-B bands respectively).

Table 21: Characteristics of the flight lines used for the comparison of airborne and field-based fluorescence retrievals over grassland and spruce forest areas.

Date	Local time	Altitude	Flight line number	Flight line number	Target
20120905	11.01	600	L2	20120905-BK-1101-600-L2-FLUO	Grassland
20120905	11.15	600	L3	20120905-BK-1115-600-L3-FLUO	Spruce forest
20120905	12.22	600	L2	20120905-BK-1222-600-L2-FLUO	Grassland
20120905	12.31	600	L3	20120905-BK-1231-600-L3-FLUO	Spruce forest
20120905	13.53	600	L2	20120905-BK-1353-600-L2-FLUO	Grassland
20120905	13.59	600	L3	20120905-BK-1359-600-L3-FLUO	Spruce forest
20120905	15.25	600	L2	20120905-BK-1525-600-L2-FLUO	Grassland
20120909	13.04	600	L2	20120909-BK-1304-600-L2-FLUO	Grassland
20120909	13.10	600	L3	20120909-BK-1310-600-L3-FLUO	Spruce forest
20120905	15.13	600	L2	20120909-BK-1513-600-L2-FLUO	Grassland
20120909	15.20	600	L3	20120909-BK-1520-600-L3-FLUO	Spruce forest
20120909	15.34	600	L3	20120909-BK-1534-600-L3-FLUO	Spruce forest
20120909	15.40	600	L3	20120909-BK-1540-600-L3-FLUO	Spruce forest

5.4.2.4 Discussion/Conclusion

The singular vector decomposition (SVD) method can be used to retrieve fluorescence at the two peaks of the fluorescence spectrum. It is a spectral fitting method in which the atmospheric radiative transfer is approximated on the basis of spectral vectors derived through singular vector decomposition of a reduced set of reference spectra; therefore, the retrieval does not require explicit atmospheric radiative transfer calculations and can be applicable over dense forest areas. This method has been used to retrieve the first fluorescence maps over dense forest areas and also to map the higher fluorescence levels emitted by a grassland carpet treated with DCMU. However, the retrieval results were not very consistent over the agricultural site in Selhausen, from which the derived maps showed across-track gradients and abnormally high fluorescence values. The reason for this site-dependent performance is still under investigation.

5.4.3 Spectral Fitting Method 1 (SFM-1, University of Valencia)

5.4.3.1 Retrieval based on apparent reflectance

For the retrieval of sun-induced fluorescence from TOC data, we propose a novel algorithm based on the difference between the peaks at the apparent reflectance and a baseline that corresponds to a hypothetical elimination of absorption features in the irradiance.

TOC radiance (L_{TOC}) can be described in terms of incoming total irradiance (E_{tot}), target directional reflectance (ρ_s), and emitted fluorescence (F):

$$L_{\text{TOC}} = \rho_s \cdot E_{\text{tot}} + F \quad (\text{Eq. 14})$$

From L_{TOC} , it is possible to derive an ‘apparent reflectance’ (ρ_{app}), which is the combination of the true directional reflectance of the target and the emitted fluorescence divided by the total irradiance:

$$\rho_{\text{app}} = \rho_s + (F/E_{\text{tot}}) \quad (\text{Eq. 15})$$

Figure 87 illustrates the difference between the true reflectance and the apparent reflectance that includes the effect of the fluorescence contribution to the total TOC radiance. The data has been extracted from the test database generated for FLEX-PARCS using the RTM SCOPE and corresponds to the reference case.

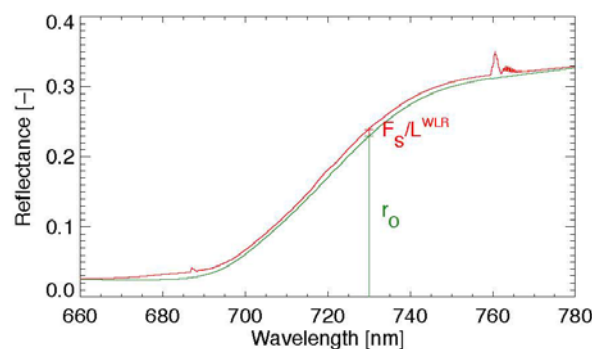


Figure 87: True reflectance (green) and apparent reflectance with the contribution of fluorescence (red).

Apparent reflectance presents some peak features that correspond to those wavelengths where the irradiance presents absorption features, the most prominent ones corresponding to O_2 absorptions. These peaks appear due to the difference in proportion between fluorescence radiance and total irradiance in each spectral band.

In case the irradiance is free of absorption features, for example, illumination from a halogen lamp, the apparent reflectance would present a smooth profile because all three terms of the equation are smooth.

In particular, if we could somehow obtain the total TOC irradiance free of O_2 absorptions (O_2 free atmosphere), then the resulting apparent reflectance would be smooth, without the O_2 peaks (note that the small Fraunhofer absorptions also produce peaks albeit very small ones). The difference between both cases can be expressed as:

$$\rho_{app} - \tilde{\rho}_{app} = \rho_s + \frac{F_s}{E_{tot}} - \left(\rho_s + \frac{F_s}{\tilde{E}_{tot}} \right) = F_s \cdot \left(\frac{1}{E_{tot}} - \frac{1}{\tilde{E}_{tot}} \right) \quad (\text{Eq. 16})$$

then,

$$F_s = (\rho_{app} - \tilde{\rho}_{app}) \cdot \frac{E_{tot} \cdot \tilde{E}_{tot}}{\tilde{E}_{tot} - E_{tot}} \quad (\text{Eq. 17})$$

The advantage of equations 16 and 17 is that the real reflectance, which has always posed a challenge in other retrieval strategies, is no longer involved in the retrieval process.

Our hypothesis are, first, that the smooth apparent reflectance ($\tilde{\rho}_a$) can be approximated by means of interpolation, and second, that eliminating the O_2 from the atmosphere in a radiative transfer model will have only a small impact in the multiple scattering outside of the absorption bands (Figure 88).

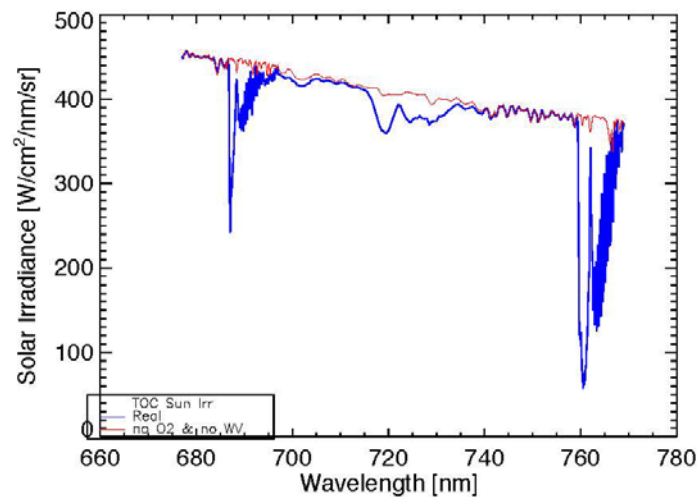


Figure 88: Solar irradiance (blue) and solar irradiance calculated with removed O_2 and water vapour (red), but all other constituents are maintained according to the RT model MODTRAN 5.

In order to properly interpolate the apparent reflectance spectrum, the resulting curve must be the lower envelope of the measured apparent reflectance. In order to achieve this, we selected a set of points where total irradiance with and without O_2 have a minimal difference and present a local maxima (Figure 89).

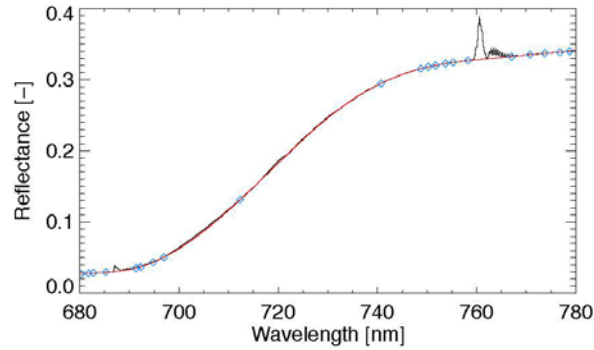


Figure 89: Apparent reflectance (black), interpolation points (blue diamonds), and resulting polynomial curve (red).

However, because the O_2 absorptions extend across several nanometres where the fluorescence values vary strongly, the resulting sun-induced fluorescence is estimated from a weighted average within defined spectral windows, three at O_2 -B and two at O_2 -A.

In this way, we obtain at least two points on the side of each peak, providing an indication of their slopes and the sun-induced fluorescence shape (Figure 90).

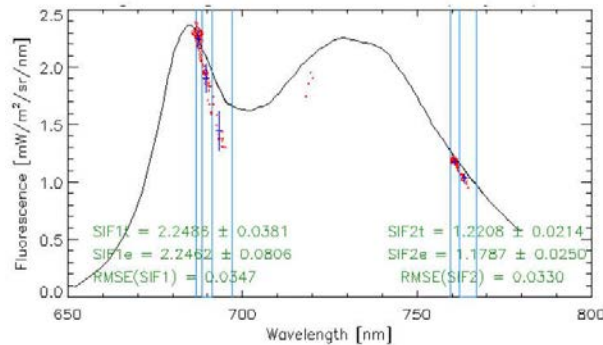


Figure 90: Sun-induced fluorescence (SIF) emission spectral signature. O_2 absorption bands are marked by vertical blue lines, where O_2 -B is divided in three spectral windows and O_2 -A in two.

The use of weights reduces the offset error, especially in the secondary absorptions, because signal noise and interpolation errors have a larger effect when the peak height is smaller.

The weights, in this first implementation, are obtained from the normalised ratio of apparent reflectances.

$$\omega_\lambda = \left(\frac{\rho_{app}}{\bar{\rho}_{app}} - 1 \right) / \max \left(\frac{\rho_{app}}{\bar{\rho}_{app}} - 1 \right) \quad (\text{Eq. 18})$$

Besides the weighting factors, because the uncertainties increase severely in those channels where the difference between the apparent reflectance and the interpolated one is small, a threshold value of 0.4 for O_2 -B and 0.6 for O_2 -A is applied to ω_λ in order to remove them from the retrieval (Figure 91). However, it is quite certain that a better estimation of the weights that also takes into account the SNR would improve the estimations.

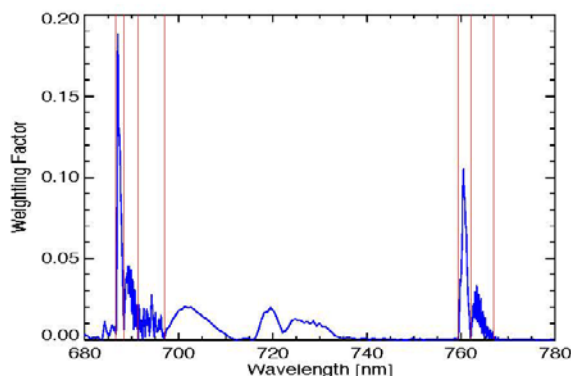


Figure 91: Weighting factors at each band according to Eq. 18. Each O₂ spectral window is delimited by vertical red lines.

Module description

The retrieval algorithm can be delineated in four main tasks:

1. lower envelope interpolation of apparent reflectance
2. application of retrieval Eq. 17
3. determination of weighting factors
4. estimation of accurate fluorescence by weighting average within selected spectral regions inside O₂ absorptions.

The retrieval module can be synthesised with the following flow chart (Figure 92):

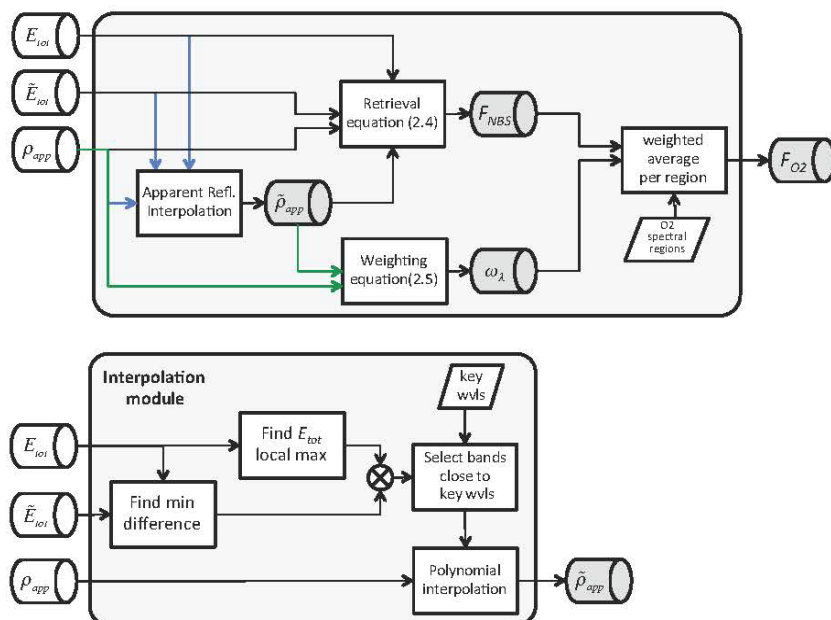


Figure 92: Flow chart of the sun-induced fluorescence retrieval algorithm (top), and for the interpolation module (bottom).

Input requirements

- TOC irradiance (with and without absorption features) and apparent reflectance from atmospheric correction module. NBS and WBS spectra must be merged into a single spectrum.
- Centre wavelength for each spectral channel taking into account spectral shift. Nominal spectral characterisation is not valid because the interpolation of the apparent reflectance makes use of key points that correspond to very precise spectral features, and failing to use the proper wavelengths could affect to the accuracy of the resulting interpolated curve.

Outputs

- Estimates of sun-induced fluorescence at all bands that fall within strong absorptions (i.e., where the values from Eq. 18 are above a given threshold), and with the same spectral sampling than the original FLORIS data (*FNBS* in the diagram).
- Mean sun-induced fluorescence at each oxygen absorption (O_2 -A and O_2 -B), averaged over the main absorption feature using the weights obtained from Eq. 18 together with their standard deviation (F_{O_2} in the diagram, Figure 92). Optionally, mean sun-induced fluorescence can be estimated from the secondary absorptions where radiometric resolution, noise levels, and interpolation accuracy allow it.

5.4.3.2 Fluorescence Maps

The spectral fitting method based on the apparent reflectance has been applied to the selected HyPlant FLUO data (Figure 93). It must be noted that the stray light detected in the instrument has an effect of distorting the spectral features of the absorptions, producing an additional in-filling of the absorption band but at the same time reducing the contrast between neighbouring peaks and valleys. No stray light correction has been applied so far. The overall result is that the overall spectral shape of the absorption cannot be fitted anymore; therefore, in order to test the concept of retrieval, we have selected single bands inside the absorptions that are farthest from contrasting bands. Also, the main absorption presents an increased height that translates into an overestimation of the fluorescence in both soil and vegetation. For this reason and because the algorithm does not make any correction for non-zero estimations over non-fluorescent targets, the overall result is a proper fluorescence distribution map with overestimated magnitudes.

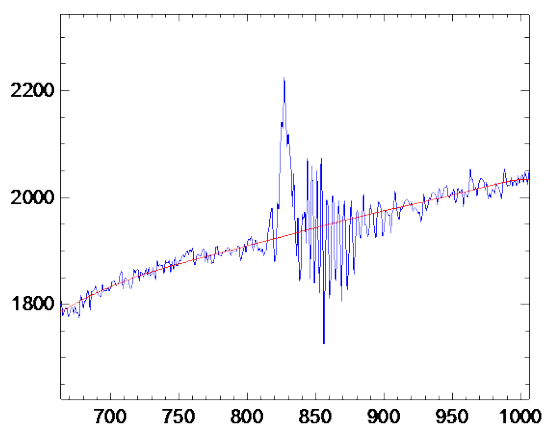


Figure 93: Fitting of the apparent reflectance of selected HyPlant data in the O_2 -A band.

Agriculture

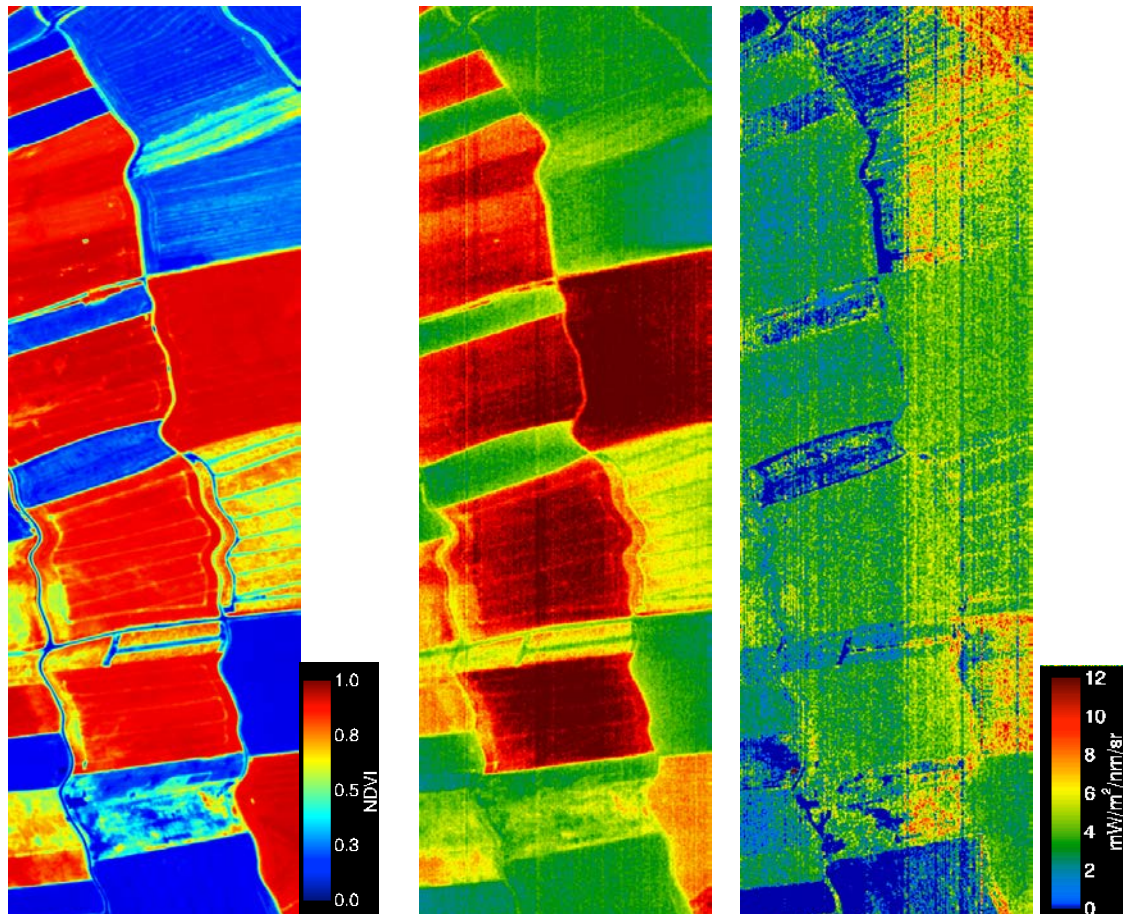


Figure 94: Maps derived from 600-m altitude over Selhausen using the apparent reflectance spectral fitting method. NDVI (*left*), sun-induced fluorescence at 760 nm (*middle*), and sun-induced fluorescence at 687 nm (*right*). Note that soil result in a fluorescence of about 3 mW/m²/nm/sr because there is no correction of baseline fluorescence.

Retrievals from both flight altitudes provide similar results (Figure 94, Figure 95). Looking at the colour scale it is evident that the estimated values in dense vegetation are about five to six times larger than reports from field measurements, especially in the O₂-A band. Values from the O₂-B band are more realistic, but we lack ground data for validation. In O₂-B, it is also clear that the dual read-out electronics (one for the leftmost 3/5 of the detector and another for the rightmost 2/5) produce different noise levels, resulting in a large fluctuation of the estimated fluorescence over bare soil in the rightmost 2/5 area, with values ranging between -20 and +15 mW/m²/nm/sr. This is not so severe in the 3/5 leftmost area of the detector (refer also to chapter 4.1 and RD-4).

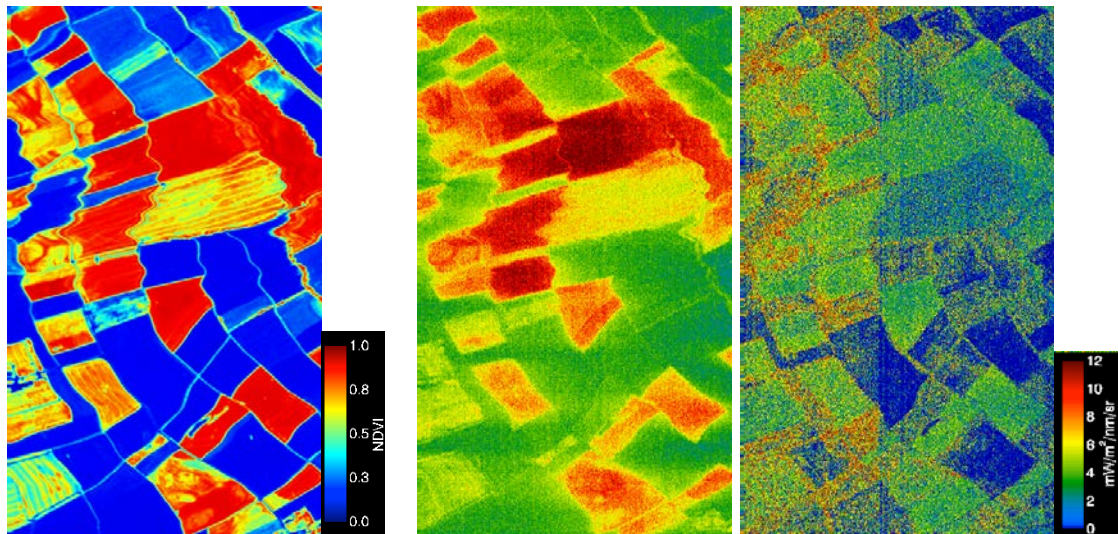


Figure 95: Maps derived from 1780 m altitude over Selhausen using the apparent reflectance spectral fitting method (images rotated to match low-altitude orientation). NDVI (*left*), sun-induced fluorescence at 760 nm (*middle*), and sun-induced fluorescence at 687 nm (*right*). Note that soil results in a fluorescence of about 3 mW/m²/nm/sr because there is no correction of baseline fluorescence.

Besides, the fluorescence map from O₂-A shows an across-track pattern that is consistent with long-reaching spatial stray light. The noise in O₂-B is clearly larger than in O₂-A (Figure 96). This is due to both the originally lower signal and the higher difficulty to do an accurate interpolation of the apparent reflectance although the stray light effect seems to be stronger in the O₂-A than the O₂-B band, at least in the spatial domain.

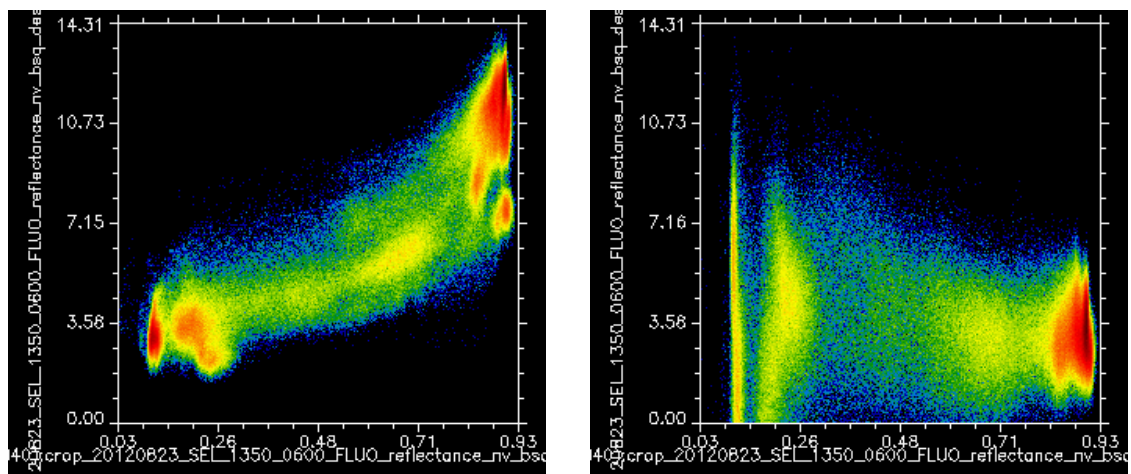


Figure 96: Scatter plot between NDVI (*x-axis*) and retrieved fluorescence (*y-axis*) from O₂-A (*left*) and O₂-B (*right*) absorptions at the low flight over Selhausen using the apparent reflectance spectral fitting method.

Forest

The atmospheric correction of the Bílý Kříž high-altitude (1780 m agl) flight image acquired on 9 September at 13:04 has been processed in two ways: 1) using a single average altitude for the whole mountainous scene; and 2) using the 1 m resolution DEM to estimate the actual altitude, slope, and orientation of the ground for each pixel of the scene. This allows the estimation of the impact of the topography on the accuracy of fluorescence retrieval.

At this moment, only the high-altitude flight image has been processed (Figure 97, Figure 98). The same restrictions to the application of the retrieval algorithm apply, that is, single-band evaluation due to spectral shape distortion and overestimation because no compensation is applied for zero-fluorescence at non-fluorescence targets.

The per-pixel correction takes into account the ground elevation of each one of the image pixels for the calculation of the atmospheric parameters of the radiative transport equation in the atmospheric correction. In the same way, it also takes into account the slope and aspect (orientation) of the surface in the calculation of the incoming direct irradiance; otherwise direct irradiance is considered to arrive to a horizontal flat surface. Figure 97 below shows the Bílý Kříž DEM (*left*) illuminated in the same manner as at the time of HyPlant overpass, an RGB of the image as acquired by the sensor (*middle*) showing the forest with different qualities of illumination due to the shape of the terrain, and after correcting the incident illumination for slope and orientation of the surface (*right*) where the topographic features are no longer evident, with exception of the shadows cast by tall trees at the edges of the forest or by high buildings.

To facilitate this correction without distorting the original image radiometry or increasing its already large file size, we have opted to project the original DEM to image space rather than the other way around. To do this, we needed to know the exact geographic coordinate of each individual pixel (that originally was not produced by Caligeo but finally implemented after our request) in order to find the closest pixel in the georeferenced DEM, then the altitude, aspect, and slope were stored in a new file that shared the geometry and space of the original image.

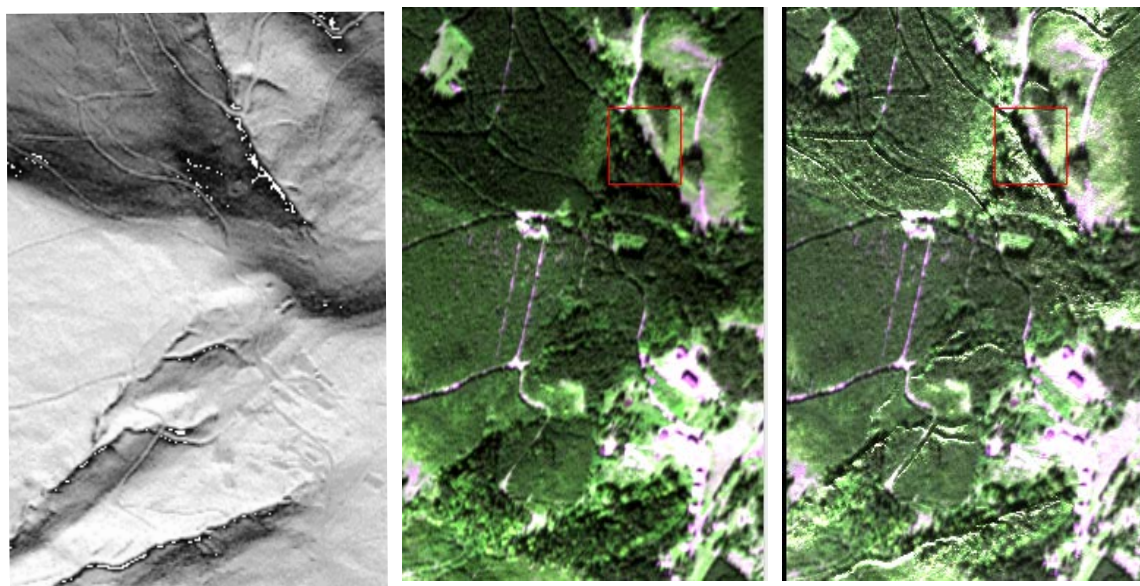


Figure 97: Solar illumination map (*left*) of the 1 m resolution DEM from Bílý Kříž at the time of the HyPlant overpass. RGB of the original image (*middle*) where topographic patterns are visible. RGB of the per-pixel-DEM-corrected image (*right*) where topographic patterns have been mostly removed.

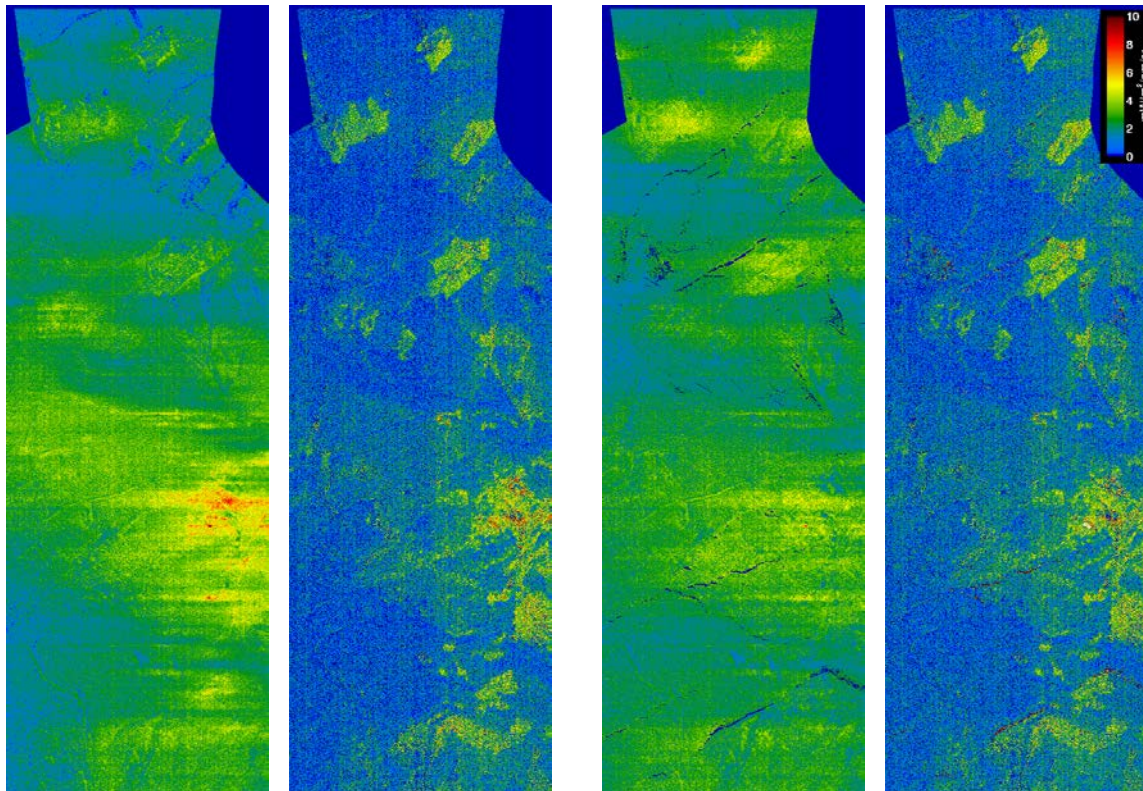


Figure 98: Estimated fluorescence maps derived from the high-altitude flight over Bílý Kříž using the apparent reflectance spectral fitting method at O₂-A (*far left*) and O₂-B (*middle-left*) using mean ground elevation for flat terrain, and O₂-A (*middle-right*) and O₂-B (*far right*) using per-pixel DEM ground elevation, slope, and aspect.

The improvements of a per-pixel atmospheric correction using DEM ground elevation and slope are clearly seen for the O₂-A band, as illustrated in Figure 98, where the range of fluorescence values has been greatly reduced (although still overestimated due to stray light), and the topographic pattern is less evident in the resulting map. The case of the retrieval in the O₂-B absorption benefits less, and only contrast is slightly improved in O₂-B. However, this limited improvement in the O₂-B band might be due to the image being dominated by noise rather than by the absorption itself. In fact, in Figure 99 below, a scatter plot of the results from O₂-A (*left*) shows how the range of estimated SIF using a mean altitude for the whole image is larger than when correcting using the altitude per pixel. At the same time, there is little correlation because the topography distorts the results in the mean-altitude case. The scatter plot of the results from O₂-B (Figure 99, *right*) shows a large correlation between both sun-induced fluorescence estimations, with a slightly larger dispersion along the X-axis, that is, when using the mean altitude. It must be noted, though, that a very small shift (in the order of one pixel) in the co-registration between the image and the DEM introduces some artefacts where there are roads that abruptly change the slope and the illumination correction is applied on the wrong location.

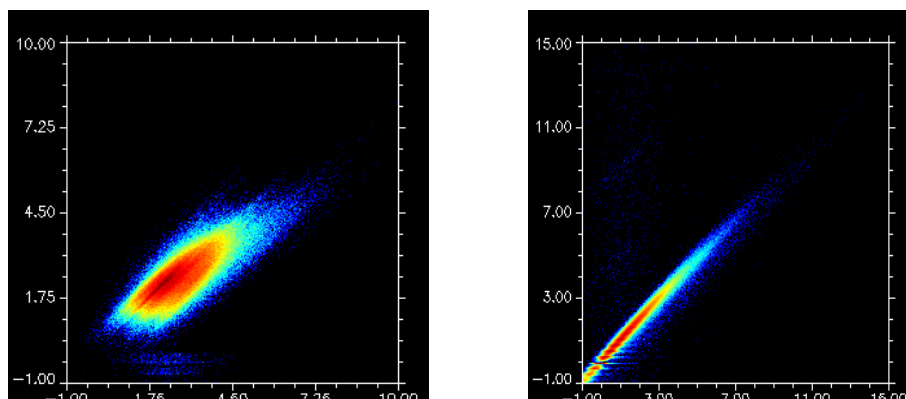


Figure 99. Scatter plot from flat terrain correction (x axis) vs per-pixel DEM correction (y axis) of retrieved fluorescence from O₂-A (*left*) and O₂-B (*right*).

5.4.3.3 Comparison of fluorescence maps and TOC fluorescence

Retrieval of fluorescence using the apparent reflectance spectral fitting method (SFM-1) over the agricultural and forest areas show a consistent spatial distribution with higher values at dense vegetation, lower at senescent and spare vegetation in crops, and overall low values in forest trees but higher in grass plots in the mountains. However, the absolute magnitude is much too high with respect to the field measurements, with estimated values of 10 to 12 mW/m²/nm/sr over the sugar beet site in Selhausen in contrast to the 2 mW/m²/nm/sr measured on the ground.

5.4.3.4 Discussion/Conclusion

This spectral fitting method (SFM-1) works on apparent reflectance data and uses the absorption features inside the O₂ bands and avoids the need to estimate true reflectance. The algorithm was successfully applied to model data and TOC spectrometer measurements providing results similar to the established and accepted SFM-2. Application of the SFM-1 to acquired HyPlant data resulted in computed fluorescence maps with higher values with respect to the ground reference measurements.

The detected sources of error for this overestimation reside both in the methodology (through the interpolation method for the apparent reflectance) and the sensor noise because the detected stray light and random noise have severe effects on the measured signal and spectral shape.

Because the apparent reflectance is derived from a physical modelling of the atmosphere, the results are as accurate as we can get, and targets identified as non-fluorescent are not corrected for any residual signal in-filling effects.

5.4.4 Spectral Fitting Method 2 (SFM-2, UNIMIB)

Preliminary results derived from the application of the fluorescence retrieval algorithm proposed by University of Milan-Bicocca to HyPlant images are presented in this section. The physically based algorithm under development is based on the atmospheric radiative transfer simulation using Modtran5 code, the 4-flux canopy-atmosphere interaction RT model, and the SFM to decouple fluorescence and reflectance. Preliminary advancements concerning the instrument stray light correction, in the spectral domain, are also shown.

5.4.4.1 Retrieval based on radiance data

The physically based algorithm proposed to retrieve the sun-induced chlorophyll fluorescence is based on the Spectral Fitting Method (SFM) to decouple the vegetation reflectance (r) and fluorescence (F_s) from total radiance (L) recorded by HyPlant. SFM relies on high-resolution observations to over-determine the mathematical system describing the radiance, reflectance, and fluorescence in the spectral domain considered. This allows us to reduce the impact of instrumental noise and provide accurate and more precise F_s values. Moreover, algorithm outputs include both the F_s and r spectral shapes that can provide further information about the plant status. It is well known that several parameters affect the SFM retrieval accuracy:

1. spectral range considered to fit the measured signal
2. the mathematical functions used to model reflectance (r) and fluorescence (F_s) in the considered range
3. sensitivity to sensor noise and finally
4. spectral information required to retrieve atmospheric parameters affecting the F_s retrieval (aerosol scattering and O_2 absorption).

A trade-off between these parameters must be found according to the considered dataset. The F_s retrieval algorithm for HyPlant presented in this work represents an evolution of the methods originally proposed by Meroni et al. (2010) and Mazzoni et al. (2012), which provide the inclusion of the recent advancements in atmosphere-canopy radiative transfer (RT) interaction modelling. Part of this study takes advantage of the current PARCS study aimed at the development and optimisation of the retrieval algorithm for the space-borne sensor FLORIS.

Radiative transfer between the atmosphere and a non-Lambertian heterogeneous Earth surface can be described with the so-called four-stream approximation. W. Verhoef recently adapted a model formulation that considers the additive contribution of fluorescence and its interaction with the atmospheric scattering and absorption (FLEX-PARCS, Task2 report-DRAFT). At-sensor radiance detected from a high-resolution sensor (L) is computed as in Equation 17.

$$\begin{aligned}
 L = & \rho_{so} \frac{E_s^o \cos \theta_s}{\pi} + \\
 & + \left[\frac{\tau_{ss} r_{so} E_s^o \cos \theta_s / \pi + F_s + (\tau_{sd} + \tau_{ss} \overline{r_{sd}} \rho_{dd}) E_s^o \cos \theta_s / \pi + \overline{F_d} \rho_{dd} r_{do}}{1 - \overline{r_{dd}} \rho_{dd}} \right] \tau_{oo} \\
 & + \frac{(\tau_{sd} \overline{r_{dd}} + \tau_{ss} \overline{r_{sd}}) E_s^o \cos \theta_s / \pi + \overline{F_d}}{1 - \overline{r_{dd}} \rho_{dd}} \tau_{do}
 \end{aligned} \tag{Eq. 19}$$

From this equation, the three major contributions are: 1) the atmospheric path radiance; 2) the radiance upwelling from the target; 3) the adjacency effect. E_s^o is the extra-terrestrial solar irradiance, F_s the solar-induced fluorescent radiance of the target in the observer's direction and $\overline{F_d}$ the hemispherical fluorescent emission of the surroundings. The ρ_{so} is the bi-

directional reflectance of the atmosphere, ρ_{dd} the spherical albedo, τ the transmittance terms. The subscripts are used respectively to indicate the incident light fluxes (s for solar and d for diffuse, first subscript), and the upward fluxes type on exit (o for radiance in the observer's direction and d for diffuse flux, second subscript). The surface reflectance terms represent r_{so} the bi-directional reflectance of the target, r_{do} the hemispherical-directional reflectance factor in the viewing direction of the target, $\overline{r_{sd}}$ the directional-hemispherical, and $\overline{r_{dd}}$ the bi-hemispherical reflectance factor of the surroundings. Over bars indicate spatial filtering over the area surrounding the target calculated as image average value at the different wavelengths.

The novel approach proposed by W. Verhoef considers fourteen atmospheric functions (Figure 102, *left table*) reducing the curve of growth effect (τ products performed at the highest Modtran5 spectral resolution, 0.1 cm^{-1}). In this study, atmospheric functions are convolved to the HyPlant instrument spectral-response function to consider actual sensor spectral shift and Full Width at Half Maximum (FWHM). The canopy-atmosphere interaction model can be reformulated according to Equation 18. In this context, the aim of the SFM is to solve equation 18 by finding the coefficients of the mathematical functions (such as, linear, polynomial, and Gaussian functions) used to represent r and F_s .

$$L = T_1 \left[T_2 + T_8 r_{so} + \frac{T_9 + T_{14} \overline{r_{sd}}}{1 - \overline{r_{dd}} T_3} r_{do} + \frac{T_{10} \overline{r_{sd}} + T_{11} \overline{r_{dd}}}{1 - \overline{r_{dd}} T_3} \right] + F_s T_6 + \left[\frac{\overline{F_d} (T_7 + T_{13} r_{do})}{1 - \overline{r_{dd}} T_3} \right] \quad (\text{Eq. 20})$$

The developed algorithm exploits the HyPlant Fluorescence module (hereafter FLUO) imagery. The processing chain currently developed is described as follows:

1. **Flickering pixels correction:** the IDL code provided by A. Damm and reported in the technical note '*Destriping algorithm for the HyPlant*', February 2013 [RD-5], was applied before other operations to correct sensor artefacts such as the flickering pixels present in the HyPlant raw imagery.
2. **Spectral Stray Light (SSL) correction:** the spectral Line-Spread Function ($f_{\text{LSFI},i}$), which describes the relative stray light response of the spectral channel i for every excitation wavelength j , was used to correct HyPlant data for the spectral stray light. HyPlant $f_{\text{LSFI},i}$ characterised using the measurements performed at the NASA calibration facilities is shown in Figure 100 (data provided by L. Alonso). An easy and computationally fast algorithm to correct SSL was proposed by Zong et al. (2006). This approach is based on a correction matrix D derived by combining the different $f_{\text{LSFI},i}$ functions for each HyPlant band. This function is modelled to take into consideration the 'In Band' (IB) signal using a Voigt spectral profile, a 10 nm wide trapezoid function with maximum at 2×10^{-3} , and the residual sensitivity to the farthest wavelength with a second Voigt profile. The resulting measurement equation used to correct measured signal is:

$$L_{meas,i} = L_{IB,i} + \sum_{j=1}^n (d_{i,j} L_{IB,j}) \quad (\text{Eq. 21})$$

where $L_{meas,i}$ is the total radiance measured at spectral band i , $L_{IB,i}$ is the IB signal for element i (i.e., the variable to be estimated), and the last term represents the SSL contribution (i.e., the sum of light at wavelength j that falls into band i). Results of the SSL correction algorithm applied to HyPlant spectrum is reported in Figure 100. It should be noted that hyperspectral imaging sensors are subjected to stray light originating in both the spectral and the spatial direction of the sensor. The algorithm introduced in the processing of HyPlant imagery accounts only for spectral stray light, which is expected to be the higher contribution within the oxygen absorption band. However, further developments should also investigate the impact of stray light originating in the spatial direction of the sensor before the F_s retrieval.

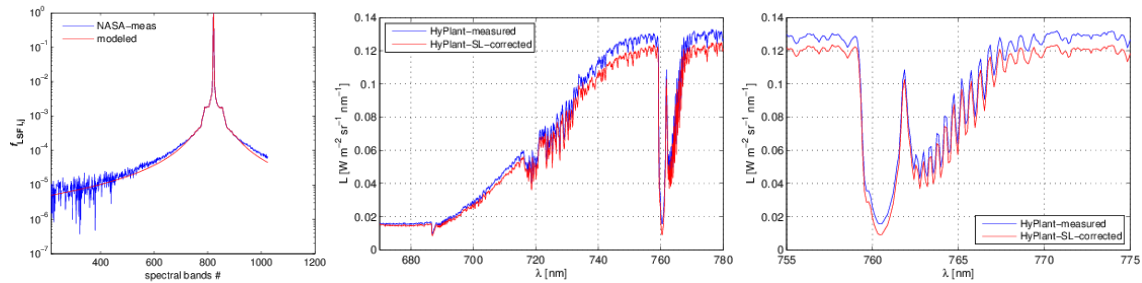


Figure 100: Spectral Stray Light correction of HyPlant data. $fLSFi,j$ (left); comparison between HyPlant raw and stray-light-corrected spectrum (middle). Zoom at the oxygen absorption band at 760 nm (right).

3. **Detection of spectral shift and FWHM:** accurate knowledge of the instrument spectral behaviour in terms of spectral shift and FWHM is a fundamental task to simulate properly at-sensor radiance. Considering imaging spectrometers is also important to characterise changes of band centres and bandwidth along the across-track (spatial) direction of the sensor (i.e., smile and band broadening). A systematic analysis of HyPlant spectral behaviour is performed for each flight line before F_s retrieval. As an example, the results for Selhausen and Bílý Kříž flight lines collected in 2012 are shown in Figure 101.

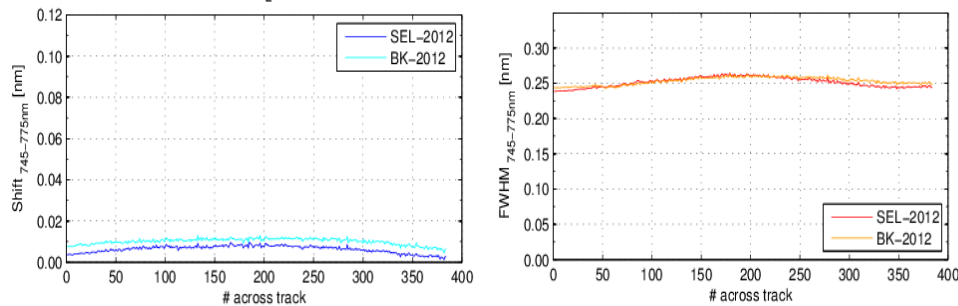


Figure 101: Across-track behaviour of HyPlant Spectral Shift and FWHM for Selhausen (flight line 20120823-SEL-1350-0600-FLUO) and Bílý Kříž (flight line 20120909_BK_1310_600_FLUO). Average values detected in the 745–775 nm fitting range are reported.

4. **Atmospheric effects simulations:** the fourteen atmospheric functions required in the retrieval model (Equation 18) are calculated using the atmospheric RT code Modtran5.2.1 at full spectral resolution (0.1 cm^{-1}) (Figure 102). Modtran input parameters are selected according the typical values (i.e., Mid-Latitude Summer, k-correlated, DISORT 8 streams, etc.) and geometric parameters during the HyPlant data collection (i.e., SZA, SAA, ground elevation, sensor altitude, etc.). In this step, atmospheric properties are not retrieved consistently from HyPlant imagery, but they rely on external data ('Characterisation of atmospheric properties to test the influence of atmospheric variations on the signal and for atmospheric correction', chapter 4.3.3). Aerosol Optical Density (AOD) estimated by sun photometer and lidar measurements was used. Modtran simulations performed at view-zenith-angles 0° , 8° , and 16° are afterwards interpolated at each of the 384 HyPlant spatial pixels in the image column direction. The resulting matrix contains the fourteen atmospheric functions for the different view angles that are resampled to the HyPlant spectral channels according to the spectral characterisation (point 3).

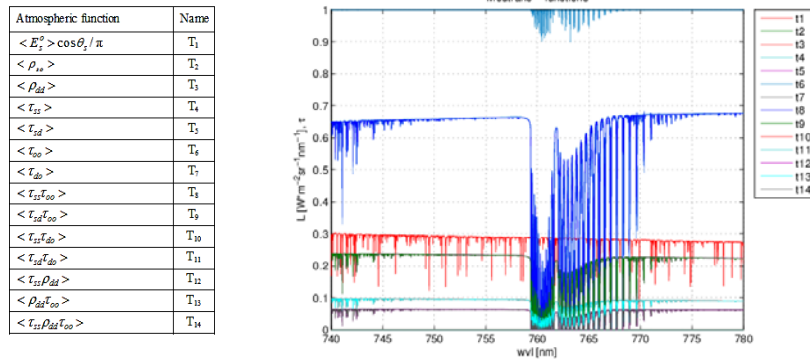


Figure 102: Atmospheric functions used in the canopy-atmosphere RT model. Table with the fourteen functions (<> operator represent the spectral convolution) on the left; spectral behaviours of the different functions at 0.1 cm^{-1} resolution are plotted on the right.

5. **Fs and r decoupling:** explicit decoupling of solar reflected radiance and fluorescence is based on the solution of the canopy-atmosphere interaction model in Equation 18. The coefficients of the mathematical functions used to represent Fs and r were numerically optimised using iterative non-linear optimisation techniques minimising the following objective function:

$$\min \sum_{\lambda} (L_{mod}(\lambda) - L_{meas}(\lambda))^2 \quad (\text{Eq. 22})$$

where L_{mod} and L_{meas} are the SFM modelled by Equation 18 and measured at sensor radiance, respectively. In this preliminary phase, the retrieval concept is tested considering: a) basic (i.e., linear) functions representing reflectance and fluorescence; b) a narrow fitting window, 759–770 nm; c) external atmospheric AOD and SPR values; d) surface reflectance and fluorescence Lambertian behaviour i.e., $r_{so}=r_{do}$ and $r_{dd}=r_{sd}$.

The current algorithm provides five different imageries as output: 1) Fs from SFM; 2) r from SFM; 3) Fs at 760 nm using FLD; 4) r at 760 nm using FLD; 5) NDVI. Further developments will extend the study in order to: i) retrieve fluorescence and its spectral behaviour over broader fitting ranges; ii) retrieve atmospheric parameters consistently from HyPlant imagery; iii) include the surface non-Lambertian behaviour. The algorithm described in this section has been implemented in Matlab2013Rb development environment.

5.4.4.2 Fluorescence Maps

The SFM retrieval method has been tested on selected flight lines collected over the Selhausen agriculture area at different flight heights. The results relative to a spatial subset of the original imagery covering different land cover types (i.e., sugar-beet field, bare soil, and urban area), including the area where top of canopy F_s measurements have been performed, are presented in this section.

F_s was retrieved from both the raw radiance HyPlant 20120823_SEL_1350_0600_FLUO flight line and from the same HyPlant image after a preliminary stray light correction. Profiles of F_s , r , and NDVI values along a horizontal spatial transect (Transect-1) through the image (indicated on the true colour image, Figure 104) are reported in Figure 103. The profiles derived from the original HyPlant image are depicted on the left panel, while those derived from the corrected image are on the right. In both cases, F_s , r , and NDVI show a similar trend, with low values on the left part of the profile, corresponding to bare soil (up to pixel# 190), and then the signals rise quickly in correspondence to the sugar beet field with high vegetation biomass. A weak reduction of F_s within the vegetated field (right part of the profiles) is due to spatial heterogeneity because the same pattern (minimum in the field centre) is shown by r and NDVI. The F_s values retrieved without the stray light correction reach $12 \text{ mW} \cdot \text{m}^{-2} \cdot \text{sr}^{-1} \cdot \text{nm}^{-1}$, while they are lower and more consistent to the ground measurements after the spectral stray light correction. The F_s values retrieved after the spectral stray light correction appear more scattered compared to non-corrected data because they are shown in a smaller absolute scale.

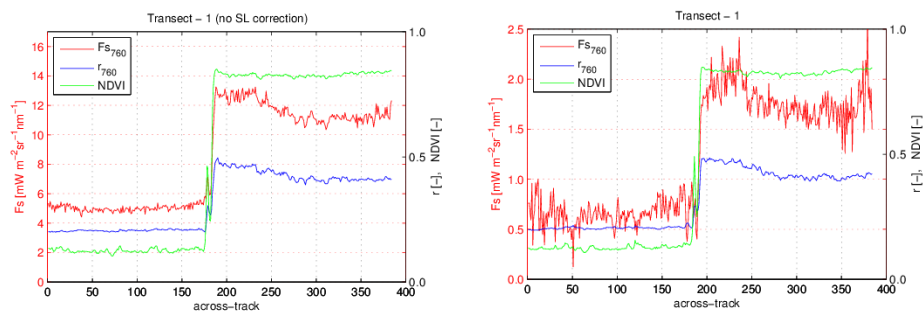


Figure 103: Spatial transects of sun-induced chlorophyll fluorescence (red line), reflectance (blue line) at 760 nm, and NDVI (green line). Transect-1 retrieved from original HyPlant image (*left*) and HyPlant corrected for the spectral stray light (*right*).

Fluorescence, reflectance, and NDVI maps derived from the flight line 20120823_SEL_1350_0600_FLUO after the spectral stray light correction are shown in Figure 104. The spatial patterns are well represented by the fluorescence image. As expected, agricultural fields with higher green biomass show higher fluorescence values; on the contrary, bare soil and urban areas have lower F_s values. Absolute values of F_s at 760 nm range from 0.0 to $3.0 \text{ mW} \cdot \text{m}^{-2} \cdot \text{sr}^{-1} \cdot \text{nm}^{-1}$, which is similar to values obtained from ground-based measurements (reference measurements of about $2.0 \text{ mW} \cdot \text{m}^{-2} \cdot \text{sr}^{-1} \cdot \text{nm}^{-1}$ in the sugar beet field). However, the striping algorithm introduces some noise on the left and right edges of the image (results over raw imagery do not show this effect).

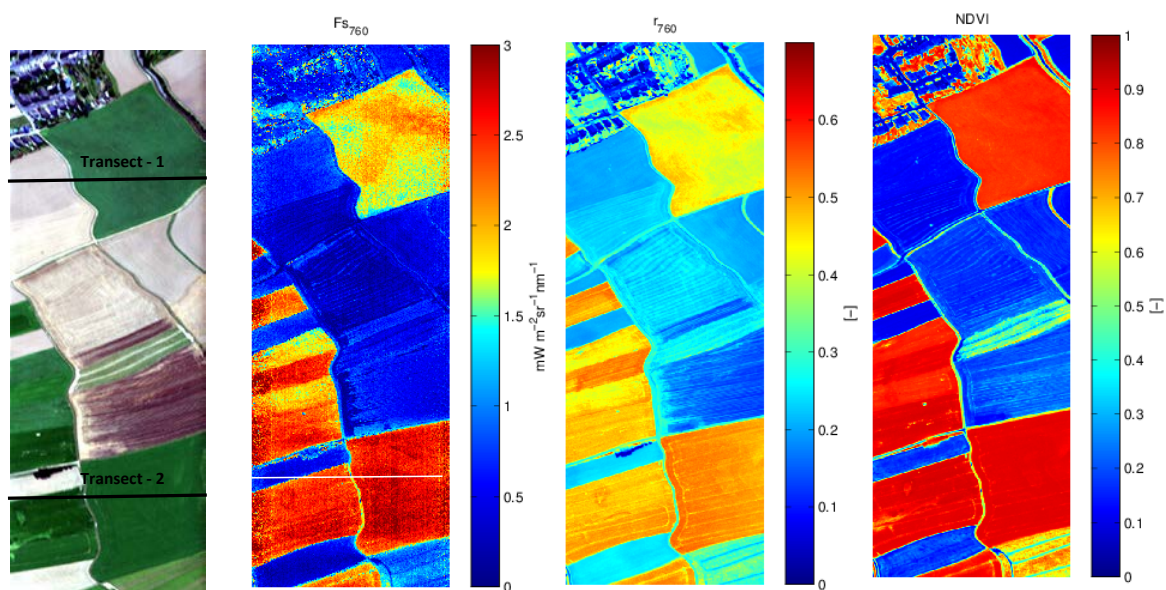


Figure 104: Subset of the flight line 20120823_SEL_1350_0600_FLUO_radiance collected at 13:50 local time on 23 August 2012 at 600 m agl. True colour image from HyPlant dual imager, fluorescence at 760 nm (Fs_{760}), reflectance (r_{760}), and NDVI imagery of Selhausen agricultural area are shown from left to right respectively.

Fluorescence and spectral indices maps derived from the flight line recorded at 1780 m agl (20120823_SEL_1423_1780_FLUO) are depicted in Figure 105. Results from both flight altitude lines are similar. The high-altitude flight was recorded 30 minutes later (with a higher SZA), and for this reason the Fs values are slightly lower. A similar decrease was observed also in the ground based fluorescence measurements.

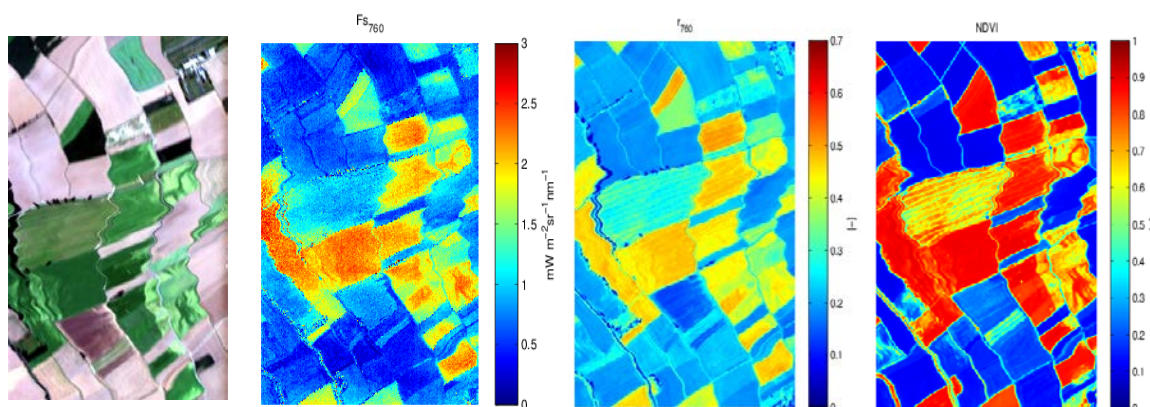


Figure 105: Subset of the flight line 20120823_SEL_1423_1780_FLUO collected at 14:23 local time on 23 August 2012 at 1780 m agl. True colour image from HyPlant dual imager, fluorescence at 760 nm (Fs_{760}), reflectance (r_{760}), and NDVI imagery of Selhausen agricultural area are shown from left to right respectively.

5.4.4.3 Comparison of fluorescence maps and TOC fluorescence

The comparison between F_s values retrieved from HyPlant and top-of-canopy field measurements are briefly presented in this section. Figure 106, left plot, shows the across-track spatial profile at the image line corresponding to ground-based measurements. Figure 106 is derived from the low-altitude flight (Transect-2, Figure 104). From left to right, values representing bare soil and two distinct sugar beet fields are shown. The boundary between two green fields is evident at spatial pixel #200. We can observe that even when the NDVI values of the two vegetated fields are similar, the F_s differs. Top-of-canopy measurements (spatial pixel #163–165) are represented with the red bar.

The plot on the right in Figure 106 shows F_s values over selected regions of interest (ROI) of about 3×3 pixels within the low- and high-altitude F_s maps corresponding to ground measurements. Absolute F_s values are in the range of ground-based measurements, but for both the low- and high-altitude imagery, the retrieved values are slightly overestimated. The bias found for the low-altitude flight is almost the same as the residual error (fluorescence over non-vegetated surfaces) observed in the F_s spatial profile. This could be due to errors in either the modelling of atmospheric effects or the residual uncertainty in the stray light correction, which is not yet perfected. The latter is twofold: 1) there is some remaining uncertainty regarding the quality of our current spectral stray light correction method; 2) spatial stray light correction has not yet been not considered.

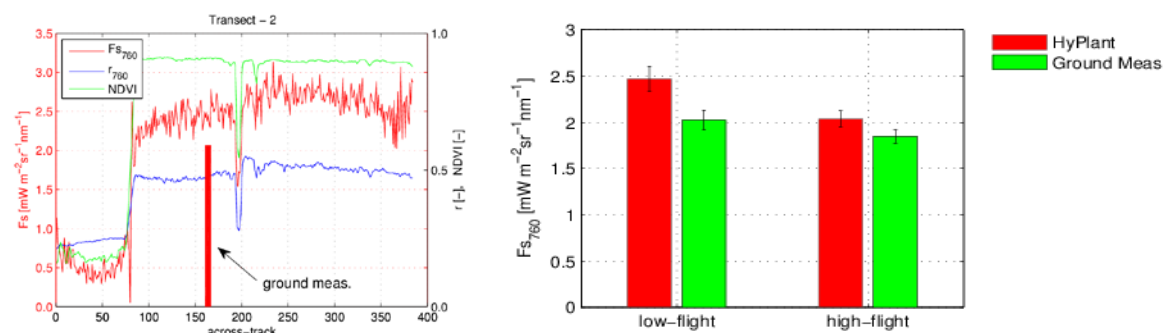


Figure 106: Comparison between ground-based and F_s values retrieved from low- and high-altitude flights over selected ROI.

5.4.4.4 Discussion/Conclusion

The retrieval algorithm based on SFM decoupling of fluorescence and reflectance modelled according to 4-flux canopy-atmosphere RT model for HyPlant data has been developed. The algorithm has been tested on selected flight lines collected in agricultural ecosystems. A preliminary evaluation of the spectral stray light correction algorithm has been performed and resulting F_s values seem more accurate (i.e., close to ground measurements). However, further investigations concerning the stray light effects in the spectral and spatial direction of the sensor are needed to develop a correction algorithm that includes both the spectral and spatial direction of the image sensor and to have a better laboratory characterisation. F_s maps achieved after the pre-processing of the HyPlant imageries for the spectral stray light seem significantly improved. In general, the spatial patterns of F_s are well reproduced, whereas absolute values are close but still slightly higher compared to ground validation measurements. Currently, the causes of the remaining bias are still unknown, and further investigations are needed. In particular, on-going activities are aimed at a consistent characterisation of atmospheric parameters directly using HyPlant imagery and at the improvement of the instrument's stray light correction. Finally, the developed algorithm has been tested only at the O_2 -A band, and further activities will exploit the O_2 -B band as well.

5.5 DCMU experiment – Biochemical block of photosynthesis

For the grassland experiment, two lawn carpets (12 x 12 m each) were laid on plastic sheets. The species composition of the grassland was *Festuca rubra*, *Lolium repenne*, and *Poa pratensis*.

The carpet was treated on 5 September at 08:00 local time by 3-(3,4-dichlorophenyl)-1,1-dimethylurea (DCMU) diluted to 10⁻⁵ M in 1% ethanol/water. On 9 September at 10:00 local time, the carpet was treated again with 10⁻⁴ M DCMU. On both days, the control carpet was treated at the same time with ethanol/water without the herbicide.

After the treatment, both lawn carpets were measured alternatively with two different instruments. One instrument is an ASD Field Spec small hydraulic movable platform (up to 12 m above surface); the second is the MRI system with two Ocean Optics HR4000 (see chapter 4.3.1) measuring approximately 150–170 cm above ground (Figure 107). In addition, leaf level measurements with a imaging PAM System were conducted (Figure 108).

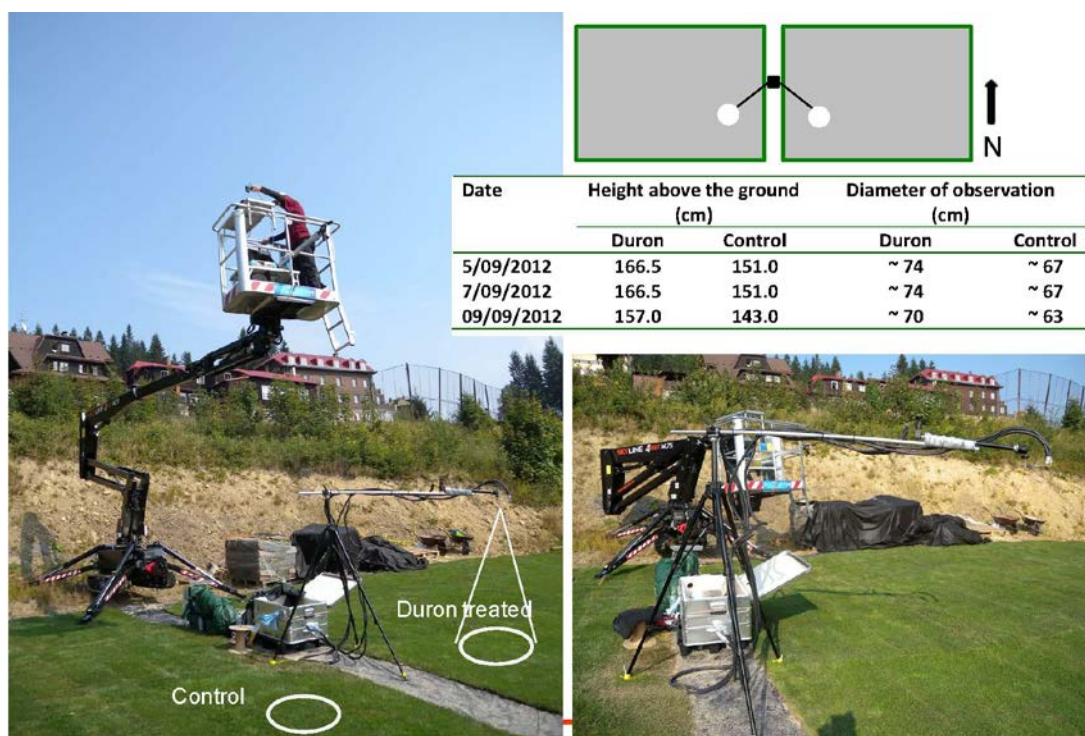


Figure 107: Set up of the grassland experiment.



Figure 108: Measurements of the lawn carpet with the Imaging PAM system.

5.5.1 Leaf level

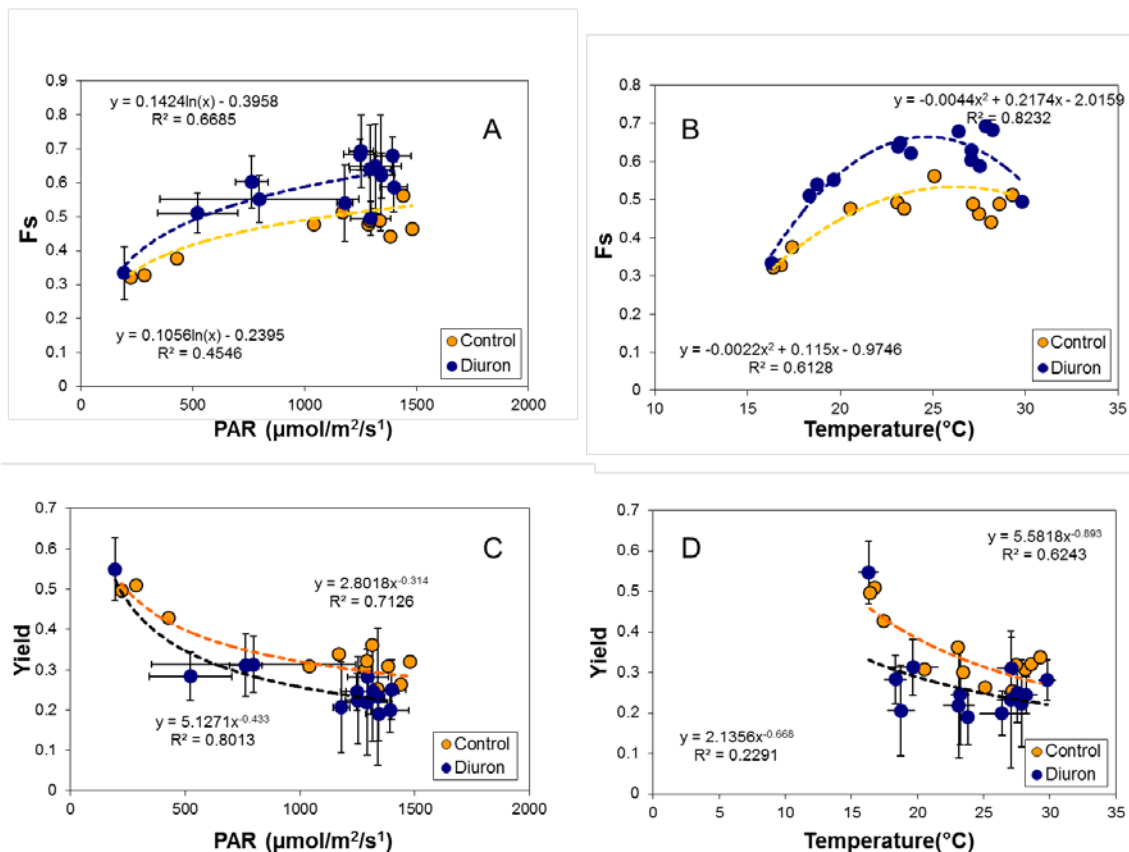


Figure 109: Scatterplot of (A) steady state and PAR, (B) steady state fluorescence and leaf temperature, (C) fluorescence yield and PAR and (D) fluorescence Yield and leaf temperature.

Leaf level measurements such as the Imaging Pam data show a clear difference between the control leaves and the DCMU treatment (Figure 109). Leaf steady state fluorescence emissions (F_s) increased (Figure 109, A and B), while photosynthetic efficiency of the treated plants decreased (Figure 109, C and D).

Further details about the leaf level measurements can be made available by Frantisek Zemek upon request.

5.5.2 Diurnal courses of reflectance values, vegetation indices, and sun-induced fluorescence

The following figures report the time courses of the normalised difference vegetation index (NDVI), the photochemical reflectance index (PRI), the sun-induced fluorescence at 760 nm (F_{760}), and the apparent fluorescence yield (Fy_{760} , ratio between estimated fluorescence and the radiation incident in a nearby restricted spectral range not including the oxygen absorption band, i.e., in the continuum).

Figure 110 shows the time course of the NDVI related to the canopy green biomass. The NDVI course is quite stable during the day, and we can observe only a slight increase of NDVI value between 5 and 9 September. NDVI values are slightly higher in the control grassland on both the days of sampling.

Figure 111 shows the time course of PRI. PRI has been proposed by Gamon et al. (1992) to track changes in the de-epoxidation state of the xanthophyll cycle pigments, related to heat dissipation. Recent experimental works support the hypothesis that zeaxanthin formation, via the xanthophyll cycle pigments, is responsible for the majority of dissipation of the excess excitation energy as heat, a process also known as non-photochemical quenching (NPQ). Under excess light, violaxanthin is converted rapidly via the intermediate antheraxanthin to zeaxanthin (i.e., de-epoxidation), and this reaction is reversed under low light levels (i.e., epoxidation). PRI is expected to decrease with increasing levels of heat dissipation (with increasing NPQ). PRI showed similar values in the two carpets during the first day of measurement, while in the second day (9 September) PRI showed higher values in the treated grassland compared to the control.

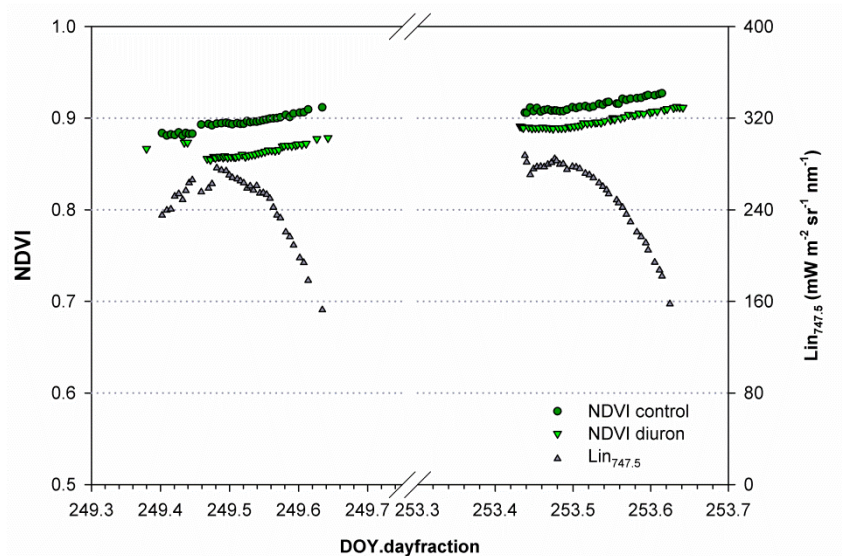


Figure 110: Time courses of the normalised difference vegetation index (NDVI) measured over the control (green circle) and the DCMU treated (green triangle) grassland carpets during 5 September (DOY 249) and 9 September (DOY 253). $Lin_{747.5}$ is the incident radiance ($mW m^{-2} sr^{-1} nm^{-1}$) at 747.5 nm.

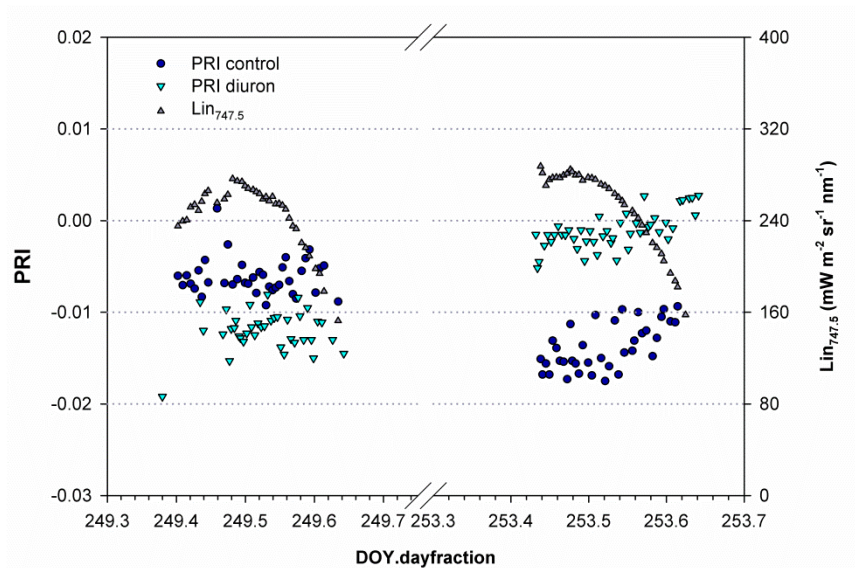


Figure 111: Time courses of the photochemical reflectance index (PRI, computed as $(R_{531} - R_{570}) / (R_{531} + R_{570})$) measured over the control (blue circle) and the DCMU treated (cyan triangle) grassland carpets during 5 September (DOY 249) and 9 September (DOY 253). Lin_{747.5} is the incident radiance (mW m⁻² sr⁻¹ nm⁻¹) at 747.5 nm.

The time courses of F_{760} are reported in Figure 112. As expected, during the day the intensity of F_{760} is generally proportional to the incident radiance, being at maximum at solar noon. On the contrary, the apparent fluorescence yield (Fy_{760} , ratio between estimated fluorescence and the radiation incident in a nearby restricted spectral range not including the oxygen absorption band, i.e., in the continuum) shows a more stable daily course (Figure 113). However a trend opposite to the one of Lin can be observed in early morning and late afternoon. This behaviour is more evident on the control carpet. This may indicate that the control sample is capable of regulating the efficiencies of the dissipation pathways (i.e., photochemistry and heat dissipation) in response to a decrease in incident radiation, better than the sample treated with DCMU which cannot drive the absorbed energy into the light reactions of photosynthesis.

The application of DCMU caused an increase of F_{760} up to 5 mW m⁻² sr⁻¹ nm⁻¹ on 9 September. This value is more than the double of the values measured on both treated and control carpets on 5 September and more than the double of the value measured on the same day in the control grassland. Fy_{760} is also increasing due to the DCMU application.

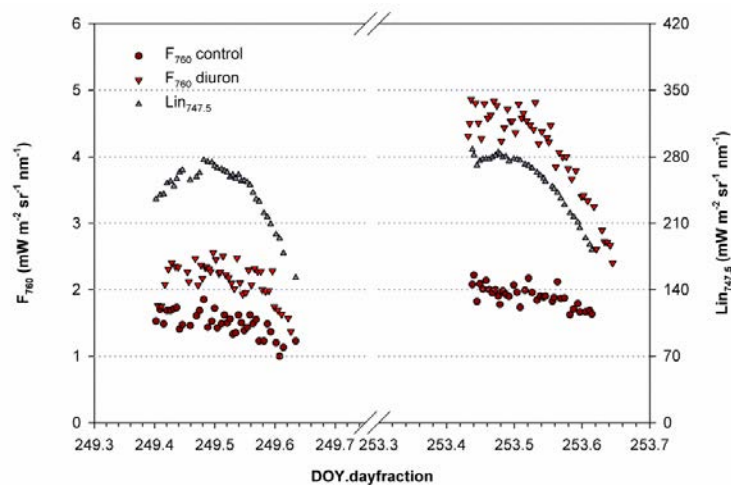


Figure 112: Time courses of sun-induced fluorescence at 760 nm (F_{760}) measured over the control (red circle) and the DCMU treated (red triangle) grassland carpets during 5 September (DOY 249) and 9 September (DOY 253). $\text{Lin}_{747.5}$ is the incident radiance ($\text{mW m}^{-2} \text{sr}^{-1} \text{nm}^{-1}$) at 747.5 nm.

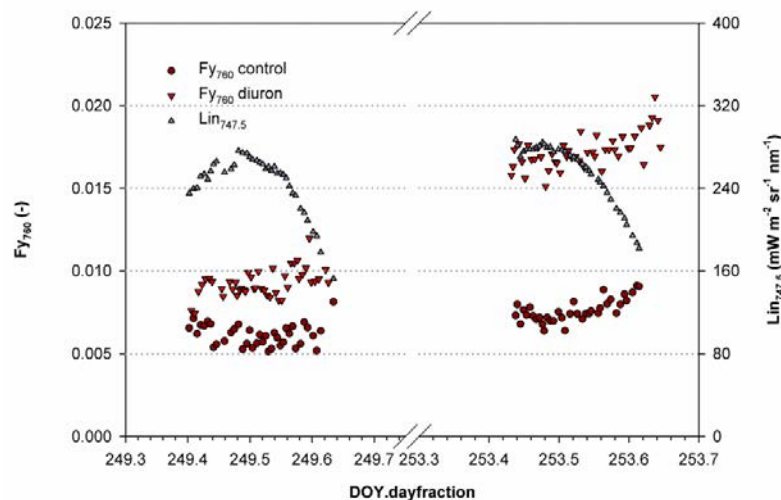


Figure 113: Time courses of the apparent fluorescence yield at 760 nm (F_{y760}) measured over the control (red circle) and the DCMU treated (red triangle) grassland carpets during 5 September (DOY 249) and 9 September (DOY 253). $\text{Lin}_{747.5}$ is the incident radiance ($\text{mW m}^{-2} \text{sr}^{-1} \text{nm}^{-1}$) at 747.5 nm.

5.5.3 Airborne measurements

5.5.3.1 Retrieval using spectral fitting method 1 (SFM-1)

Results in Figure 114 show that the DCMU treatment had no effects on leaf pigments or canopy structure as no difference of NDVI values (Figure 114, *left*) between treatments can be detected. The physiological change of treatments can be detected with changes in fluorescence in the $\text{O}_2\text{-A}$ (Figure 114, *middle*). However, absolute values of fluorescence are two times higher than ground reference measurements and non-fluorescence pixel show fluorescence values up to 4–5 $\text{mW/m}^2/\text{nm}/\text{sr}$. The fluorescence derived from $\text{O}_2\text{-B}$ (Figure 114, *right*) is dominated by noise and no clear outcome can be extracted.

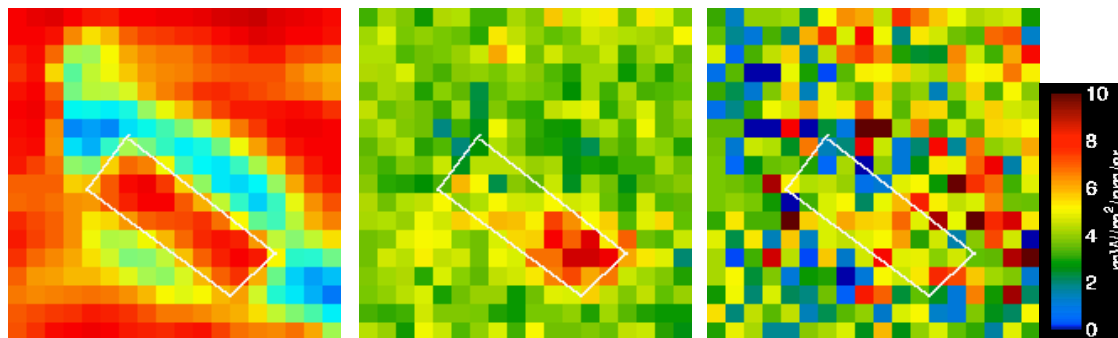


Figure 114: Estimated fluorescence at the Duron experiment using the apparent reflectance SFM-1 on a per-pixel-DEM-corrected high-altitude image. NDVI (*left*) showing vegetation in red and soils in blue, experiment area delimited by a white rectangle. O₂-A fluorescence (*middle*) and O₂-B fluorescence (*right*).

5.5.3.2 Fluorescence retrieval using singular vector decomposition

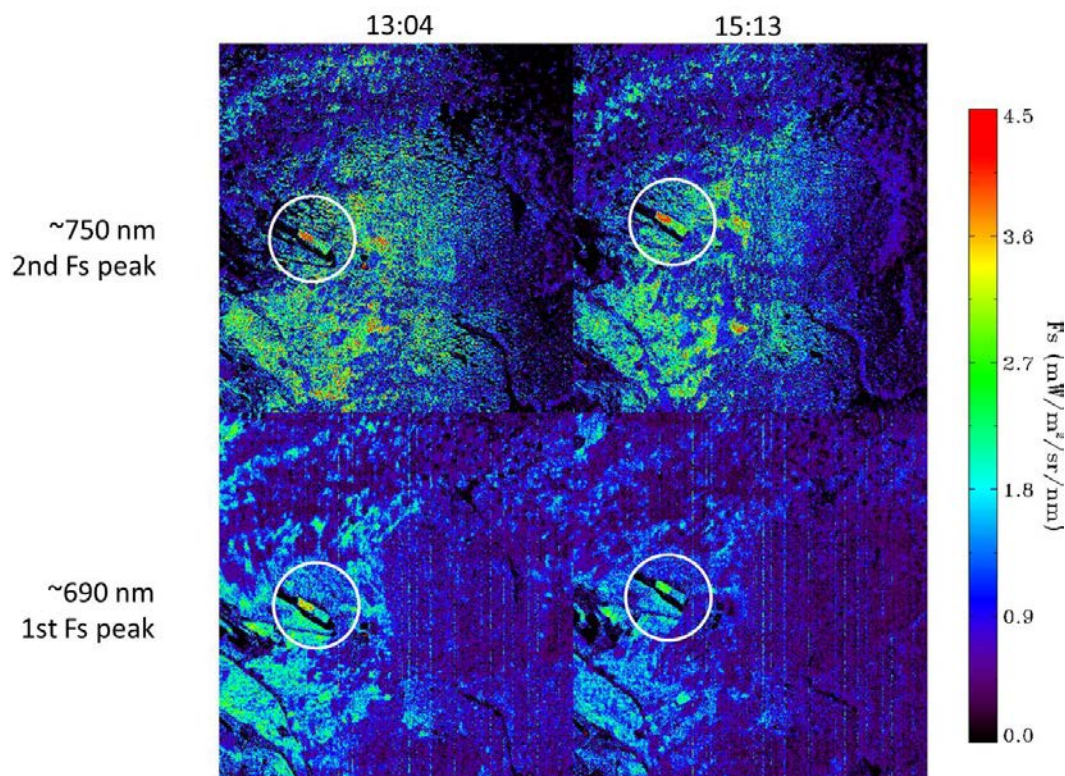


Figure 115: Fluorescence maps of the DCMU experiment derived using singular vector decomposition on 9 September.

DCMU treatment caused significant increase of fluorescence (within hours) (Figure 115) that is solely due to the physiological limitation of photosynthesis. The DCMU treatment had no effects on leaf pigments or canopy structure (Figure 116). The increased fluorescence signal is detected on the level of leaves (active measurement with PAM), a small canopy patch (active measurement with Maxi-PAM), top-of-canopy measurements (for passive measurement of sun-induced fluorescence, see chapter 5.5.2), and also from the aircraft at both bands using singular vector decomposition. The magnitude of changes is consistent across all spatial levels; thus,

this case study is the first very convincing proof that sun-induced fluorescence tracks changes in the physiological state of photosynthesis. These physiological changes can be monitored from an airborne platform.

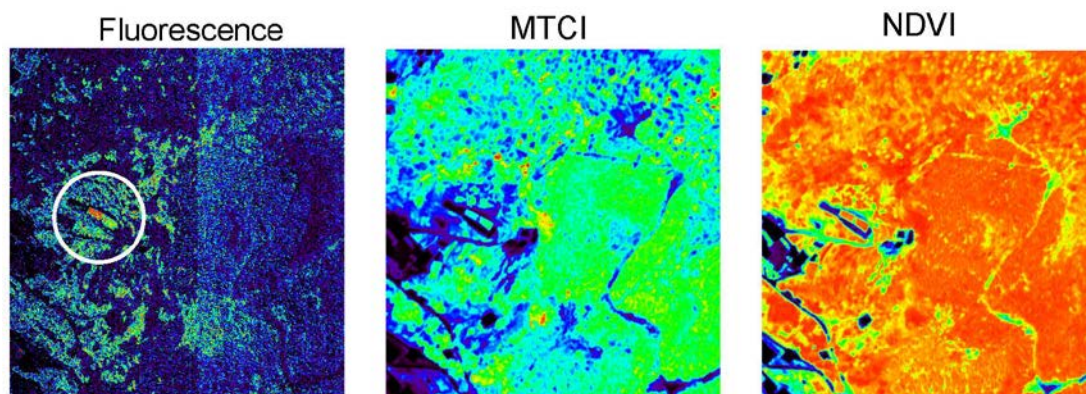


Figure 116: Fluorescence derived using singular vector decomposition, and MTCI and NDVI vegetation indices calculated from flight line on 9 September around midday (13:04).

References

- Alonso L, Gomez-Chova L, Vila-Frances J, Amoros-Lopez J, Guanter L, Calpe J, Moreno J. 2008. Improved Fraunhofer line discrimination method for vegetation fluorescence quantification. *Ieee Geoscience and Remote Sensing Letters* 5: 620–624.
- Amiridis V, Giannakaki E, Balis DS, Gerasopoulos E, Pytharoulis I, Zanis P, Kazadzis S, Melas D, Zerefos C. 2010. Smoke injection heights from agricultural burning in Eastern Europe as seen by CALIPSO. *Atmos. Chem. Phys.* 10: 11567–11576.
- Berk A, et al. 2004. MODTRAN5: A reformulated atmospheric band model with auxiliary species and practical multiple scattering options. Pages 341–347.
- Carter GA, Theisen AF, Mitchell RJ. 1990. Chlorophyll fluorescence measured using the Fraunhofer line-depth principle and relationship to photosynthetic rate in the field. *Plant Cell and Environment* 13: 79–83.
- Corp LA, Middleton EM, McMurtrey JE, Campbell PKE, Butcher LM. 2006. Fluorescence sensing techniques for vegetation assessment. *Applied Optics* 45: 1023–1033.
- Damm A, Erler A, Hillen W, Meroni M, Schaepman ME, Verhoef W, Rascher U. 2011. Modeling the impact of spectral sensor configurations on the FLD retrieval accuracy of sun-induced chlorophyll fluorescence. *Remote Sensing of Environment* 115: 1882–1892.
- Damm A, et al. 2010. Remote sensing of sun induced fluorescence yield to improve modelling of diurnal courses of Gross Primary Production (GPP). *Global Change Biology* 16: 171–186.
- Daumard F, Champagne S, Fournier A, Goulas Y, Ounis A, Hanocq J. 2010. A field platform for continuous measurement of canopy fluorescence. *IEEE transactions on geoscience and remote sensing* 48: 3358–3368.
- Gamon JA, Peñuelas J, Field CB. 1992. A narrow-waveband spectral index that tracks diurnal changes in photosynthetic efficiency. *Remote Sensing of Environment* 41: 35–44.
- Guanter L. 2007. New algorithms for atmospheric correction and retrieval of biophysical parameters in Earth observation. Application to ENVISAT/MERIS data. PhD thesis. Universitat de Valencia, Valencia.
- Guanter L, Alonso L, Gomez-Chova L, Meroni M, Preusker R, Fischer J, Moreno J. 2010. Developments for vegetation fluorescence retrieval from spaceborne high-resolution spectrometry in the O2-A and O2-B absorption bands. *Journal of Geophysical Research-Atmospheres* 115.
- Guanter L, Rossini M, Colombo R, Meroni M, Frankenberg C, Lee JE, Joiner J. 2013. Using field spectroscopy to assess the potential of statistical approaches for the retrieval of sun-induced chlorophyll fluorescence from ground and space. *Remote Sensing of Environment* 133: 52–61.
- Joiner J, Guanter L, Lindstrot R, Voigt M, Vasilkov AP, Middleton EM, Huemmrich KF, Yoshida Y, Frankenberg C. 2013. Global monitoring of terrestrial chlorophyll fluorescence from moderate spectral resolution near-infrared satellite measurements: methodology, simulations, and application to GOME-2. *Atmos. Meas. Tech. Discuss.* 6: 3883–3930.
- Kokkalis P, Papayannis A, Amiridis V, Mamouri RE, Veselovskii I, Kolgotin A, Tsaknakis G, Kristiansen NI, Stohl A, Mona L. 2013. Optical, microphysical, mass and geometrical properties of aged volcanic particles observed over Athens, Greece, during the Eyjafjallajökull eruption in April 2010 through synergy of Raman lidar and sunphotometer measurements. *Atmos. Chem. Phys.* 13: 9303–9320.
- Liu LY, Zhang YJ, Wang JH, Zhao CJ. 2005. Detecting solar-induced chlorophyll fluorescence from field radiance spectra based on the Fraunhofer line principle. *Ieee Transactions on Geoscience and Remote Sensing* 43: 827–832.

- Louis J, et al. 2005. Remote sensing of sunlight-induced chlorophyll fluorescence and reflectance of Scots pine in the boreal forest during spring recovery. *Remote Sensing of Environment* 96: 37–48.
- Maier SW, Günther KP, Stellmes M. 2003. Sun-induced fluorescence: A new tool for precision farming. Pages 209–222 in McDonald M, Schepers J, Tarty L, van Toai T, Major D, eds. *Digital Imaging and Spectral Techniques: Applications to Precision Agriculture and Crop Physiology*, vol. 66 ASA Special Publication.
- Malenovský Z, Homolová L, Zurita-Milla R, Lukeš P, Kaplan V, Hanuš J, Gastellu-Etchegorry J-P, Schaepman ME. 2013. Retrieval of spruce leaf chlorophyll content from airborne image data using continuum removal and radiative transfer. *Remote Sensing of Environment* 131: 85–102.
- Mazzoni M, Meroni M, Fortunato C, Colombo R, Verhoef W. 2012. Retrieval of maize canopy fluorescence and reflectance by spectral fitting in the O-2-A absorption band. *Remote Sensing of Environment* 124: 72–82.
- Meroni M, Busetto L, Colombo R, Guanter L, Moreno J, Verhoef W. 2010. Performance of spectral fitting methods for vegetation fluorescence quantification. *Remote Sensing of Environment* 114: 363–374.
- Meroni M, Rossini M, Guanter L, Alonso L, Rascher U, Colombo R, Moreno J. 2009. Remote sensing of solar induced chlorophyll fluorescence: Review of methods and applications. *Remote Sensing of Environment* doi:10.1016/j.rse.2009.05.003.
- Moya I, Camenen L, Evain S, Goulas Y, Cerovic ZG, Latouche G, Flexas J, Ounis A. 2004. A new instrument for passive remote sensing 1. Measurements of sunlight-induced chlorophyll fluorescence. *Remote Sensing of Environment* 91: 186–197.
- Papayannis A, Mamouri RE, Amiridis V, Kazadzis S, Pérez C, Tsaknakis G, Kokkalis P, Baldasano JM. 2009. Systematic lidar observations of Saharan dust layers over Athens, Greece in the frame of EARLINET project (2004–2006). *Ann. Geophys.* 27: 3611–3620.
- Plascyk JA. 1975. MK II Fraunhofer Line Discriminator (FLD-II) for airborne and orbital remote-sensing of solar-stimulated luminescence. *Optical Engineering* 14: 339–346.
- Reichstein M, et al. 2005. On the separation of net ecosystem exchange into assimilation and ecosystem respiration: review and improved algorithm. *Global Change Biology* 11: 1424–1439.
- Zong Y, Brown SW, Johnson BC, Lykke KR, Ohno Y. 2006. Simple spectral stray light correction method for array spectroradiometers. *Applied Optics* 45: 1111–1119.